HYDRODYNAMICS OF POLYMERS IN SOLUTION

FINAL REPORT

CONTRACT REPORT NO. OSQ83-00157

PART I: LOW REYNOLDS NUMBER FLOW THROUGH FIBROUS POROUS MEDIA

PART II: PERMEABILITY MEASUREMENT OF POLYMER CHAINS IN SOLUTION

by

D. F. James, Ph.D., P.Eng.
C. P. Chesneau, M.A.Sc.
D. G. Kimbell, B.A.Sc.
C. R. Fraser, B.A.Sc.

Work Conducted for the Department of Energy, Mines and Resources

DSS File No. 03SQ.23440-3-9088

CANMET Scientific Authority: Dr. W. Friesen

March, 1985

168 pp

S & J Engineering Inc.
403 Wellesley St. E.
Toronto, Ontario M4X 1H5

MICROMEDIA
OCT 11 1985

Organization of Final Report

This final report really consists of two separate reports. The first, Part I, deals with theoretical work to predict the permeability of fibrous porous media, and the second, Part II, describes experiments to measure the permeability of entangled polymer chains in solution. Since each Part is self-contained, it appears with its own title page, table of contents, page numbers, and bibliography; each can be read on its own.

Hydrodynamics of Polymers in Solution

PART I: LOW REYNOLDS NUMBER FLOW THROUGH FIBROUS POROUS MEDIA

by

D. F. James, Ph.D., P.Eng.
C. P. Chesneau, M.A.Sc.

Work Conducted for the Department of Energy, Mines and Resources

DSS File No. 03SQ.23440-3-9088

CANMET Scientific Authority: Dr. W. Friesen

March, 1985

S & J Engineering Inc.
403 Wellesley St. E.
Toronto, Ontario M4X 1H5

ABSTRACT

The relationship between pressure drop over some length and discharge velocity through fibrous porous media, or permeability, is theoretically investigated. A mathematical model is proposed to represent low inertia flow past the fibers of these media. The entangled fibers are modelled by randomly oriented rings whose centers lie in a cubical lattice. All rings have the same radius of curvature and body radius. The rings are very thin so that slender body theory can be used to obtain the drag on a single ring at all orientations. The linearity of governing equations is then used to obtain the hydrodynamic interaction effects in the total matrix by studying the drag on two rings. The resulting permeability is a function of curvature as well as solid volume fraction of fibers; however, the dependence on curvature is so small that a single value is chosen to represent most randomly-coiled porous media.

TABLE OF CONTENTS

Page

Acknowledgement i

Abstract ii

List of Common Symbols iv

List of Figures vii

Chapter I: Introduction . . . . I- 1
  i) Porous Media . . . . I- 1
  ii) Experimental Investigations . . . . I- 3
  iii) Theoretical Investigations . . . . I- 6

Chapter II: The Conception of a Model with Curvature II-1

Chapter III: Mathematical Treatment of the Model III-1
  Section A: Slender Body Theory III-1
  Section B: Forces on a Ring in a Uniform Flow III-10
    i) Flow Normal to a Ring III-10
    ii) Flow Aligned with a Ring III-15
    iii) Flow at Any Angle to a Ring III-23
    iv) The Average Drag on a Ring III-25
  Section C: Interaction Among Rings III-28
    i) Two Coaxial Rings Normal to the Flow III-29
    ii) The Average Interaction Between 2 Rings III-35
    iii) Cubical Array of Randomly Oriented Rings III-37

Chapter IV: Presentation of Results and Conclusions IV-1
  i) Presentation of Results IV-1
  ii) Conclusions IV-5

References . . . . R- 1

Figures 1 to 17 . . . . Fig. 1

Appendix A: Drag on a Cylindrical Rod in Uniform Flow . . . . A- 1

Appendix B: The Integration of I_d and I_e . . . . B- 1

Figure A1 . . . . Fig.A1

LIST OF COMMON SYMBOLS

a	Fiber radius.
A	Equivalent sphere radius.
D	Center to center distance between rings.
E(m)	Complete elliptic integral of the 2nd kind.
$\bar{f}$	Stokeslet strength vector.
$\bar{F}$	Force on a body (Section A). Drag on a single ring at any orientation (Section B). Average force per ring in a matrix (Section C).
$\bar{F}$	Average drag on a single ring.
$\bar{F}'$	Force on a ring at any orientation.
$\bar{F}_1$	Force on a ring normal to the flow.
$\bar{F}_2$	Force on a ring aligned with the flow.
$\bar{F}_3$	Force per ring, two coaxial rings normal to the flow.
G	Value equal to the $\ln(8R/a) + 2/5$.
G_1	Value equal to the $\ln(8R/a) + 1/2$.
$\bar{H}$	Vector integral of the interaction term.
I	with various subscripts: integrals appearing in calculations.
J_1	Two body interaction term.
J	General interaction term.
k	Intrinsic permeability.
K(m)	Complete elliptic integral of the 1st kind.
L	Length of straight rod (Appendix A). Length of a slender body (Section A).
m	Argument of elliptic integrals

n	as a subscript: Denotes the component normal to the centerline. Constant.
$\frac{\Delta P}{\Delta x}$	Pressure drop (or piezometric head) per unit length.
$\bar{r}$	Distance vector from s to s_0 (see Figure 7).
r_0	Short distance around s_0 equal to a $\sqrt{e}/2$
$\bar{r}_2$	Distance vector from s_2 to s_0 (see Figure 9).
R	Ring radius.
s	General point on the centerline of: slender body (Section A). ring (Sections B & C). rod (Appendix A).
s_0	Specific point where boundary conditions are matched.
t	as a subscript: Denotes the component tangents to the centerline.
T	Tangential force to velocity proportionality constant.
$\bar{U}$	Far field velocity.
$\bar{U}_D$	Velocity field associated with a doublet.
$\bar{U}_s$	Velocity field associated with a Stokeslet.
$\bar{x}$	Position vector.
α	Angle equal to $\theta-\theta_0$.
α_0	Small angle around θ_0 (equal to $a\sqrt{e}/2R$).
γ	Normal to tangential drag ratio.
$\bar{\delta}$	Doublet strength vector.
Δ	Constant.
η	Constant.
θ	Angular position on a ring (see Figure 7).
θ_0	Specific angle where boundary conditions are matched.
θ_2	Angular position on a second ring (see Figure 9).

μ	Fluid dynamic viscosity.
ξ	Angle equal to $\theta_2-\theta_0$.
ϕ	Solid volume fraction or fibre volume concentration.
Ω	Second term of permeability equations.

LIST OF FIGURES

1. Non-Dimensional Permeability as a Function of Solidity, for Various Porous Media.
2. Parallel Rod Model for Porous Media.
3. Non-Dimensional Permeability versus Solid Volume Fraction (Three-Dimensional Fiber Networks).
4. Schematic Representation of a Portion of a Polymer Skein in an Aqueous Solution.
5. Conceptual Diagram for Rings in a Cubical Array.
6. Definition Diagram for Lighthill's Theorem.
7. Definition Diagram for an Isolated Ring in a Uniform Flow.
8. Definition Diagram of Flow-Related Parameters.
9. Definition Diagram for Two Coaxial Rings in a Uniform Flow.
10. Table of Values for Ω as the Ratio R/D Varies.
11. Non-Dimensional Permeability versus Radius of Curvature for a Solid Volume Fraction of $\phi = .01$.
12. Non-Dimensional Permeability versus Radius of Curvature for a Solid Volume Fraction of $\phi = .001$.
13. Non-Dimensional Permeability versus Radius of Curvature for a Solid Volume Fraction of $\phi = .0001$.
14. Table of Values of the Non-Dimensional Permeability versus the Solid Volume Fraction for Different Theories.
15. Non-Dimensional Permeability versus Solid Volume Fraction for Several Theories.
16. Table of Values of the Non-Dimensional Permeability versus the Ratio R/D and the Solid Volume Fraction.
17. Non-Dimensional Permeability versus Solid Volume Fraction for Two Values of the Radius of Curvature.

A1. Definition Diagram for a Rod in a Uniform Flow.

CHAPTER I

INTRODUCTION

i) POROUS MEDIA

The study of flow through porous media is basic to many scientific and engineering fields. Such diverse areas as soil mechanics, petroleum engineering and filtration all rely on understanding porous media flow to solve problems. Porous media can be naturally classified into a number of basic categories. While most media are highly compact, granular in nature, there is a class of media comprised of very long, thin, loosely packed particles which can be described as fibrous. Fibrous porous media include paper filters, steel wool and even banks of heat exchanger tubes. Another example comes from the microscopic structure of a concentrated polymer solution. Entangled polymer molecules in solution form a skein through which the solvent flows. Fibrous porous media can therefore be thought of as a continuous network of randomly coiled filaments, or as very long thin fibers, whose length to diameter ratio is so large that length ceases to be a parameter.

The density of a fibrous porous medium can be expected to be much lower than that of a granular structure. The compaction of grains permits the solid part of the latter medium to occupy most of the total volume, while the solid portion of a fibrous medium occupies only a small fraction of the total volume. Since the solid volume fraction in fibrous media varies over several orders of magnitude, it is chosen to characterize media density, as opposed to void fraction, or porosity, which is commonly used for soils and other granular-type porous media. Some porous media, such as paper filters, can have solid volume fractions as high as 10%, though most have much lower solid fractions. At the other end of the scale, polymer solutions often have effective solid fractions well below 0.1%. At these solid fractions, fibers are separated by many particle diameters and the fibrous characteristics of the media are most important in these regimes. While solid fraction is an important physical property of porous media, another parameter is needed to characterize its hydrodynamic properties.

The needed parameter is permeability, which is a measure of a fluid's ability to seep through voids of a medium. The permeability of a medium is directly related to the resistance it offers to the flow. Media which offer a high resistance to flow, for example, are said to have low permeabilities, while high permeabilities mean low resistance. The resistance to flow is measured by the drop in pressure over some flow length. Intrinsic permeability, denoted by the symbol k, is the relationship between pressure drop and flow rate as defined by the following hydrodynamic law:

$$k\frac{\Delta P}{\Delta x} = \mu\frac{Q}{S} \qquad (1)$$

where Q is the volumetric flow rate through a cross-sectional area S, μ is the fluid's dynamic viscosity and $\frac{\Delta P}{\Delta x}$ is the pressure drop per unit length in the streamwise direction. The present work is aimed at the determination of the permeability of fibrous porous media.

The fibers in a typical porous medium generally have circular cross-sections of constant radius. Because k has units of $[L^2]$, fiber radius is naturally used to express the permeability in dimensionless form.

Dimensionless permeability varies from medium to medium. Solid fraction clearly affects it since loosely packed media tend to have high permeabilities while compact media are much less permeable. However, permeability is also a function of fiber arrangement. Fiber orientation and curvature, as well as inhomogeneous fiber distribution, all contribute to permeability. Therefore, in theoretical studies at least, a specific fiber geometry is often chosen to express the permeability as a function of solid fraction only. In general, a relationship of the type

$$\frac{k}{a^2} = f(\emptyset) \qquad (2)$$

is sought, where a is the fiber radius and $\emptyset$ the solid fraction.

Equation 1, which states the relationship between pressure and flow rate, is given the name of Darcy's Law after the French engineer Henry Darcy who proposed this law (1) in 1856. Darcy based his conclusions on experimental work done using homogeneous porous media of the granular variety. This relationship has since been verified for a wide variety of porous media, some of which were fibrous. Since fibrous media are of interest here, the portion of work done on these media is now reviewed.

ii) EXPERIMENTAL INVESTIGATIONS

The earliest experiments dealing with these fibrous media were carried out in the late thirties and early forties. Carman (2), Wiggins et al. (3) and Sullivan (4) performed numerous experiments involving such materials as steel and copper wire, glass rods, glass wool, fiberglass and various wools. In the fifties, Bergelin et al. (5) conducted experiments with flow perpendicular to heat exchanger tubes. Chen (6) and later Wheat (7) gathered data from various filter mats.

It was not until the 1960s that the permeability of polymer gels was investigated when White (8) found the pressure drop of distilled water across various concentrations of acrylamide polymer. The permeability of hyaluronic acid, a biological polymer, was the object of experiments by Jackson and James (9). Another biological medium was the subject of investigations by Stenzel et al. (10) who provided data on the permeability of collagen, a fibrous material found throughout the human body.

Most of these data were obtained for very loose media. Solid fractions ranged from 3×10^{-4} for the lowest concentrations of hyaluronic acid to 0.5 for the most dense arrangement of heat exchanger tubes. Some very high solidities were also investigated, however. Kostornov and Shevchuk (11) worked with discs of compressed 20% Cr-80% Ni alloy fibers with solidities ranging from 0.31 to 0.71.

Because these various experimental results were presented in different ways by various authors, it has been difficult to make direct comparisons from medium to medium. However, in a review paper, Jackson and James (12) collected the data for all experiments reviewed here and plotted the results on the master graph shown in Figure 1. It is clear that these data do not result in a unique determination of the permeability; that is, the function of $f(\phi)$ of equation 2 is not uniquely determined. This is due to the many configurations taken by the fibers of these media. Some are comprised of parallel rods, such as heat exchanger tubes, while others have fibers arranged in bundles of varying densities. Furthermore, if the fibers are not evenly distributed throughout the medium, the fluid tends to rush through the empty "spaces" between fiber bundles, thereby raising the effective permeability. Because of such problems, a unique value for $f(\phi)$ cannot be determined; however, Davies (13) proposed a correlation based on permeability data for media ranging from glass wool and copper wire to camel hair and down. He proposed the relation:

$$\frac{k}{a^2} = \frac{1}{16\phi^{1.5}(1+56\phi^3)} \qquad (3)$$

which is the equation of a "best-fit" curve passing through his data points. The author states that his correlation is valid for the solid fractions between .006 and .3 and for Reynolds numbers less than unity. The last restriction is generally valid for all porous media since Darcy's Law is a linear equation, i.e., inertial effects are negligible. The media described by Davies' equation have randomly oriented fibers. This correlation is not expected to be valid for media whose fibers are parallel, such as the tubes of a heat exchanger, because the permeability of a homogeneous fibrous medium is affected by fiber orientation. Media comprised of fibers oriented normal to the flow have lower permeabilities than those whose fibers are aligned with it, and theoretical models have shown this permeability ratio to be 1 to 2 (14, 15).

iii) THEORETICAL INVESTIGATIONS

Most theoretical models of fibrous porous media idealize the medium as a matrix of straight rods. Parallel rods of infinite length are placed in a periodic manner, usually in a square array as shown in Figure 2, and the flow is aligned with the rods or normal to them. The permeability is found by solving the equations of Stokes and continuity.

The Stokes equation expresses the conservation of fluid momentum at very low Reynolds numbers. Since the Reynolds number is considered as the ratio of the inertia forces to viscous forces, the condition of very low Reynolds numbers amounts to very small inertia. The Stokes approximation, then, neglects all inertia terms which appear in the general Navier-Stokes equation. The Stokes equation is written

$$0 = -\nabla p(\bar{x}) + \mu \nabla^2 \bar{u}(\bar{x})$$

where $\bar{u}(\bar{x})$ is the velocity vector, $\bar{x}$ is the position vector, $p(\bar{x})$ is the pressure and μ is the fluid's dynamic viscosity.

The continuity equation expresses the conservation of mass. Since the fluids of interest in the present case are incompressible, the continuity equation is written as

$$\nabla \cdot \bar{u}(\bar{x}) = 0$$

These two equations, coupled with appropriate boundary conditions, must be satisfied in a low Reynolds number flow problem. In the case of these parallel rod models, the approach is generally to solve the problem for a single period of the periodic arrangement, effectively dividing the medium in constituent cells.

Solving for the flow aligned with the rods is simpler than solving for flow across the array because the velocity vector has only a single component parallel to the array. Happel (14), Sparrow and Loeffler (16) and Drummond and Tahir (15) all presented different methods to solve for the flow parallel to arrays of rods.

Happel (14) found an approximation to the problem of square array using a shear-free surface cell model. In this approximation all the fluid around each rod is channelled into a concentric cylindrical cell with zero shear at the surface. These cells have circular cross-sections as opposed to the actual square cross-section. This is a model based on the assumption that the flow is not significantly affected by the exact shape of the outside boundary provided that the appropriate no-slip boundary condition at the wall of the rod is maintained. The pressure drop was calculated from the drag on a rod and the following permeability was obtained:

$$\frac{k}{a^2} = \frac{1}{4\phi} \left(\ln \frac{1}{\phi} - 1.5 + 2\phi - 0.5\phi^2 \right)$$

Sparrow and Loeffler (16) solved this problem numerically. They considered both square and equilateral triangular arrays and solved the Stokes equations numerically for the proper boundary conditions at the edge of the cell. They used a Laurent series solution which was matched analytically to all but one boundary condition, then the shear was required to vanish at discrete points on the boundary. They presented results in tabular and graphical form which agree with those predicted using Happel's equation.

A different technique was used by Drummond and Tahir (15) to match the final boundary condition of Sparrow and Loeffler's Laurent series solution. They placed two-dimensional singularities at the center of each rod to obtain a second solution to the Stokes equation to within an undetermined constant. The two solutions were matched to obtain the final constant. Permeabilities were obtained to order ϕ^2 or better for the case of square, equilateral triangular, hexagonal and rectangular arrays. The results were generalized to yield

$$\frac{k}{a^2} = \frac{1}{4\phi}(\ln\frac{1}{\phi} - \Omega + 2\phi - \frac{1}{2}\phi^2 + O(\phi^3))$$

where the constant Ω depends on array configuration. This constant for the square array is 1.476, which is similar to the less accurate results of Happel ($\Omega = 1.5$) and Sparrow and Loeffler, while the triangular, hexagonal and rectangular arrays have values of Ω of 1.498, 1.354 and 1.130 respectively.

Problems where the flow is normal to the array are more complex since the velocity vector has two components, both perpendicular to the rods. These problems can, however, be solved by similar techniques. In fact, Happel (14) used his shear-free surface cell model to calculate the permeability across a square array. He obtained

$$\frac{k}{a^2} = \frac{1}{8\phi}\left(\ln\frac{1}{\phi} - 1 + O(\phi^2)\right).$$

This model was also used by Kuwabara (17) with a zero vorticity condition of the cell surface to obtain

$$\frac{k}{a^2} = \frac{1}{8\phi}\left(\ln\frac{1}{\phi} - 1.5 + 2\Phi\right).$$

Hasimoto (18) used a Fourier series technique to solve for permeability across the same array and found

$$\frac{k}{a^2} = \frac{1}{8\phi}\left(\ln\frac{1}{\phi} - 1.476 + O(\phi)\right),$$

while Sangani and Acrivos (19) used a similar series technique and numerically solved for both square and hexagonal arrays. Their results were graphed and tabulated and, in the case of the square array, were found to agree with Hasimoto's equation.

A basic pattern is observed. The ratio of permeabilities for the two flow directions is approximately 2:1 with the flow normal to the array having the lower permeability. This is also found to be the ratio of drags on an isolated rod of finite length when it is placed parallel and normal to a uniform flow (20, 21). This ratio, however, was found to be exactly 2:1 to order ϕ by Drummond and Tahir (15). They used their method to solve for the permeability of square and triangular arrays and found it to be precisely half that obtained for flow parallel to these respective arrays.

Theoretical work on two dimensional arrays is not sufficient to accurately describe a three dimensional fibrous porous medium. Only two models for three-dimensional fibrous media are found in the literature. These are presented by Spielman and Goren (22) and Jackson and James (9).

The essence of Spielman and Goren's (22) model is that, on average, the fluid in the proximity to a rod experiences a viscous drag while Darcy's law governs the far field flow to account for the influence of neighbouring rods. The drag on a rod oblique to the flow, which is considered immersed in a porous medium, is calculated. The porous medium's permeability is eventually determined from the calculated drag averaged over flow direction. The permeability is implicitly given by

$$\frac{1}{3} + \frac{5}{6}\frac{\sqrt{k}}{a}\frac{K_1(\frac{a}{\sqrt{k}})}{K_0(\frac{a}{\sqrt{k}})} = \frac{1}{40} \qquad (4)$$

where K_0 and K_1 are modified Bessel functions of the second kind. In this approximation, the medium is not well defined since the influence of neighbouring rods are taken into account only by a model of the far field condition. A more accurately defined system can be obtained by superimposing results obtained for the two orthogonal directions.

Jackson and James (9) proposed such a method. They argued that a random fibrous porous medium has the same permeability as a cubical lattice of rods having the same diameter and volume fraction. The pressure drop through the lattice was calculated by adding the pressure drops due to the parallel and normal rods. If $\frac{\Delta P_1}{\Delta x}$ is the pressure drop for flow parallel to a square array of rods and $\frac{\Delta P_2}{\Delta x}$ is the pressure drop for flow normal to such an array, since there are twice as many perpendicular rods as parallel ones, the total pressure drop is obtained by the addition:

$$\frac{\Delta P}{\Delta x}(\phi) = \frac{\Delta P_1}{\Delta x}\left(\frac{\phi}{3}\right) + \frac{\Delta P_2}{\Delta x}\left(\frac{2\phi}{3}\right)$$

The permeability is then found using Darcy's Law. Jackson and James used the parallel and perpendicular flow permeabilities given by Happel; however, a revised result using the more accurate Drummond and Tahir equations was later obtained (12) which states:

$$\frac{k}{a^2} = \frac{3}{20}\frac{1}{\phi}\left(\ln\frac{1}{\phi} - .931 + O\left(\ln^{-1}\frac{1}{\phi}\right)\right) \qquad (5)$$

This calculation does not take into account the nature of the interactions between the parallel and perpendicular rods.

All the theories presented here were compared to each other and to experimental data in the review paper of Jackson and James (12). In particular, they compared equations 4 and 5 with experimental data on the graph shown in Figure 3. It is apparent that despite the different nature of equations 4 and 5, they both agree reasonably well with each other and with experimental data. The results obtained from Speilman and Goren's equation fall within 20% of Jackson and James'. The agreement cannot be expected to be any better considering the approximations made in each model. The interactions between parallel and perpendicular rods, neglected in Jackson and James' calculation, for example, can be shown to affect the second order term in the expression for k/a^2.

This influence can be illustrated using a different but equivalent superposition of the two flow directions. By noting that there are the same number of rods aligned with each of the three Cartesian coordinate axes in a cubical lattice, the total pressure drop can be written:

$$\frac{\Delta P}{\Delta x}(\phi) = \frac{\Delta P_1}{\Delta x}\left(\frac{\phi}{3}\right) + \frac{\Delta P_2}{\Delta x}\left(\frac{\phi}{3}\right) + \frac{\Delta P_2}{\Delta x}\left(\frac{\phi}{3}\right).$$

Since the pressure drop is not a linear function of ϕ, this equation yields a slightly different result. Again, making use of the equations of Drummond and Tahir, the permeability is calculated. The result is:

$$\frac{k}{a^2} = \frac{3}{20}\frac{1}{\phi}\left(\ln\frac{1}{\phi} - .378 + 0\left(\ln^{-1}\frac{1}{\phi}\right)\right).$$

Here, the values obtained for the permeability differ by about 15% from equation 5. The result of Jackson and James should therefore be regarded only as a rough approximation to a cubical lattice and not as an accurate solution.

Three-dimensional theories to date, then, do not seem to be entirely adequate since the results are approximate and since they apply to porous media comprised only of straight fibers. It is noted that neither of these theories takes any account of the curvature of fibers.

Some fibrous porous media, such as steel wool or entangled polymer molecules in solution, are comprised of flexible, randomly coiled filaments as illustrated in Figure 4. Since all random configurations are hydrodynamically equivalent, the curvature of fibers and the solid fraction are the only parameters which influence the permeability of a fibrous porous medium. In this thesis, a well defined model possessing curvature is proposed. This model is then used to predict the permeability of porous media. The result will be compared to other predictions, and to experimental data, found in the literature, for fibrous porous media.

CHAPTER II

THE CONCEPTION OF A MODEL WITH CURVATURE

The main problem here is to develop a model which is a realistic representation of a random fibrous structure, such as in Figure 4, but which retains sufficient simplicity for mathematical analysis. It is expected that some approximations must be made to accomplish this.

Some assumptions on the curvature of fibrous media can be made. As shown in Figure 4, the local radius of curvature of these structures is much larger than the body radius and varies only slightly from coil to coil. The average radius of curvature is then never significantly different from the local curvature at any given location. In order to obtain a first approximation to the influence of curvature, a model possessing a single radius of curvature is sufficient. Furthermore, the ratio of the body radius to the radius of curvature is small, so that expansions for small values of this ratio are possible.

The homogeneity of the medium must also be considered. Because it is difficult to treat a medium in which the solid fraction varies randomly throughout, only homogeneous structures will be dealt with here.

A simple model possessing all these characteristics can be obtained by a uniform distribution of thin rings. Homogeneity is obtained by letting the ring centers lie in a cubic arrangement while the randomness of the fibrous structure can be accounted for by letting each ring have a random orientation, as shown in Figure 5. It follows from the fixed radius of curvature assumption that all rings are of equal size. The thickness of the ring is taken to be the fiber radius a, while the ring radius, denoted by R, represents the average radius of curvature of the medium. The separation between ring centers is denoted by D as shown in

Figure 5. This is now a well defined medium, with the single random parameter being the orientation of each ring. What is meant by random orientation is that the probability that a ring be in a given orientation is the same as the probability that the ring be in any other orientation.

The problem is to find the permeability of the ring matrix, and the approach here is to first study the drag on an isolated ring in a uniform flow at any orientation. From this result, the drag is averaged over all possible flow directions to obtain the average drag per ring when the influence of nearby rings is neglected. The influence of interaction is then estimated by considering the drag on a ring when a second ring is nearby. This result is then generalized to a complete array but the solution leaves three undetermined constants. These constants are found by matching to limiting cases with exact solutions.

The drag on a single ring of various orientations to the flow will be obtained using low Reynolds number slender body theory. This theory, initiated by Burgers (23) and greatly improved by Cox (20), Tillett (21), Batchelor (24) and Lighthill (25), depends on approximations which are valid when bodies are very long and thin. Slender body theory is well suited to the calculation of the drag on a ring when it has a very small $\frac{a}{R}$ ratio. In this theory, a long slender solid is placed in a given undisturbed flow. Under conditions in which fluid inertia is negligible, the force per unit length on the body is obtained as an asymptotic expansion in terms of the ratio of the cross-sectional radius a to body length L. There are two basic approaches to solving these slender body problems at low Reynolds numbers.

The first is a method of inner and outer expansions which was formulated by Cox (20). Cox defines an outer expansion for small $\frac{a}{L}$, in which L is the characteristic dimension, and an inner expansion, also for small $\frac{a}{L}$, but for which the characteristic dimension is a. The inner expansion is then matched to the solution for the outer expansion. In his paper, Cox treated, among other examples, the case of a uniform flow past a ring in the plane of flow. He expressed his results as a two term expansion in powers of $\ln^{-1}(\frac{R}{a})$.

The alternate approach used by Tillett, Batchelor and Lighthill is the one used here. This method involves the distribution of singularities along the body centerline. The two singularities used here are the Stokeslet, which is the singular force acting at a point, and the doublet, which is the superposition of a source and a sink (similar to the doublet in potential flow theory).

Both Tillett (21) and Batchelor (24) made use of this method to solve for the drag on straight axisymmetric slender bodies while Lighthill (25) applied slender body theory to the movement of micro-organisms.

In Lighthill's work, the slender body is the flagellum which propels the micro-organism. He provided a theorem which relates the fluid velocity at the surface of the flagellum to the distribution of singularities along its centerline. The theorem allows curvature, provided that the radius of curvature R is many times larger than the cross-section radius a. The present work will make use of this theorem in a modified form to account for a different far field flow. That is, in Lighthill's case, the flagellum was moving in quiescent fluid, while in the present case, a stationary ring is immersed in a uniform flow. This modification of boundary conditions must be incorporated in Lighthill's theorem so that it may be applied to obtain the drag on a ring.

The study of an isolated ring in a uniform flow will show that the drag on it, averaged over all directions, has the same form as the drag on a sphere, and the radius of the equivalent sphere can be found by matching the two drags. The notion of an equivalent sphere is useful in determining the permeability through the rings since a solution to the problem of a cubic lattice of spheres is known. Since the previous review of theories for porous media treated only arrays of rods and not spheres, and since theories of the latter will be used in the analysis of this thesis, it is necessary to review here the prior work which has been done on these arrays.

The Stokes equation for flow past a cubical array of spheres has been solved by Hasimoto (18) using the Fourier series technique described previously. He found the permeability to be

$$\frac{k}{A^2} = \frac{2}{9}\frac{1}{\phi}(1 - 1.7601\,\phi^{1/3} + \phi + O(\phi^2))$$

where A is the sphere radius. Zick and Homsy (26) and Sangani and Acrivos (27) have obtained numerical solutions to this problem which completely agree with Hasimoto's result to the order given.

The average drag on a ring will replace the drag on a sphere in Hasimoto's cubical array to obtain the limiting case, for small ϕ, when rings are separated by many ring radii.

CHAPTER III

MATHEMATICAL TREATMENT OF THE MODEL

This chapter, dealing with the mathematical treatment of the model itself, is divided into three sections. The first deals with slender body theory, the second is concerned with its application to the drag on an isolated ring, while the third concentrates on the interactions among rings of the matrix.

SECTION A: SLENDER BODY THEORY

The basic concepts of slender body theory are introduced and developed in this section. As discussed before, the approach taken by Batchelor (24), Tillett (21) and Lighthill (25) makes use of the superposition of fundamental singular solutions. This approach will be referred to here as Lighthill's method mainly because it is his theorem which will be used to solve for the drag on a ring. The alternate method presented by Cox is equally valid, but the use of singularity solutions is more widespread. However, Cox's results will be used to verify some of the results obtained in the present work.

Lighthill's method makes use of singular solutions to generate a flow field similar to the one obtained when a slender body is immersed in a uniform flow. How well the flow field conforms to the actual one determines the accuracy of the solution. To simulate uniform flow past a given slender body, singularities such as Stokeslets and doublets are distributed along a curve (the body centerline) and a uniform flow is superimposed. The superposition of these fields is a solution which satisfies the Stokes equation; and when appropriate boundary conditions are satisfied, the flow field past a slender body is duplicated. Only two singularities are necessary in slender body theory: the Stokeslet and the doublet.

The Stokeslet is defined by Chwang & Wu (28) as the fundamental solution, to the inhomogeneous Stokes equation, which is associated with a singular point force. The inhomogeneous Stokes equation is given by

$$\nabla P = \mu \nabla^2 \bar{u} + \bar{F}_s$$

where $\bar{F}_s$ is an external force per unit volume. A singular point force located, say, at the origin is defined as

$$\bar{F}_s = \bar{f} \delta (\bar{x}) \tag{6}$$

where $\bar{f}$ is a force vector proportional to the strength of the Stokeslet, δ is the three-dimensional Dirac delta function and $\bar{x}$ is the position vector in a three-dimensional Euclidean space. The Stokeslet strength is $\bar{f}/8\pi\mu$; here, however, to simplify notations, the force vector $\bar{f}$ will be used to characterize this strength. The solution of the above Stokes equation can be found in a straightforward manner, giving the velocity and pressure fields associated with a Stokeslet:

$$\begin{aligned} \bar{U}_s &= \frac{1}{8\pi\mu} \left(\frac{f}{x} + \frac{(\bar{f} \cdot \bar{x})\bar{x}}{x^3} \right) \\ P_s &= \frac{1}{4\pi} \frac{\bar{f} \cdot \bar{x}}{x^3} \end{aligned} \tag{7}$$

where x is the magnitude of the position vector $\bar{x}$ and the pressure P_s is measured relative to the pressure at infinity. $\bar{U}_s$ and P_s are added to the undisturbed velocity and pressure fields. The velocity and pressure fields resulting from a Stokeslet immersed in a uniform flow, for example, are given by $\bar{U}_s + \bar{U}$ and $P_s + P_0$, where $\bar{U}$ and P_0 are the constant velocity and pressure of the uniform flow. Because of linearity, the resultant velocity and pressure fields satisfy Stokes equation.

The second singularity treated here is the doublet which is a solution derived from high Reynolds number potential flow theory. All solutions of potential flow theory are governed by the equation

$$\nabla^2 \bar{u} = 0.$$

When the Laplacian of the velocity is zero, the pressure gradient must also be zero to satisfy the Stokes equation. Potential flow theory shows that the doublet is the superposition of a sink and a source, and its solution is well known. The velocity field associated with this solution is

$$\bar{U}_D = \frac{-\bar{\delta}}{x^3} + 3\,\frac{(\bar{\delta}\cdot\bar{x})\bar{x}}{x^5} \qquad (8)$$

where $\bar{\delta}$ is the strength of the doublet. The pressure field, of course, remains unaltered.

The doublet's spatial influence decreases rapidly as $\frac{1}{x^3}$ giving this singularity a very local influence on the flow. The Stokeslet's influence, on the other hand, is much greater because it decreases as $\frac{1}{x}$. Doublets and Stokeslets will be used together in this work and this allows a simplifying assumption when considering a Stokeslet and doublet at a distant point. In this case, only the Stokeslet needs to be considered since the influence of the doublet has long since become negligible. This assumption will be used when studying the influence of one ring on another.

Whenever a Stokeslet is placed in a flow field, it must be accompanied by a doublet centered at the same point. This combination creates a stream surface S_b surrounding both singularities which describes the shape of the body for which a solution is sought. Stream surfaces in three dimensional flow are analogous to stream-lines in two dimensional flow; the velocity on a stream surface is of constant magnitude. Boundary conditions are met by matching the velocity of the stream surface with the required velocity of the body, while the far field condition is given by the original flow field which hosts the singularities. This gives the distribution of Stokeslet and doublet strengths as a function of a general point s on the centerline of the body.

The case of a single Stokeslet-doublet combination immersed in a uniform flow yields a spherical stream surface envelope, thereby leading to Stokes' drag law for a sphere. A distribution of these pairs along a line, however, creates an elongated envelope, giving the solution for the flow past an oblate spheroid. When this line is long and curved, the distribution of singularities creates a long, thin envelope representative of a slender body.

The strengths of these singularities are responsible for the force exerted by the body on the fluid. This force is obtained by the integration of pressure and viscous forces over the body's surface S_b:

$$\bar{F} = \int_{S_b} (P\bar{n} - \bar{\bar{\tau}} x \bar{n}) dS \qquad (9)$$

where $\bar{n}$ is the unit outward and normal and $\bar{\bar{\tau}}$ is the viscous stress tensor given by

$$\tau_{ij} = \frac{\mu}{2} \left(\frac{\partial ui}{\partial xj} + \frac{\partial uj}{\partial xi} \right)$$

In the last expression, the subscripts denote the components of $\bar{u}$ and $\bar{x}$ in Cartesian coordinates. By making use of the divergence theorem and the above relation, equation 9 can be expressed as an integral over the body's volume V_b. This integral is found to be

$$\bar{F} = \int_{V_b} (\nabla P - \mu \nabla^2 \bar{u}) dV$$

The inhomogeneous Stokes equation can be substituted in this equation:

$$\bar{F} = \int_{V_b} \bar{F}_s \, dV.$$

However, $\bar{F}_s$, given by equation 6, is zero except on the centerline where it takes on the value f(s); thus

$$\bar{F} = \int_L \bar{f}(s) ds \qquad (10)$$

where L is the length of the centerline. This equation says that the force exerted by the body on the neighbouring fluid then is given by an integration of the Stokeslet strength distribution $\bar{f}(s)$ along the centerline.

The drag is defined as the force exerted on a body in the streamwise direction. The drag $\bar{D}$ is therefore given by

$$\bar{D} = (-\bar{F}.\bar{U})\frac{\bar{U}}{U^2}$$

where U is the magnitude of the uniform velocity $\bar{U}$.

The doublet distribution does not directly contribute to the drag since it does not alter the pressure field, nor does it contribute any external forces. However, the doublet distribution affects the Stokeslet strengths which means that the doublet distribution indirectly affects the drag.

In order to find the drag on a body, then, the Stokeslet strength distribution must be obtained. This distribution is found by matching the velocity of the stream surface to that of the body which, in the present work, is zero since the rings are at rest. The velocity at a given point on S_b is given by the sum of the Stokeslet and doublet flow fields, $\bar{U}_s$ and $\bar{U}_D$, and uniform flow $\bar{U}$. All singularities along the centerline must contribute to the velocity of S_b, this the flow field associated with singularities at all points of the centerline must be summed yielding an integral expression. The no-slip condition at S_b is written:

$$\bar{U} + \int_L (\bar{U}_s(\bar{r}) + \bar{U}_D(\bar{r}))ds = 0$$

where $\bar{r}(s)$ is the distance from a general point s of the centerline to a given point on S_b. The above equation gives the following complicated expression when equations 7 and 8 are used to give $\bar{U}_s$ and $\bar{U}_D$:

$$\bar{U} + \int_L \left[\frac{1}{8\pi\mu}\left(\frac{\bar{f}}{r} + \frac{(\bar{f}.\bar{r})\bar{r}}{r^3}\right) + \left(-\frac{\bar{\delta}}{r^3} + \frac{3(\bar{\delta}.\bar{r})\bar{r}}{r^5}\right)\right] ds = 0 \qquad (11)$$

Because $\bar{U}_s$ and $\bar{U}_D$ have cylindrical symmetry, the no-slip condition is met around the entire perimeter of the cross-section. The strengths $\bar{f}$ and $\bar{\delta}$ are found by satisfying equation 11 for all cross-sections. Evaluation of this integral is difficult and Lighthill (27) offered a simplification.

It will be recalled that Lighthill's problem differs from the present one in that his micro-organisms were moving in a quiescent fluid. In order to use his method, some modifications must be made, specifically, a uniform flow must be added and the surface of the body must be stationary.

The theorem of Lighthill which relates the Stokeslet and doublet strength distributions to the non-slip boundary condition can now be stated in a form suitable for the present work.

THEOREM: If $\bar{f}(s)$ is the force per unit length which a slender body exerts on a fluid, where s signifies length measured along the centerline of the body, as shown in Figure 6, then the surrounding flow field can be represented by a distribution of Stokeslets and doublets along the centerline, of respective strengths $\bar{f}(s)$ and $\frac{-a^2\bar{f}_n(s)}{16\pi\mu}$ per unit length, immersed in a uniform flow of velocity $\bar{U}$. Here $\bar{f}_n(s)$ is a vector perpendicular to the centerline obtained by resolving $\bar{f}(s)$ onto the plane normal to the centerline. The velocity around the perimeter of a particular cross-section passing through $s = s_0$ is given by:

$$\bar{U} + \frac{\bar{f}_n(s_0)}{4\pi\mu} + \frac{1}{8\pi\mu}\int_{r(s)>r_0} \left(\frac{f(s)}{r} + \frac{(\bar{f}(s).\bar{r})\bar{r}}{r^3}\right) ds \qquad (12)$$

where $r_0 = \frac{a\sqrt{e}}{2} = 0.82a$ with a being the body radius and $\bar{r}$ the position vector of magnitude r from s to s_0 (Figure 6). The integration is carried out along the entire centerline except for a small region of length r_0 on either side of s_0.

A sketch of the proof of this theorem can be found in Lighthill (27) where it is pointed out that equation 12 is accurate to order $\frac{a}{L}$ or $\frac{a}{R}$, where L is a characteristic length or R is a characteristic radius of curvature, whichever is bigger.

In the problems solved in this thesis, the bodies are at rest so that for each cross-section s_0, equation 12 must be set equal to zero or

$$\bar{U} + \frac{\bar{f}_n(\bar{s}_0)}{4\pi\mu} + \frac{1}{8\pi\mu}\int_{r>r_0} \left(\frac{\bar{f}(s)}{r} + \frac{(\bar{f}(s).\bar{r})\bar{r}}{r^3}\right) ds = 0 \qquad (13)$$

Equation 13 is equivalent to equation 11, according to Lighthill's theorem; however, the former has simpler integrations to carry out and is therefore preferred when setting out to calculate the Stokeslet distribution $\bar{f}(s)$.

As given, equation 13 is of limited use because, taken literally, it requires knowledge of the distribution sought. Lighthill circumvented this problem by making assumptions about the form of this distribution. His principal assumption is that the vector $\bar{f}(s)$ is proportional to the far field velocity $\bar{U}$ at all points where the centerline is either aligned with $\bar{U}$ or normal to it. Two separate constants of proportionality are thus introduced: T, when the centerline is tangent to $\bar{U}$, and γT, when the centerline is normal to it. γ is therefore effectively the ratio of drags. When $\bar{U}$ and $\bar{f}(s)$ are decomposed into normal and tangential parts, the same two constants of proportionality are used to give the functional form of the singularity distribution.

The vector $\bar{f}_t(s)$ is defined as the component of $\bar{f}(s)$ tangent to the centerline (Figure 6) such that

$$\bar{f} = \bar{f}_t + \bar{f}_n \tag{14}$$

The velocity $\bar{U}$ is decomposed in a similar fashion,

$$\bar{U} = \bar{U}_t + \bar{U}_n \tag{15}$$

where $\bar{U}_t$ is tangent to the centerline and $\bar{U}_n$ is normal to it. At each point s along the centerline, then, the strength $\bar{f}(s)$ is chosen such that

$$\bar{f}_t = -T\bar{U}_t \tag{16}$$

and

$$\bar{f}_n = -\gamma T\bar{U}_n \tag{17}$$

The ratio γ is expected to be close to 2, because this is the value for straight rods, either isolated or arranged in regular arrays (16, 20, 21).

Equations 13 through 17 can now be used to solve for the Stokeslet strength distribution $\bar{f}(s)$. This distribution corresponds to the force per unit length which a body exerts on the circumambient liquid. This leads in a straightforward manner to the drag $\bar{D}$ on the body which is given by an expression similar to equation 10:

$$\bar{D} = (-[\int_L \bar{f}(s)\, ds].\bar{U})\, \frac{\bar{U}}{U^2} \qquad (18)$$

with the minus sign needed since the drag, by definition, is the force exerted by the fluid on the body, i.e., $\bar{f}$ is in opposite direction to $\bar{U}$. This theory is now used to calculate the drag on a ring in a uniform flow.

SECTION B: FORCES ON A RING IN A UNIFORM FLOW

This section deals with the mathematical development to find the drag on a ring immersed in a uniform flow. The flow normal to the ring is treated first, followed by the case of flow aligned with it. These solutions are then used to find the drag on a ring at any orientation. Finding the average drag on the ring, over all orientations, and determining the equivalent sphere are described in the last subsection.

i) FLOW NORMAL TO A RING

A definition sketch of flow normal to and aligned with the ring is given by Figure 7, which also serves to define some of the parameters for the analysis. In the normal flow case, the tangent to the ring centerline is always perpendicular to the flow velocity $\bar{U}$ and therefore the tangential component of velocity is zero. According to the assumption made in section A, then, the Stokeslet strength is aligned with $\bar{U}$ such that

$$\bar{f} = -\gamma T \bar{U}.$$

Since the uniform velocity vector is independent of its position in the flow field, the vector $\bar{f}$ does not depend on its position on the centerline, i.e., the strength of the singularities, $\bar{f}$, is constant around the ring.

To use Lighthill's theorem, or equation 13, it is necessary to describe the ring mathematically. R denotes the radius from the centerline of the ring to its center and θ is angle in the y-z plane measured from the y axis as shown in Figure 7. The position of a point s on the centerline of the ring, in the y-z plane, is given in a Cartesian coordinate system by

$$R \begin{bmatrix} 0 \\ \cos\theta \\ \sin\theta \end{bmatrix} \tag{19}$$

The zero velocity boundary condition must be met at the surface of the ring. A cross-section passing through the particular point $s_0 = s(\theta_0)$, where θ_0 is an arbitrary but fixed angle, is considered. Independence with respect to θ_0 will then be required. The point s_0 is given by

$$R\begin{bmatrix}0\\ \cos\theta_0\\ \sin\theta_0\end{bmatrix}$$

and the vector $\bar{r}$ going from s to s_0 is

$$\bar{r} = R\begin{bmatrix}0\\ \cos\theta_0-\cos\theta\\ \sin\theta_0-\sin\theta\end{bmatrix} \qquad (20)$$

This vector represents the distance from the singularities located at s to the point s_0. The magnitude of this vector is given by

$$r = R\sqrt{2(1-\cos\alpha)} \qquad (21)$$

where the angle α is

$$\alpha = \theta-\theta_0. \qquad (22)$$

Since the velocity $\bar{U}$ is normal to the ring, it must be chosen along the x-axis or

$$\bar{U} = U\begin{bmatrix}1\\ 0\\ 0\end{bmatrix}$$

where U is the magnitude of $\bar{U}$. Since $\bar{r}$ is in the plane of the ring, $\bar{r}$ is perpendicular to $\bar{f}$ and thus their dot product is zero. Equation 13, then, has only the following component remaining (in the x-axis),

$$U - \frac{T\gamma U}{4\pi\mu} - \frac{T\gamma U}{8\pi\mu} I_a = 0 \qquad (23)$$

with

$$I_a = \int_{r>r_0} \frac{ds}{r}.$$

The integral I_a is the contour integral of $\frac{1}{r}$ around the centerline of the ring, which is a circle. The element ds, then, is simply R$d\alpha$ and the limits of integration are α_0 and $2\pi-\alpha_0$ where $\alpha_0 = \frac{\sqrt{e}}{2}\frac{a}{R}$ as required by Lighthill's theorem. Since the domain of the line integral I_a is a circle minus a small region around s_0, the limits of integration can be changed to two domains on either side of S_0, one ranging from $-\pi$ to α_0 and the other from α_0 to π. The integral I_a becomes

$$I_a = \frac{1}{\sqrt{2}} \int_{-\pi}^{-\alpha_0} \frac{d\alpha}{\sqrt{1-\cos\alpha}} + \frac{1}{\sqrt{2}} \int_{\alpha_0}^{\pi} \frac{d\alpha}{\sqrt{1-\cos}} .$$

The integral is even and I_a becomes

$$I_a = \sqrt{2} \int_{\alpha_0}^{\pi} \frac{d\alpha}{\sqrt{1-\cos\alpha}} .$$

Using a change of variables, the integral is straightforwardly found to be

$$Ia = 2(\ln \frac{8R}{a} - \frac{1}{2}). \tag{24}$$

When this result is substituted into equation 23, then

$$\gamma T = \frac{4\pi\mu}{\ln\frac{8R}{a} + \frac{1}{2}}. \tag{25}$$

The strength of the Stokeslet distribution is therefore

$$\bar{f} = \frac{-4\pi\mu}{\ln\frac{8R}{a} + \frac{1}{2}} \bar{U}. \tag{26}$$

The drag on the ring, $\bar{F}_1$, calculated using equation 18, is

$$\bar{F}_1 = \int_0^{2\pi} \frac{4\pi\mu}{\ln\frac{8R}{a} + \frac{1}{2}} \bar{U}\, Rd\alpha .$$

The drag on a ring normal to the flow becomes

$$\bar{F}_1 = \frac{8\pi^2\mu\bar{U}R}{\ln\frac{8R}{a} + \frac{1}{2}} . \tag{27}$$

The result is accurate to order a/R according to Lighthill's theorem, and is therefore valid only for small values of $\frac{a}{R}$. The same calculation was made using Cox's method (20) and the result was found to be the same, but this time the neglected term was of order $(\ln \frac{R}{a})^{-3}$.

This solution can be compared to that for a straight rod normal to the flow to show the influence of curvature, for this is the only parameter which differs between the two solutions. This rod problem is calculated in appendix A, where the drag $\bar{F}_{rod}$ is found to be

$$\bar{F}_{rod} = \frac{8\pi^2 \mu \bar{U} R}{\ln\frac{8R}{a} - .048}$$

for a rod of length $2\pi R$, and of radius a immersed in a uniform flow. Cox also performed this calculation and obtained the same result. The influence of curvature is therefore seen in the second order term and the two solutions approach each other as R tends to infinity.

ii) FLOW ALIGNED WITH A RING

The problem of calculating the drag on a ring aligned with the flow is more complicated since the velocity $\bar{U}$ is now at different angles to the centerline. The aligned flow situation is treated here keeping the ring exactly as it was in subsection i) and changing the flow direction, as shown in Figure 7. All parameters associated with the ring are carried over to this new problem, particularly the vector $\bar{r}$ which is defined by equations 20 through 22. The velocity can be placed anywhere in the y-z plane because of circular symmetry. The uniform flow velocity vector can therefore be chosen along the y-axis without loss of generality.

This velocity vector is

$$\bar{U} = U \begin{bmatrix} 0 \\ 1 \\ 0 \end{bmatrix} \tag{28}$$

where U is the magnitude of $\bar{U}$ as before. The decompositions of $\bar{U}$ into components normal and tangential to the ring's centerline yields:

$$\bar{U}_n = U\cos\theta \begin{bmatrix} 0 \\ \cos\theta \\ \sin\theta \end{bmatrix}$$

and

$$\bar{U}_t = -U\sin\theta \begin{bmatrix} 0 \\ -\sin\theta \\ \cos\theta \end{bmatrix}$$

The same components of the Stokelet strength distribution can now be given using the assumptions and procedure outlined in section A, which are summarized mathematically in equations 16 and 17:

$$\bar{f}_n = -\gamma T\bar{U}_n \quad \text{and} \quad \bar{f}_t = -T\bar{U}_t$$

Substitution of $\bar{U}_n$ and $\bar{U}_t$ into these relations yields

$$\bar{f}_n = -T\gamma\, U\cos\theta \begin{bmatrix} 0 \\ \cos\theta \\ \sin\theta \end{bmatrix} \tag{29}$$

and

$$\bar{f}_t = TU\,\sin\theta \begin{bmatrix} 0 \\ -\sin\theta \\ \cos\theta \end{bmatrix} \tag{30}$$

The Stokeslet strength distribution $\bar{f}$ is found by adding $\bar{f}_n$ and $\bar{f}_t$ (equation 14), and is therefore

$$\bar{f} = -TU \begin{bmatrix} 0 \\ (1 + (\gamma-1)\cos^2\theta) \\ (\gamma-1)\sin\theta\cos\theta \end{bmatrix} \tag{31}$$

The procedure now is the same as in subsection i). Equation 13 is used to find the constants γ and T. This equation is written:

$$\bar{U} + \frac{\bar{f}_n(\theta_0)}{4\pi\mu} + \frac{\bar{I}_1 + \bar{I}_2}{8\pi\mu} = 0 \tag{32}$$

where

$$\bar{I}_1 = \int_{-\pi}^{-\alpha_0} \frac{\bar{f}}{r} R d\alpha + \int_{\alpha_0}^{\pi} \frac{\bar{f}}{r} R d\alpha \tag{33}$$

and

$$\bar{I}_2 = \int_{-\pi}^{-\alpha_0} \frac{(\bar{f}.\bar{r})\bar{r}}{r^3} R d\alpha + \int_{\alpha_0}^{\pi} \frac{(\bar{f}.\bar{r})\bar{r}}{r^3} R d\alpha \tag{34}$$

where $\bar{r}$, α and α_0 are defined in subsection i) and $\bar{r}$ and α are shown in Figure 7. The x component of each vector in equation 32 is zero, which means that results are obtained only for the y and z directions. The y component of equation 32 is treated first and is given by:

$$U + \frac{f_{ny}(\theta_0)}{4\pi\mu} + \frac{I_{1y} + I_{zy}}{8\pi\mu} = 0 \tag{35}$$

where f_{ny}, I_{1y} and I_{2y} are the y components of $\bar{f}_n$, $\bar{I}_1$ and $\bar{I}_2$ respectively. I_{1y} requires the y component of $\bar{f}$ expressed in terms of the angles α and θ_0 and the result is

$$I_{1y} = \frac{-TU}{\sqrt{2}} [(\cos^2\theta_0 + \gamma\sin^2\theta_0) I_a + ((\gamma - 1)\cos 2\theta_0) I_b] \tag{36}$$

where I_a is given by equation 24 and I_b is given by

$$I_b = \int_{-\pi}^{-\alpha_0} \frac{\cos^2\alpha}{1-\cos\alpha} d\alpha + \int_{\alpha_0}^{\pi} \frac{\cos^2\alpha}{1-\cos\alpha} d\alpha .$$

The integral in I_b is even and the integral becomes

$$I_b = 2 \int_{\alpha_0}^{\pi} \frac{\cos^2\alpha}{\sqrt{1-\cos\alpha}} d\alpha .$$

I_b is integrated using a change of variables to give

$$I_b = 2\sqrt{2} \left(\ln \frac{8R}{a} - \frac{11}{6} \right) \qquad (37)$$

where the value $\alpha_0 = \frac{\sqrt{e}}{2} \frac{a}{R}$ has been used. Equations 24 and 37 are substituted in relation 36 to give:

$$I_{1y} = - TU \left(\cos 2\theta_0 (\gamma-1) \left(\ln \frac{8R}{a} - \frac{19}{6} \right) + (\gamma+1) \left(\ln \frac{8R}{a} - \frac{1}{2} \right) \right) . \qquad (38)$$

To calculate the other integral in equation 35, I_{2y}, the value of $(\bar{f}.\bar{r})$ is needed. This dot product is expressed in terms of the angles α and θ_0 as:

$$(\bar{f}.\bar{r}) = TUR \left[(-1 + \gamma\cos\alpha - (\gamma-1) \cos^2\alpha)\cos\theta_0 + ((\gamma-1)\cos\alpha - \gamma)\sin\alpha \sin\theta_0 \right] .$$

The y component of $(\bar{f}.\bar{r})\bar{r}$ consists of trigonometric functions of α which are either odd or even. The odd terms do not contribute to the result since the integration from $-\pi$ to $-\alpha_0$ cancels that from α_0 to π. In the calculation of I_{2y}, then, only the even terms need to be considered. These give:

$$I_{2y} = \frac{TU}{2\sqrt{2}}\left[[-\gamma+(\gamma-1)\cos^2\theta_0]\ I_{c_0}+[\gamma+\cos 2\theta_0]\ I_{c_1}+[\gamma-(3\gamma-1)\cos^2\theta_0]\ I_{c_2} + [(\gamma-1)\cos 2\theta_0]\ I_{c_3}\right]$$

with

$$I_{c_n} = 2\int_{\alpha_0}^{\pi} \frac{\cos^n\alpha}{(1-\cos\alpha)^{3/2}}d\alpha\ ;\ n = 0,\ 1,\ 2,\ 3.$$

The integrals I_{c_n} are calculated straightforwardly:

$$\begin{aligned} I_{c_0} &= 2\left(\zeta + \frac{1}{2}\ln\frac{8R}{a} - \frac{1}{4}\right)\\ I_{c_1} &= 2\left(\zeta - \frac{3}{2}\ln\frac{8R}{a} + \frac{3}{4}\right)\\ I_{c_2} &= 2\left(\zeta - \frac{7}{2}\ln\frac{8R}{a} + \frac{23}{4}\right)\\ I_{c_3} &= 2\left(\zeta - \frac{11}{2}\ln\frac{8R}{a} + \frac{113}{12}\right) \end{aligned}$$

with $\zeta = \dfrac{1}{1-\cos\alpha_0}$.

The values for the integrals I_{c_n} are substituted into the expression for I_{2y}. The coefficients of ζ are found to add up to zero in all cases and the final value of I_{2y} is

$$I_{2y} = TU\ \left[\left(\ln\frac{8R}{a} - \frac{17}{6} + \frac{\gamma}{3}\right)\cos 2\theta_0 - \ln\frac{8R}{a} + \frac{3}{2} - \gamma\right] \qquad (39)$$

Substitution of equations 38 and 39 into equation 35 gives a relationship between and T as a function of the arbitrary angle θ_0:

$$U - \frac{TU}{8\pi\mu}\left[\cos 2\theta_0\left(\left(\ln\frac{8R}{a} - \frac{5}{2}\right) - 2\left(\ln\frac{8R}{a} - 3\right) + \gamma\left(\left(\ln\frac{8R}{a} + \frac{3}{2}\right) + 2\left(\ln\frac{8R}{a} - 1\right)\right)\right]\right. = 0. \tag{40}$$

It was stated in subsection i) that θ_0 is the angle giving the location on the ring where the non-slip boundary condition is imposed. This boundary condition must be valid everywhere along the ring. Hence equation 40 must be independent of θ_0 and thus the coefficient of $\cos 2\theta_0$ must be zero. The value for γ is therefore:

$$\gamma = 2\,\frac{\ln\frac{8R}{a} - 3}{\ln\frac{8R}{a} - \frac{5}{2}}\,, \tag{41}$$

and the value of T can be calculated by substitution of equation 41 into equation 40:

$$T = \frac{2\pi\mu}{\ln\frac{8R}{a} - \left[\frac{2}{\ln\frac{8R}{a} - \frac{5}{2}}\right]}\,. \tag{42}$$

Equation 32 must also be satisfied on the z axis. The method of calculation is identical. Furthermore, since all unknowns have been calculated, this solution can serve only to verify calculations done on the y axis. The z components of $\bar{I}_1$ and $\bar{I}_2$ are given by:

$$I_{1z} = \frac{-TU}{\sqrt{2}} (\gamma - 1)(2I_b - I_a) \sin\theta_0 \cos\theta_0$$

$$I_{2z} = \frac{TU}{\sqrt{2}} [(\gamma-1)I_{c_0} + 2I_{c_1} - (3\gamma-1)I_{c_2} + 2(\gamma-1)I_{c_3}]$$

where every integral involved has already been calculated. The z component of equation 32 then becomes

$$\frac{TU \sin\theta_0 \cos\theta_0}{4\pi\mu} \left((\gamma-1)(\ln\frac{8R}{a} - \frac{19}{6}) + \ln\frac{8R}{a} - \frac{17}{6} - \frac{2}{3}\gamma \right) = 0$$

When this equation is solved for γ, the result is equation 41. The z component of equation 32 is then satisfied, and the non-slip boundary condition is now met in all directions, all around the ring.

At this point, it is useful to compare this solution to that obtained in subsection i). From equations 41 and 42, the product γT for the case where the flow is aligned with the ring is

$$\gamma T = \frac{4\pi\mu}{\ln\frac{8R}{a} + \frac{1}{2}\left[\frac{\ln\frac{8R}{a} - 4}{\ln\frac{8R}{a} - 3}\right]}$$

For the prior case of flow normal to the ring, the same product is given by equation 25:

$$\gamma T = \frac{4\pi\mu}{\ln\frac{8R}{a} + \frac{1}{2}}$$

The values of γ and T are therefore not uniquely defined, and thus the singularity strengths depend upon orientation. However, the first two terms in an expansion of powers of $(\frac{1}{\ln(8R/a)})$ are identical, and therefore γ and T can be taken as independent of flow direction for small values of $\frac{a}{R}$. Thus when terms of $(\ln\frac{8R}{a})^{-3}$ or smaller are neglected, the values of γ and T are

$$\gamma = 2 - \frac{1}{\ln\frac{8R}{a}} - \frac{\frac{2}{5}}{(\ln\frac{8R}{a})^2} \tag{43}$$

and

$$T = \frac{2\pi\mu}{\ln\frac{8R}{a}} \tag{44}$$

for all far field flow orientations. The drag on a ring aligned with the flow, $\bar{F}_2$, is given by equation 18, which in this case becomes

$$\bar{F}_2 = T\bar{U}R\int_0^{2\pi}\begin{bmatrix}0\\1+(\gamma-1)\cos^2\theta\\(\gamma-1)\cos\theta\sin\theta\end{bmatrix}d\theta\ ,$$

which, on integrating, yields

$$\bar{F}_2 = (\gamma+1)\ T\pi R\bar{U}. \tag{45}$$

When the values of γ and T from equations 43 and 44 are substituted into the above equation, the result is:

$$\bar{F}_2 = \frac{6\pi^2\mu\bar{U}R}{\ln\frac{8R}{a} + \frac{1}{3}} \tag{46}$$

where the order of the first neglected term is $\frac{1}{(\ln\ 8R/a)^3}$. Cox has calculated the drag for this same situation using his inner and outer expansion technique, and the result is identical.

A comparison of this drag to the drag on a straight rod has no meaning this time.

iii) FLOW AT ANY ANGLE TO A RING

The case treated in this subsection is the general case of flow past an isolated ring. A uniform flow approaches the ring from any direction and has components along all three coordinate axes:

$$\bar{U} = \begin{bmatrix} U_x \\ U_y \\ U_z \end{bmatrix}$$

The ring is placed exactly as before (Figure 8) and the components of velocity normal and tangential to the centerline are readily calculated. They are respectively:

$$\bar{U}_n = \begin{bmatrix} U_x \\ U_y \cos^2\theta + U_z \sin\theta \cos\theta \\ U_y \cos\theta \sin\theta + U_z \sin^2\theta \end{bmatrix}$$

and

$$\bar{U}_t = \begin{bmatrix} 0 \\ U_y \sin^2\theta - U_z \sin\theta \cos\theta \\ -U_y \sin\theta \cos\theta + U_z \cos^2\theta \end{bmatrix}$$

Again, relations 16 and 17 from section A are used to obtain the Stokeslet strength vector:

$$\bar{f} = -T \begin{bmatrix} \gamma U_x \\ U_z(1+(\gamma-1)\cos^2\theta) + U_z(\gamma-1)\cos\theta\ \sin\theta \\ U_z(\gamma-(\gamma-1)\cos^2\theta) + U_z(\gamma-1)\cos\theta\ \sin\theta \end{bmatrix}$$

As before, integration of $-\bar{f}$ around the contour of the ring gives the force exerted on the ring by the surrounding fluid. This force, which is not aligned with the velocity vector, is given by $\bar{F}'$ where

$$\bar{F}' = \pi R \begin{bmatrix} 2\ TU_x \\ (\gamma+1)TU_y \\ (\gamma+1)TU_z \end{bmatrix} \tag{47}$$

Here, the values of γ and T are known from equations 43 and 44 because it was shown that these relations are valid for all flow orientations. The expression for $\bar{F}'$ is then

$$\bar{F}' = 2\pi^2\mu R \begin{bmatrix} \dfrac{4U_x}{\ln\dfrac{8R}{a} + \dfrac{1}{2}} \\ \dfrac{3U_y}{\ln\dfrac{8R}{a} + \dfrac{1}{3}} \\ \dfrac{3U_z}{\ln\dfrac{8R}{a} + \dfrac{1}{3}} \end{bmatrix} \tag{48}$$

For the special case of flow normal to and aligned with the ring, $\bar{U} = (U,0,0)$ and $\bar{U} = (0,U,0)$ respectively, $\bar{F}'$ reduces to the known results $\bar{F}_1$ and $\bar{F}_2$ (equations 37 and 46).

This force is generally not in the direction of flow which implies that the ring generates a lift, i.e., there is a component of force perpendicular to the streamwise direction.

In a random arrangement of rings, every flow direction is equally probable. For each flow direction which gives a positive lift, there exists an equally probable flow direction which gives a negative lift, so that the net lift is zero. This reasoning leads to the conclusion that the force on the ring is, on average, aligned with the flow. To find this average force, the drag, which is the streamwise component of the force $\bar{F}'$ given by

$$\bar{F} = \frac{(\bar{F}'.\bar{U})}{U^2}\,\bar{U}\ , \tag{49}$$

is needed. Substitution of equation 42 into 49 gives the drag:

$$\bar{F} = \pi RT\ (\gamma + 1 + (\gamma - 1)\ \frac{U_x^2}{U^2})\ \bar{U} \tag{50}$$

where use has been made of the identity

$$U^2 = U_x^2 + U_y^2 + U_z^2 .$$

iv) THE AVERAGE DRAG ON A RING

The porous medium model which will eventually be considered is comprised of a large number of rings at random orientations. The force on each ring varies with orientation but as the number of rings tends toward infinity, the average drag can be used since it is the drag on the total system which is of interest here. This average is now calculated.

In the expression giving the drag for any flow direction, equation 50, the only orientation-dependent quantity is $\frac{U_x^2}{U^2}$. The average drag is therefore

$$<\bar{F}> = \pi RT(\gamma + 1 + [\gamma - 1] < \frac{U_x^2}{U^2} >)\bar{U} \tag{51}$$

where the brackets, <> , are understood to denote averaging. The best way to determine $< \frac{U_x^2}{U^2} >$ is by expressing the velocity vector in terms of its magnitude, U, and two spatial angles, ϕ and Ψ, defined as the angles of a spherical coordinate system, as shown in Figure 8. The component U_x is then

$$U_x = U\cos\Psi\sin\phi$$

and therefore

$$< \frac{U_x^2}{U^2} > = \frac{1}{4} \int_0^{2\pi} \int_0^{\pi} (\cos^2\Psi\sin^2\phi)\sin\phi\, d\phi\, d\Psi$$

where $\sin\phi d\phi d\Psi$ is the element of integration in spherical coordinates. This integration gives

$$< \frac{U_x^2}{U^2} > = \frac{1}{3} \quad ,$$

which is the result to be expected on intuitive grounds. Equation 51 can now be re-written to give the average drag:

$$< \bar{F} > = \frac{20\pi^2\mu R\bar{U}}{3G} + 0\left(\frac{1}{(\ln\frac{8R}{a})^3}\right) \tag{52}$$

with
$$G = \ln\frac{8R}{a} + \frac{2}{5} \tag{53}$$

There exists no result in the literature to which this result can be compared. However, the comparison with a straight rod averaged over flow direction in a similar manner shows once again that the radius of curvature affects the second term. This calculation is carried out in appendix A. The result for a rod of length $2\pi R$ is

$$<\bar{F}_{rod}> = \frac{\frac{20}{3}\pi^2 R\bar{U}\mu}{\ln\frac{8R}{a} - 0.25}$$

Here again, the solutions for the straight rod and the curved ring share the first term in the expansion.

As a result of spatial averaging, the ring problem takes on a spherical symmetry. Under these conditions, comparison to the drag on a sphere is appropriate. This drag is given by Stokes' drag law:

$$\bar{D}_s = 6\pi\mu\bar{U}A \tag{54}$$

where $\bar{D}_s$ is the drag on a sphere of radius A. By equating $\bar{D}_s$ to $<\bar{F}>$, an equivalent sphere radius can be found. This is the radius of the sphere whose drag is equal to the average drag on a ring. The calculation gives

$$A = \frac{\frac{10}{9}\pi R}{G} \tag{55}$$

This result, like previous ones, neglects all terms of order $(\ln\frac{8R}{a})^{-3}$ or smaller. For values of $\frac{R}{a}$ close to 10, the neglected term is about 10% of the leading term and thus 10 is considered to be the lowest permissible value of this ratio. In this case,

$$A = .730R ,$$

which shows that A and R are of the same order of magnitude. This equivalence to a sphere will be used in the solution to the general problem of flow past an array of rings.

SECTION C: INTERACTION AMONG RINGS

When two or more rings are placed in a flow field, the drag on each is generally different from that on a corresponding isolated ring. Since a second ring disturbs the surrounding flow field, the primary ring is no longer immersed in a uniform flow. It is instead immersed in a modified flow field, and therefore the drag on it is changed accordingly.

In order to obtain the exact interaction among rings, a complete study must be done where rings are randomly distributed in a flow. Each ring is characterized by a distribution of singularities along its centerline and a proper summation of the flow fields associated with each distribution is needed to obtain the complete, exact solution. These calculations are extremely involved, however, and lie beyond the scope of this model, which is concerned with a first approximation to the permeability of an actual porous fibrous medium.

To obtain this approximation, some considerations on the nature of the problem must be made. In an infinite medium of randomly oriented rings, the force on any given ring will be uniformly modified by the influence of neighbouring ones. That is to say, the change in the Stokeslet strengths of a given ring can be taken to be independent of position on the centerline. This, of course, is not strictly true since the modification to the flow field surrounding a ring depends on the actual orientation of neighbouring rings. For example, in places where the distance between the bodies of two nearby rings is small, the interaction must be larger than in other places along the centerline where this distance is greater. On average, however, it is quite reasonable to assume that the interactions are the same throughout the medium provided the distribution of rings is uniform.

At low Reynolds numbers, the interaction between a ring and all its neighbours is a linear combination of the interaction between two rings. This is possible since each ring added to the medium modifies the drag on the initial ring in the same fashion due to the linearity of the Stokes equation. The change in drag when a second ring is added next to the first gives the functional form of the interaction term which can be used to obtain the influence of many rings. A prototype of the interaction problem is treated in the following subsection.

i) TWO COAXIAL RINGS NORMAL TO THE FLOW

It was noted that the interaction sought should remain independent of location along the centerline, or in the notation of section B, the interaction term should not depend on θ_0 (Figure 9). If s_2 is an arbitrary point on the centerline of the second ring, as shown in Figure 9, then the shortest possible distance between s_2 and s_0 (defined in section B) should be independent of θ_0, since interaction is directly related to the closest point of the nearby ring. This condition is obtained by studying two coaxial rings. Here, the flow is chosen to be normal to both rings to simplify calculations; however, this choice does not affect the mathematical properties of the solution.

When the rings are placed in a different fashion, say the second ring of Figure 9 becomes aligned with the flow rather than normal to it, the interaction between them is no longer independent of θ_0. In this case, the flow field associated with singularities on the centerline of the added ring is not symmetric about the x-axis, and therefore it does not have the same influence on all points of the ring's centerline. This means that the local drag varies along each ring's centerline and depends on the orientation of neighbouring rings as well as its own orientation. Such non-uniformities in local drag, however, should not affect the drag on a global scale. By leaving orientation-dependent constants undetermined, the coaxial ring problem, then, seems to be a reasonable way to obtain the functional relationship of the average interaction between two rings.

A second ring of the same size, then, is placed parallel to the first as shown in Figure 9. These rings are both facing a uniform flow which is parallel to the x-axis. The streamlines are symmetric about a plane midway between both rings due to the absence of inertia at low Reynolds numbers, and therefore the drag on each ring is the same. In the following analysis, the drag on the original ring is calculated and compared to the drag on a single ring, thereby revealing the influence due to the second ring.

As shown in Figure 9, the second ring is centered at x=D so that a point s_2 on its centerline is given by the coordinates

$$\begin{bmatrix} D \\ R\ \cos\theta_2 \\ R\ \sin\theta_2 \end{bmatrix}$$

where the angle θ_2 is measured counterclockwise from the x-y plane, and D is the distance between the two rings.

Since the problem is symmetrical and the drags are identical, the singularity distribution associated with both rings is the same. The Stokeslet strength distribution of each ring is of the form

$$\bar{f} = -\gamma T\bar{U} \tag{56}$$

as it was for the single ring normal to the flow. However, the proportionality constants γ and T can no longer be expected to be given be equations 43 and 44 for they are now affected by the second ring. These constants depend on the neighbouring flow pattern and, as before, result from the no-slip boundary condition on the ring surfaces. Again, this condition is satisfied at an arbitrary cross-section of the first ring, given by the point $s_0=s_1(\theta_0)$ where s_0 and s_1 were defined in section B. Equation 13, used to satisfy this condition, was given in section A as

$$\bar{U} + \frac{f_n(S_0)}{4\pi\mu} + \frac{1}{8\pi\mu}\int_{r>r_0}\left(\frac{\bar{f}(s)}{r} + \frac{(\bar{f}(s).\bar{r})\bar{r}}{r^3}\right) ds = 0.$$

However, the contour integral must now span both rings, since both contain singularities. The integration around the first ring was performed in section B and is given by

$$\frac{-T\gamma\bar{U}}{8\pi\mu} I_a$$

where I_a is given by equation 24. Equation 13 now becomes

$$\bar{U} - \frac{T\gamma\bar{U}}{4\pi\mu} - \frac{T\gamma\bar{U}}{8\pi\mu} I_a + \frac{1}{8\pi\mu}\int_{S_2} \left(\frac{\bar{f}}{r_2} + \frac{(\bar{f}.\bar{r}_2)\bar{r}_2}{r_2^3}\right) ds_2 = 0 \qquad (57)$$

where $\bar{r}_2$ is a vector joining the point s_2 to s_0, and S_2 is the contour of the second ring. Here, since the rings are normal to the flow, the fact that $\bar{f}_n = \bar{f}$ was used. The vector $\bar{r}_2$ is

$$\bar{r}_2 = \begin{bmatrix} -D \\ R(\cos\theta_0 - \cos\theta_2) \\ R(\sin\theta_0 - \sin\theta_2) \end{bmatrix}$$

and its magnitude is

$$r_2^2 = D^2 + 2R^2 - 2R\cos\xi \qquad \text{where } \xi = \theta_2 - \theta_0.$$

The only terms of equation 57 which have to be determined come from the contour integral around the second ring. Let this integral be denoted by $\bar{H}$:

$$\bar{H} = \int_{S_2} \left(\frac{\bar{f}}{r_2} + \frac{(\bar{f}.\bar{r}_2)\bar{r}_2}{r_2^3}\right) ds_2$$

To determine $\bar{H}$, the vector $\bar{f}$ must be expressed in terms of the constants γ and T. $\bar{f}$ is proportional to the velocity

$$\bar{U} = U \begin{bmatrix} 1 \\ 0 \\ 0 \end{bmatrix} ,$$

and therefore is

$$\bar{f} = -\gamma T U \begin{bmatrix} 1 \\ 0 \\ 0 \end{bmatrix} .$$

The vector dot product which appears in $\bar{H}$ is then

$$\bar{f} . \bar{r}_2 = DT\gamma U.$$

The integral $\bar{H}$ can now be expressed as

$$\bar{H} = -T\gamma\bar{U}\ I_d + DT\gamma U\ \bar{H}_a$$

where $I_d = \int_{S_2} \frac{ds_2}{r_2}$ and $\bar{H}_a = \int_{S_2} \frac{\bar{r}_2}{r_2^3} ds_2 .$

The y and z components of the quantity $\bar{H}_a$ are zero. This is due to the form of the vector $\bar{r}_2$ in the integral; that is, because the y and z components of this vecter are trigometric expressions, integration over a whole period is zero. The integral $\bar{H}_a$ is then written

$$\bar{H}_a = DI_e \begin{bmatrix} 1 \\ 0 \\ 0 \end{bmatrix}$$

with $I_e = \int_{S_2} \frac{ds_2}{r_2^3} .$

The integrals I_e and I_d are integrated in appendix B and are given by:

$$I_d = 2\sqrt{m'}\ K(m')$$

and

$$I_e = 2\frac{\sqrt{m'}}{D^2}E(m')$$

where

$$m' = \frac{1}{\frac{D^2}{4R^2} + 1}$$

and K(m') and E(m') are elliptic integrals of the first and second kind respectively. These functions are well characterized. Their values are tabulated and graphed in special function handbooks such as the one compiled by Abramowitz and Stegun (29). Furthermore, approximations in terms of logarithms, polynomials and expansions for small m' are available in this text. In terms of these integral functions,

$$\bar{H} = -2T\gamma\bar{U}\sqrt{m'}(K(m') + E(m')),$$

which is substituted into equation 57 to yield:

$$\bar{U} - \frac{T\gamma\bar{U}}{4\pi\mu} - \frac{T\gamma\bar{U}}{4\pi\mu}\left(\ln\frac{8R}{a} - \frac{1}{2}\right) - \frac{T\gamma\bar{U}}{4\pi\mu}\sqrt{m'}\,(K(m') + E(m')) = 0 \qquad (58)$$

This equation is solved for γT to give

$$\gamma T = \frac{4\pi\mu}{\frac{8R}{a} + \frac{1}{2} + J_1} \qquad (59)$$

where $J_1 = \sqrt{m'}(K(m') + E(m'))$

Hence the force per unit length on each ring is given by

$$\bar{f} = \frac{-4\pi\mu\bar{U}}{\ln\frac{8R}{a} + \frac{1}{2} + J_1} \tag{60}$$

The drag on the first ring, denoted by F_3, is obtained by integrating $-\bar{f}$ around a ring; it is easily found to be:

$$\bar{F}_3 = \frac{8\pi^2\bar{U}R\mu}{\ln\frac{8R}{a} + \frac{1}{2} + J_1} \tag{61}$$

The interaction appears as an addition of the term J_1, in the denominator to the single ring solution. The neglected terms in $\bar{F}_3$ are those of $\bar{F}_1$ and those of the correction term calculation. According to slender body theory, the neglected term in the correction term is of order of the thickness radius a divided by the smallest centerline separation distance. In this case, the neglected term is of order $\frac{a}{D}$.

ii) THE AVERAGE INTERACTION BETWEEN TWO RINGS

At this point, it is necessary to make assumptions as to the nature of the average interaction between two rings, because it is the average which appears in the general solution. Since the average spacing between the centerlines of two rings is D, one should expect an interaction term similar to the parallel ring case, where the separation is exactly D everywhere.

Mathematically, the interaction term comes from the integral $\bar{H}$ which depends on the exact two-body configuration. It must be pointed out that for a general two-body problem, $\bar{H}$ is expected to be a function of θ_0 because of the non-constant spacing between various sections of the two rings. It is impractical to integrate $\bar{H}$ for each configuration and take the average because of the difficulty of calculations involved. However, the solution to $\bar{H}$ must include complete elliptic integrals which come from the form of the integrals to be calculated, namely from

$$\int_0^{2\pi} \frac{\cos^n\theta}{r_2^p}\, d\theta$$

and

$$\int_0^{2\pi} \frac{\sin^n\theta}{r_2^p}\, d\theta ,$$

where $p = 1,3$ and $n = 0,1,2,3$. Since the magnitude of $\bar{r}_2$ is of the form

$$r_2 = \sqrt{a + b\cos\theta + c\sin\theta},$$

these integrals can be reduced to complete elliptic integrals by performing changes in variables similar to the one appearing in Appendix B. The exact magnitude of these integrals must, however, remain undetermined because their coefficients are unknown.

Based on these arguments, it is reasonable to assume that the average interaction term, J , is of the form:

$$\langle J \rangle = \sqrt{m}\ (\Delta' K + \eta' E) \tag{62}$$

with

$$m = \frac{1}{(\frac{D}{nR})^2 + 1} \tag{63}$$

where Δ', η' and n are constants to be determined. Since m comes at least in part from the coefficients appearing in the vector $\bar{r}_2$, the constant n appearing in the argument of m assures that no particular form of $\bar{r}_2$ is taken.

iii) CUBICAL ARRAY OF RANDOMLY ORIENTED RINGS

At low Reynolds numbers, the influence of many neighbouring rings on a given one is simply a linear combination of two-ring problems. If $\bar{H}_i$ is the integral giving the influence of the i^{th} ring on the initial one, then

$$\bar{H} = \sum_{i=1}^{N} \bar{H}_i$$

where N is the number of rings considered. The interaction term J, then, is also a linear combination of the average two-body interaction terms, or

$$J = \sqrt{m}(\Delta K + \eta E) \tag{64}$$

where Δ and η are the sum of Δ''s and η''s respectively.

In a regular array of randomly oriented rings, the force per ring is the average force $\langle \bar{F} \rangle$ (equation 52) modified to account for the presence of surrounding rings. As in equation 61, this modification must appear as an addition of an interaction term to the denominator of the single ring solution. It is noted that this is a modification to the second order term. The average force per ring in the array is then written:

$$\bar{F} = \frac{\frac{20}{3}\pi^2 \mu \bar{U} R}{G+J} \tag{65}$$

The undetermined constants, n, η and Δ appearing in J (equation 64), are now found by considering two limiting cases. The first of these is when the rings are far apart and the second is when the radius of curvature approaches infinity.

When the rings are sufficiently separate, they can be replaced by spheres having the same drag. This condition applies when the ratio $\frac{D}{R}$ is large, the other ratio $\frac{a}{R}$ remaining small to comply with slender body theory. The radius of the equivalent sphere is given by equation 55 because the system is dilute and each body is effectively alone. This equation is substituted into equation 65 to give the drag on a sphere in a cubical array:

$$\bar{F} = \frac{6\pi\mu\bar{U}A}{1 + \frac{J}{G}} \tag{66}$$

It must be remembered that this result is valid only for large values of $\frac{D}{R}$, or small values of m. In this case, the elliptic integrals found in J are given as the following asymptotic expressions:

$$K(m) = \frac{\pi}{2}(1 + \frac{m}{4} + 0(m^2)),$$

$$E(m) = \frac{\pi}{2}(1 - \frac{m}{4} + 0(m^2)),$$

and m, for large $\frac{D}{R}$, is

$$m = (\frac{nR}{D})^2 (1 - (\frac{nR}{D})^2 + 0(\frac{R^4}{D^4}))$$

These relations are used to express J (given by equation 64) as an asymptotic expansion in powers of $\frac{R}{D}$,

$$J = n(\Delta+\eta)\frac{\pi}{2}\frac{R}{D} - n^3(\Delta+3\eta)\frac{\pi}{8}\frac{R^3}{D^3} + 0(\frac{R^4}{D^4}). \tag{67}$$

Equations 66 and 67 are then combined to give the drag per sphere in a cubical lattice (at low solid fractions). The exact solution to this problem has been provided by Hasimoto (18). For spheres of radius A, his prediction of the drag is

$$\bar{F}_s = \frac{6\pi\mu\bar{U}A}{Q}$$

with

$$Q = 1 - 1.7601\ c^{1/3} + c + 0(c^2),$$

where c is the volume concentration of spheres; by definition, c is

$$c = \frac{4}{3}\pi\ \frac{A^3}{D^3}\ .$$

Using this definition for c and substituting the equivalent radius (equation 55), the quantity Q becomes:

$$Q = 1 - \frac{P}{G}\ R/D + \frac{P_1}{G^3}\ (R/D)^3 \tag{68}$$

where $P = 9.9039$ and $P_1 = 178.2$.

By equating $\bar{F}$ and $\bar{F}_s$, which are now both solutions for an array of spheres, a relationship between Q and J is obtained:

$$1 + \frac{J}{G} = Q\ .$$

The substitution of equations 67 and 68 into this equation gives

$$1 + \frac{n(\Delta+\eta)}{G}\,\frac{\pi}{2}\,(R/D) - \frac{n^3(\Delta+3\eta)}{G}\,\frac{\pi}{8}\,(R/D)^3$$
$$= 1 - \frac{P}{G}\,(R/D) + \frac{P_1}{G^3}\,(R/D)^3$$

or, by neglecting terms in G^{-3} which are of order $\ln^{-3}\frac{8R}{a}$,

$$\left(n(\Delta+\eta)\,\frac{\pi}{2} + P\right)\frac{R}{D} - \left(n^3(\Delta+3\eta)\,\frac{\pi}{8}\right)\frac{R^3}{D^3} = 0$$

This equation must be valid independently of the ratio $\frac{R}{D}$ so that

$$n(\Delta+\eta)\frac{\pi}{2} + P = 0 \tag{69}$$

and

$$n^3(\Delta+3\eta)\frac{\pi}{8} = 0 \tag{70}$$

Since n cannot be zero, equation 70 becomes

$$\Delta = -3\eta \tag{71}$$

and by substitution of this relation into equation 69, the following relationship between n and Δ is obtained:

$$\eta\Delta = \frac{-3P}{\pi} \tag{72}$$

This equation is indeterminate since it possesses two unknowns. A second equation is necessary. This equation comes from a hypothesis based on the behaviour of the solution when the radius of curvature goes to infinity.

When the ring radius becomes large compared with the separation distance D, rings entwine or overlap to form an entangled medium (Figure 5(i)). This, however, does not violate any hypothesis used in the construction of the lattice provided that the body-to-body distance between any two rings exceeds 10a. This last restriction comes from slender body theory which states that the correction term is of order of the thickness radius a divided by the smallest centerline separation distance.

As R approaches infinity, the medium becomes a three dimensional random array of straight rods, definite in length. Two existing solutions for three dimensional rod arrays by Spielman and Goren and Jackson and James (9) show that in such a case, the permeability on the medium is only a function of the volume concentration of rods. Thus, if $\emptyset$ is the space occupied by the rings per unit volume, then the permeability of the ring medium should depend on $\emptyset$ only for a large enough value of $\frac{R}{D}$.

The permeability given by Darcy's law introduced in Chapter I is

$$k = \frac{\mu U}{\Delta P/\Delta x}$$

For a ring in an array, the pressure drop $\frac{\Delta P}{\Delta x}$ is simply the drag per unit volume on a ring; hence

$$k = \frac{D^2 \mu U}{F} \qquad (73)$$

where F is the magnitude of $\bar{F}$ given by equation 65. For a ring array, the solid volume fraction is

$$\emptyset = \frac{2\pi^2 a^2 R}{D^3} \qquad (74)$$

so that equation 73 becomes

$$k = \frac{2\pi^2 a^2 R \mu U}{\emptyset F} \qquad (75)$$

The substitution of equation 65 into this expression gives the permeability of the ring solution in terms of $\mathrm{In}\frac{R}{a}$ and $\frac{R}{D}$ as:

$$\frac{k}{a^2} = \frac{3}{10}\frac{1}{\phi}\left(\ln\frac{8R}{a} + \frac{2}{5} + \sqrt{m}\,(\Delta K + \eta E\right) \qquad (76)$$

by using the values of J and G given by equations 64 and 53 respectively. It will be recalled that m (equation 63) is

$$m = \left[\left(\frac{D}{nR}\right)^2 + 1\right]^{-1}$$

This function can be expanded in powers of $\frac{D}{R}$ (R approaches infinity) to give

$$m = 1 - \left(\frac{D}{nR}\right)^2 + 0\left(\frac{D^4}{R^4}\right) \qquad (77)$$

For values of m close to 1, the elliptic integrals K and E can be approximated as follows:

$$K(m) = \ln 4 + \frac{1}{2}\,\mathrm{In}\left(\frac{1}{1-m}\right)$$

and

$$E(m) = 1$$

Substitution of the expansion for m (equation 77) into equation 78 is used to obtain

$$K = \ln 4n + \ln\frac{R}{D}$$

This value of K is used in conjunction with the approximations for m and E to give the permeability of the ring system,

$$\frac{k}{a^2} = \frac{3}{10}\,\frac{1}{\phi}\,\left(\ln\frac{8R}{a} + \frac{2}{5} + \Delta\ln 4n + \Delta\ln\frac{R}{D} + \eta\right)$$

which can be expressed in terms of ϕ as

$$\frac{k}{a^2} = \frac{3}{20}\,\frac{1}{\phi}\,\left[\ln\frac{1}{\phi} + 7.94149 + (3+2\Delta)\ln\frac{R}{D} + 2\Delta\ln 4n + 2\eta\right] \qquad (78)$$

Since the permeability must be independent of $\frac{R}{D}$ for large values of this ratio, the coefficient of $\ln\frac{R}{D}$ must be zero, hence

$$\Delta = \frac{-3}{2} \qquad (79)$$

The values of η and n given by equations 71 and 72 can now be found explicitly:

$$\eta = \frac{1}{2} \qquad (80)$$

and

$$n = \frac{2P}{\pi}$$

By using the value 9.9039 for P (from Hasimoto's solution), n becomes

$$n = 6.305 \qquad (81)$$

Hence all the terms for the equation predicting the permeability of a ring array are known. The final equation is

$$\frac{k}{a^2} = \frac{3}{20}\,\frac{1}{\phi}\left(\ln\frac{1}{\phi} - \Omega\left(\frac{R}{D}\right) + \varepsilon\right) \qquad (82)$$

where

$$\Omega\left(\frac{R}{D}\right) = -7.94149 + 3\ln\frac{D}{R} - \sqrt{m}\,(3K(m) - E(m)) \qquad (83)$$

and

$$m = \frac{1}{\left(\frac{D}{6.305R}\right)^2 + 1} \qquad (84)$$

K and E are complete elliptic integrals of the first and second kind respectively and the solid fraction ϕ is given by equation 74. The greatest neglected term, ε, in this solution comes from two sources. The first source is the force on an isolated ring. The neglected term in this solution was of order $\ln^{-3}\left(\frac{8R}{a}\right)$; however, when this solution is written as the permeability of non-interacting rings, the neglected term becomes of order $[\emptyset \ln(\frac{8R}{a})]^{-1}$. In this case, then, ε is of order $\ln^{-1}(\frac{8R}{a})$. The second contribution to ε comes from the interaction term J which is of order $\frac{a}{d}$ where d is the smallest centerline-to-centerline distance between rings.

When $\frac{R}{D}$ is small, d is close to D due to the vast separation distance between rings. In this case, the neglected term comes from the non-interacting ring solution. When $\frac{R}{D}$ is large, however, d is no longer of order D and the contribution to ε from J becomes important. In this case, the medium resembles a medium of straight rods where

$$\emptyset \sim \frac{\pi a^2}{d^2}$$

and therefore the neglected term ε now becomes of order $\sqrt{\emptyset}$.

CHAPTER IV

PRESENTATION OF RESULTS AND CONCLUSION

i) PRESENTATION OF RESULTS

Values of $\frac{k}{a^2}$, calculated from equation 82 for various values of $\frac{R}{D}$ and ϕ, are given here along with comparisons to previous theoretical and experimental results. Since the permeability given be equation 82 depends on two independent variables, two sets of graphs are plotted. The variation of the radius of curvature for fixed solid fractions gives plots of $\frac{k}{a^2}$ versus $\frac{R}{D}$ which cannot be compared to other theories since none exist. Other theories (Spielman and Goren, Jackson and James) can be compared to plots of $\frac{k}{a^2}$ versus ϕ for fixed radii of curvature.

The analytical expression for $\frac{k}{a^2}$ when $\frac{R}{D}$ is varied but ϕ is constant is a complicated function involving elliptical integrals. Because Ω is the only parameter which varies with $\frac{R}{D}$, it is useful to tabulate it. This table is presented in Figure 10 where the numerical values of Ω are given to three significant digits. These values of Ω have been used for plots of $\frac{k}{a^2}$ versus $\frac{R}{D}$ shown on Figures 11, 12 and 13 for ϕ=.01, ϕ=.001 and ϕ=.0001 respectively. The limit of the theory is arbitrarily taken to be when $\frac{a}{R}$ reaches 0.1, since the neglected terms at this point become large enough to produce an uncertainty of order 10% on the result. For the larger values of ϕ, small values of $\frac{R}{D}$ lie outside this domain. This does not violate assumptions made in the analysis since the small $\frac{R}{D}$ expansion which was used served only to match undetermined parameters in the general solution. At very small ϕ, this expansion is valid. However, since is independent of ϕ, it remains valid for all solid fractions.

The plots of $\frac{k}{a^2}$ versus $\frac{R}{D}$ have a semi-log scale since the permeability changes little with $\frac{R}{D}$. The sudden drop in permeability observed for small values of $\frac{R}{D}$ is not thought to appear in fibrous porous media flow. However, in this case, the more appropriate scale to express the permeability in non-dimensional form becomes R, since it is of the same order of magnitude as the radius A of the equivalent sphere. To illustrate this, the permeability can be written

$$\frac{k}{R^2} = \frac{3}{40\pi^2} \frac{D^3}{R^3} (\ln\frac{1}{\emptyset} - \Omega).$$

In this form the permeability increases rapidly as $\frac{R}{D}$ decreases, as expected. When the rings are this far apart, it is no longer clear what this model physically represents. This model, then, is most useful in the region where $\frac{R}{D}$ is above $\frac{1}{3}$ to $\frac{1}{2}$; here it can be used to represent a continuous skein because non-dimensionalization of permeability by the strand radius makes sense. This is the region where different theories should be compared.

The value of $\frac{k}{a^2}$ predicted by prior investigations is compared to the present work in the table of Figure 14. The equations of Davies, Spielman and Goren, and Jackson and James were introduced in Chapter I. Davies' equation is an empirical relation obtained from a correlation of experimental data while both Spielman and Goren and Jackson and James present theoretical results based on three dimensional arrays of straight rods. Their results are given by equations 3, 4 and 5 respectively in Chapter I. The two "present work" columns give the permeability predicted by equation 82 where the value of Ω is determined by the table of Figure 10 for two values of $\frac{R}{D}$. Since for large values of $\frac{R}{D}$ the permeability depends only on solid fraction, this case is important. Furthermore, it permits direct comparison with straight rod theories. The permeability in this case is given by

$$\frac{k}{a^2} = \frac{3}{20}\frac{1}{\emptyset}\left[\ln\frac{1}{\emptyset} - .742 + 0(\emptyset^{\frac{1}{2}})\right] \tag{85}$$

which was used to obtain the values of the "$\frac{R}{D} \longrightarrow \infty$" column. The second "present work" column was given for the smallest value of $\frac{R}{D}$ where $\frac{k}{a^2}$ remains meaningful. This value is estimated at $\frac{R}{D} = .3$. In this case, the value of Ω given by Figure 10 gives the permeability as

$$\frac{k}{a^2} = \frac{3}{20}\frac{1}{\emptyset}\left[\ln\frac{1}{\emptyset} - .497\right] \tag{86}$$

valid only for thin rings as defined previously. The results from the first four columns are also presented in graphical form in Figure 15. The graph is rather crowded with four curves very close to each other, and should only be regarded as an illustration of the previous table (Figure 14). It is observed from these figures that the results from the present theory lie between the two straight rod theories previously established. This is true regardless of the $\frac{R}{D}$ value selected, provided this ratio remains in the meaningful range.

The effect of the ratio $\frac{R}{D}$ is summarized in Figures 16 and 17. The noted increase in permeability at constant solid fraction as $\frac{R}{D}$ decreases could be attributed, at least in part, to the increase in surface area exposed to the flow. In low Reynolds number situations, viscous forces are the only ones accounting for the drag on the ring network. A greater surface area allows the skin friction due to viscous drag to increase. The greater surface area of the large, thin rings could then partly account for an increase in drag over smaller, fatter rings. It follows that the permeability should decrease correspondingly.

For a real porous medium, say a randomly coiled polymer structure in solution, the surface area exposed to the flow of solvent is only a function of the polymer structure and is expected to always be the same at a given solid fraction. That is, each value of ϕ has a single value of $\frac{R}{D}$ associated with it. Furthermore, as the structure is compressed, the coils get tighter as the separation distance decreases so that $\frac{R}{D}$ must vary only a little. This approximation is thought to be realistic for small volume fractions. In such a medium, the permeability given by equation 82 is uniquely determined by the value of the solid fraction.

The most appropriate estimate of $\frac{R}{D}$ must be made from known notions of the configuration of these structures. Since these media are made from very long coiled strands instead of separate rings, the radius of curvature must be of the order of magnitude of the mean separation distance. The ratio $\frac{R}{D}$ must therefore lie between 1/3 and 5 for most fibrous media, such as steel wool. The small differences in permeability in this region prompts the proposal that $\frac{R}{D} = 1$ be the average representative value. In this instance, the permeability becomes

$$\frac{k}{a^2} = \frac{3}{20}\frac{1}{\phi}\left(\ln\frac{1}{\phi} - .679 + 0\left(\ln^{-1}\left(\frac{1}{\phi}\right)\right)\right) \qquad (87)$$

where the neglected term here comes from the isolated ring calculation $(\ln^{-1}\frac{8R}{a})$; in this case, this term is proportional to $\ln^{-1}\frac{1}{\phi}$, which is larger than the error of the interaction term.

ii) CONCLUSION

The object of this thesis has been to provide a model for the flow through fibrous structures. A distribution of rings was chosen because of its analytical approachability. It is believed that the effect of curvature in random media is adequately represented by such a model. The permeability obtained was found to vary little with values of curvature so that a single such radius could represent most media. Thus a single relation (equation 87) was proposed to describe the permeability of random fibrous porous media. The values obtained using this relation are not much different from those obtained for straight rods, when $\frac{R}{D}$ approaches infinity, and compares favourably with other straight rod theories. This model, however, is believed to be the only one which estimates the influence of curvature on permeability.

A basic shortcoming of this solution is the lack of a rigorous accounting of the influence between rings. This influence was found here as a first order estimate to a two-ring problem solution. This is not an exact solution to the problem of interference between strands, which was the problem encountered by both Spielman and Goren and Jackson and James. A more thorough investigation of this problem should also include touching strands and varying radii of curvature. At the experimental level, the permeability of small volume fraction fibrous media should be investigated to validate the present theoretical work.

REFERENCES

1. Darcy, H., "Les Fortaines Publiques de la Ville de Dijon," Dalmont, Paris, 1856.

2. Carman, P.C., "The Determination of the Specific Surface of Powders - I," Society Chem. Industry (Trans. and Communications), V. 57, p. 225, July 1938.

3. Wiggins, E.J. et al., "Determination of the Specific Surface of Fibrous Materials," Can. J. Research, V. 17, Sec. B, p. 318, 1939.

4. Sullivan, R.R., "Specific Surface Measurements on Compact Bundles of Parallel Fibers," J. of App. Phys., V. 13, p. 725, November 1974.

5. Bergelin, O.P. et al., "Heat Transfer and Fluid Friction During Viscous Flow Across Banks of Tubes - III: A study of tube spacing and tube size," Trans. ASME, p. 881, August 1950.

6. Chen, C.Y., "Filtration of Aerosols by Fibrous Media," Chem. Rev., Vol. 55, p. 595, 1955.

7. Wheat, J.A., "The Air Flow Resistance of Glass Fiber Filter Paper," Can. J. of Chem. Eng., p. 67, April 1963.

8. White, M.L., "The Permeability of an Acrylamide Polymer Gel," J. Phys. Chem., Vol. 64, p. 1563, 1960.

9. Jackson, G.W. and James, D.F., "The Hydrodynamic Resistance of Hyaluronic Acid and Its Contribution to Tissue Permeability," Biorheology, Vol. 19, 1982.

10. Stanzel, K.H. et al., "Optimization of Collagen Dialysis Membranes," Trans. Amer. Soc. Artif. Int. Organs, Vol. XVII, p. 293, 1971.

11. Kostornov, A.G. and Shevchuck, M.S., "Hydraulic Characteristics and Structure of Porous Metal Fiber Materials III. Laws of Liquid Permeability of Materials," Pososhkovaya Metallurgiya, No. 9 (177), p. 450, September 1977.

12. Jackson, G.W. and James, D.F., "Permeability of Fibrous Porous Metals," submitted to A.I. Ch. E. Journal.

13. Davies, C.N., "The Separation of Airborne Dust and Particles," Proc. Inst. Mech. Eng., Vol. 13, p. 185, 1952.

14. Happel, J., "Viscous Flow Relative to Arrays of Cylinders," A.I. Ch. E. Journal, Vol. 5, No. 2, p. 124, 1959.

15. Drummond, J.E. and Tahir, M.I., "Laminar Viscous Flow Through Regular Arrays of Parallel Solid Cylinders," Int. J. Multiphase Flow, in press.

16. Sparrow, E.M. and Loeffler, A.L. Jr., "Longitudinal Laminar Flow Between Cylinders Arranged in Regular Array," A.I. Ch. E. Journal, Vol. 5, No. 3, p. 325, 1959.

17. Kuwabara, S., "The Forces Experienced by Randomly Distributed Parallel Circular Cylinders or Spheres in a Viscous Flow at Small Reynolds Numbers," J. of the Phys. Soc. of Japan, Vol. 14, No. 4, p. 527, April 1959.

18. Hasimoto, H., "On the Periodic Fundamental Solutions of the Stokes Equations and Their Application to Viscous Flow Past a Cubic Array of Spheres," J. Fluid Mech. Vol. 5, p. 317, 1959.

19. Sangani, A.S. and Acrivos, A., "Slow Flow Past Periodic Arrays of Cylinders with Application to Heat Transfer," Int. J. of Multiphase Flow, Vol. 8, No. 3, p. 193, 1982.

20. Cox, R.G., "The Motion of Long Slender Bodies in a Viscous Fluid. Part I. General Theory," J. Fluid Mech., Vol. 44, p. 791, 1970.

21. Tillett, J.P.K., "Axial and Transverse Stokes flow Past Slender Axysymmetric Bodies," J. Fluid. Mech., Vol. 44, p. 401, 1970.

22. Spielman, L. and Goren, S.L., "Model for Predicting Pressure Drop and Filtration Efficiency in Fibrous Media," Environmental Sci. and Tech., Vol. 2, No. 4, p. 279, April 1968.

23. Burgers, J.M., "On the Motion of Small Particles of Elongated Form Suspended in a Viscous Liquid," 2nd Report of Viscosity and Plasticity, Kon. Ned. Akad. Wet., Verhand. (Eerste Sectie), Vol. 16, p. 113, 1938.

24. Batchelor, G.K., "Slender Body Theory for Particles of Arbitrary Cross-Section in Stokes Flow," J. Fluid. Mech., Vol. 44, p. 419, 1970.

25. Lighthill, J., "Flagellar Hydrodynamics," SIAM Review, Vol. 18, No. 2, p. 161, April 1976.

26. Fick, A.A. and Homsy, G.M., "Stokes Flow Through Periodic Arrays of Spheres," J. Fluid. Mech., Vol. 115, p. 13, 1982.

27. Sangani, A.S. and Acrivos, A., "Slow Flow Through a Periodic Array of Spheres," Int. J. Multiphase Flow, Vol. 8, No. 4, p. 343, 1982.

28. Chwang, A.T. and Wu, T.Y.T., "Hydromechanics of Low-Reynolds-Number Flow. Part 2. Singularity Method for Stokes Flows," J. Fluid. Mech., Vol. 67, p. 787, 1975.

29. Abramowitz, M. and Stegun, I.A., "Handbook of Mathematical Functions with Formulas, Graphs and Mathematical Tables," Nat'l Bureau of Stds., App. Math. Series 55, 1964.

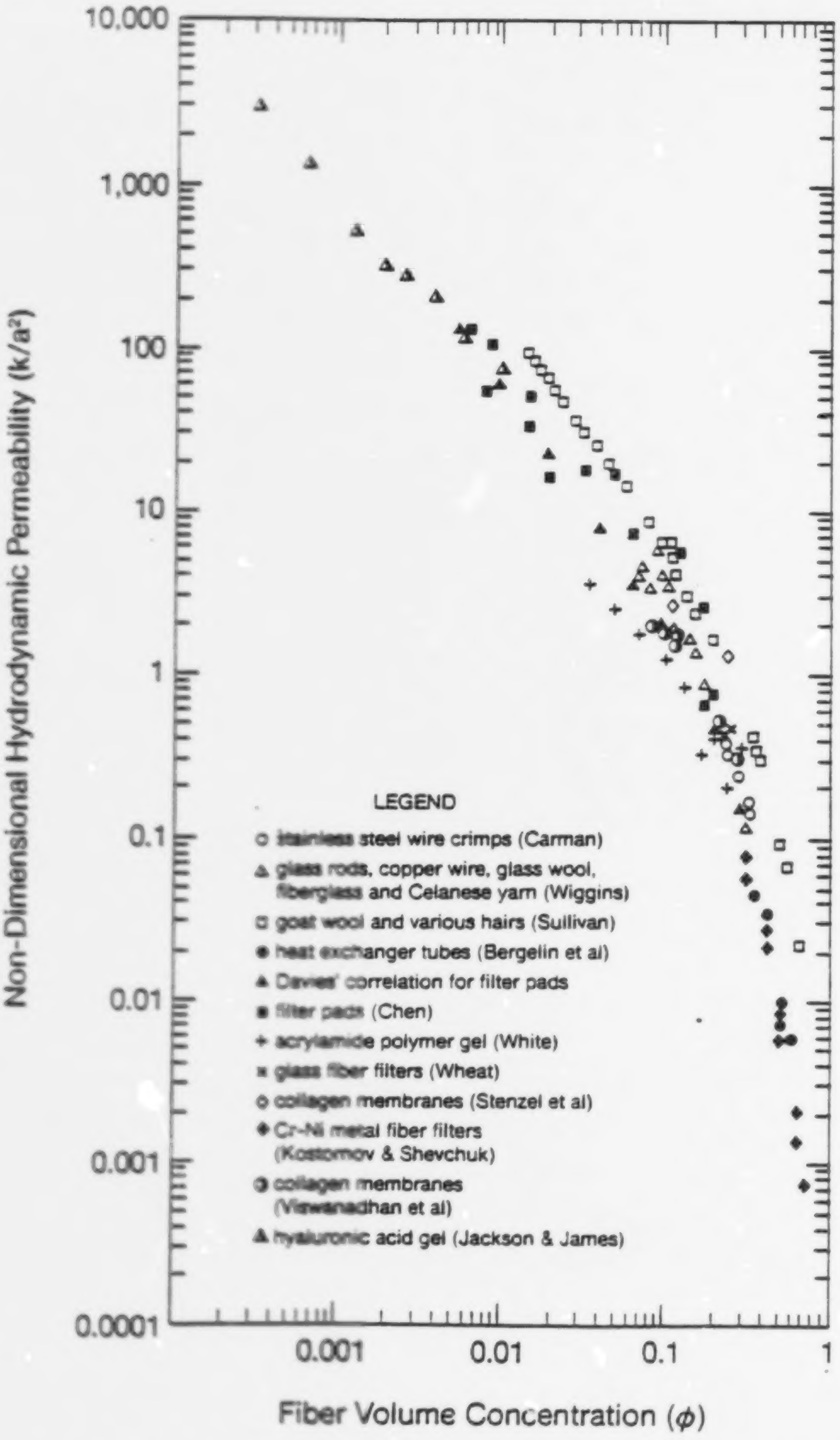

Figure 1. Non-Dimensional Permeability as a Function of Solidity, for Various Fibrous Porous Media from Jackson and James (12)

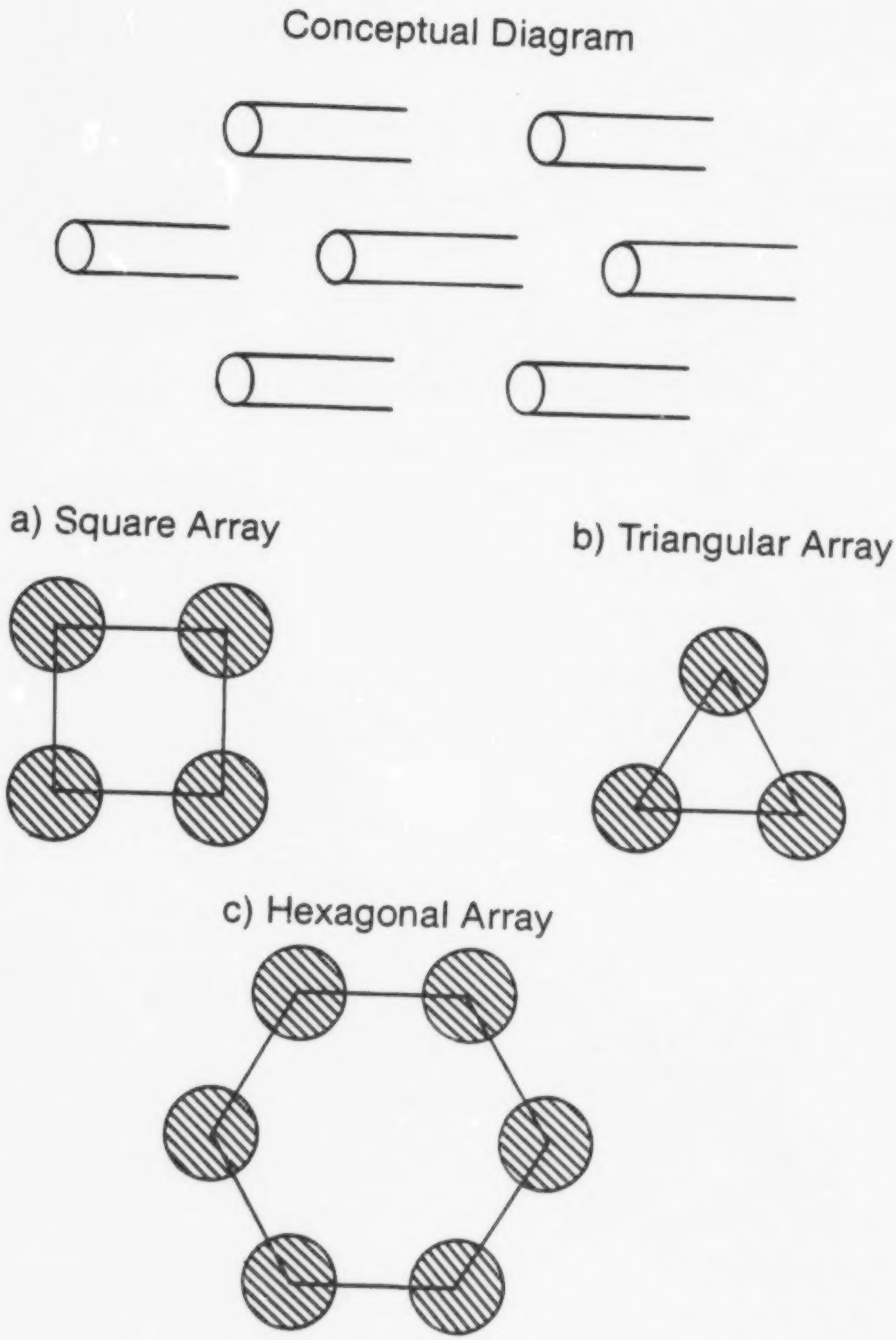
Conceptual Diagram
a) Square Array
b) Triangular Array
c) Hexagonal Array

Figure 2. Parallel Rod Model for Porous Media

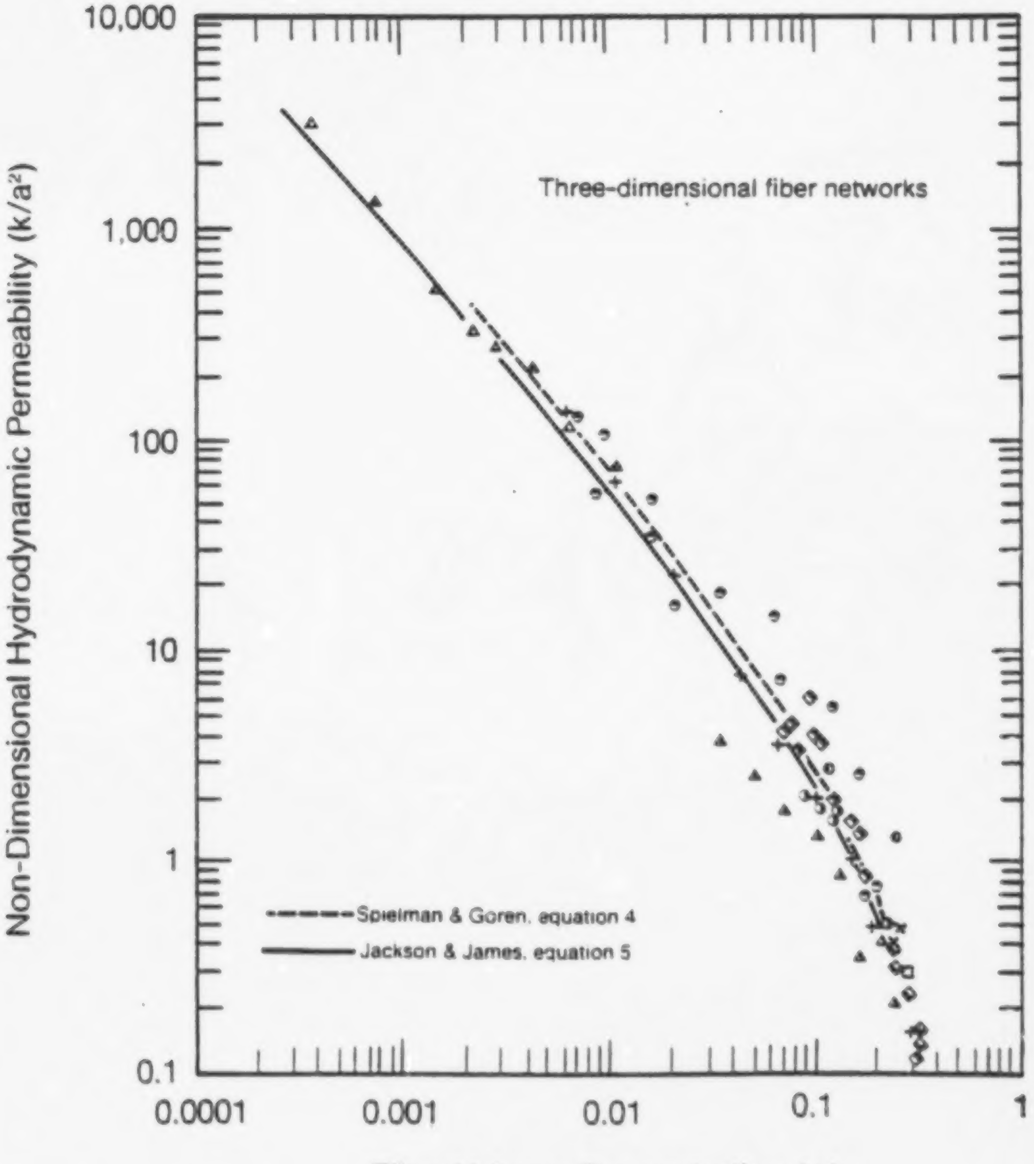

Figure 3. Non-Dimensional Permeability versus Solid Volume Fraction, from Jackson and James (12)

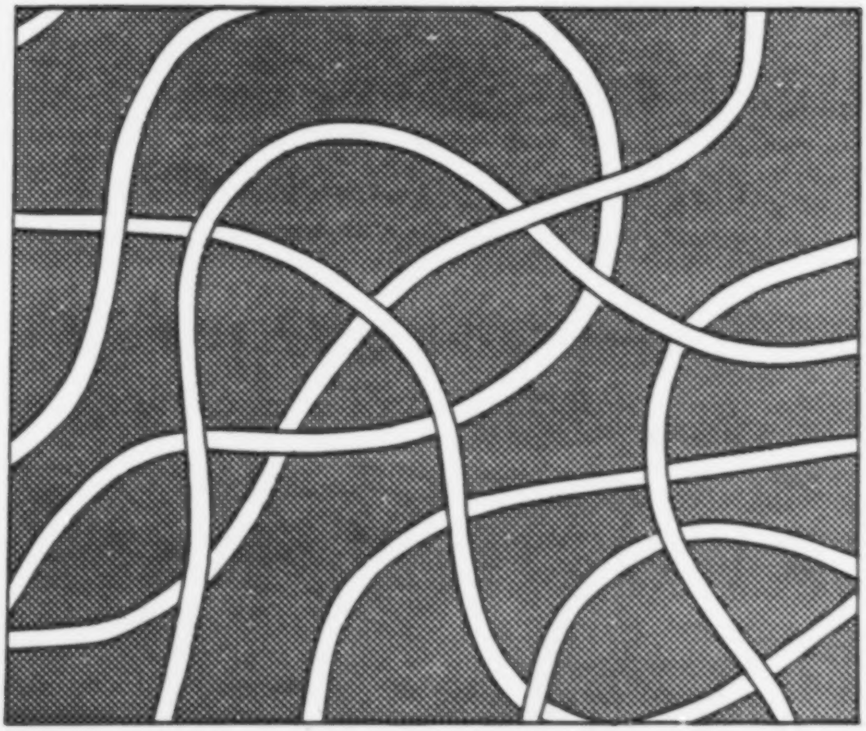

Figure 4. Schematic Representation of a Portion of a Polymer Skein in an Aqueous Solution.

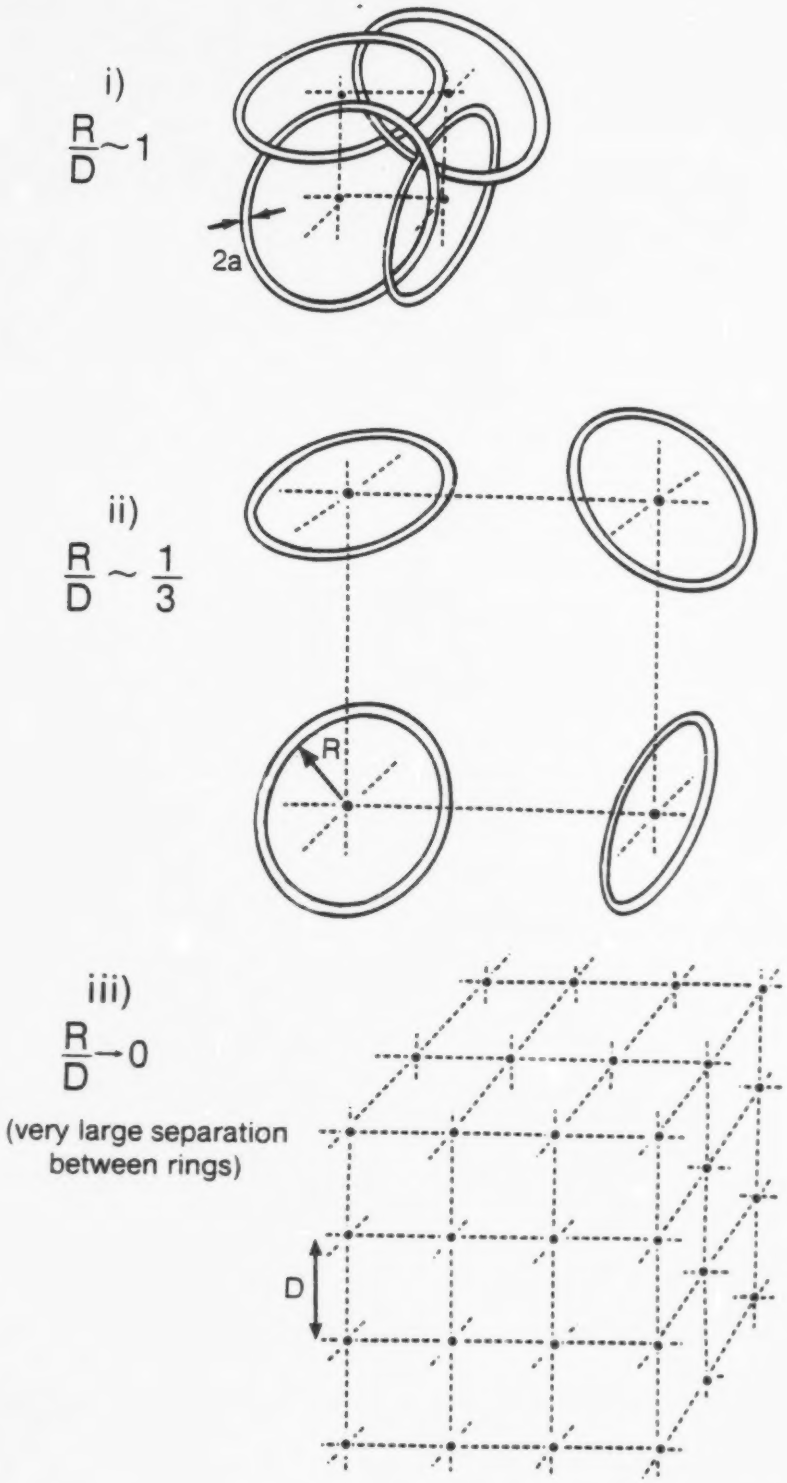
i)
R/D ~ 1
2a
ii)
R/D ~ 1/3
R
iii)
R/D → 0
(very large separation between rings)
D

Figure 5. Conceptual Diagram for Rings in a Cubical Array.

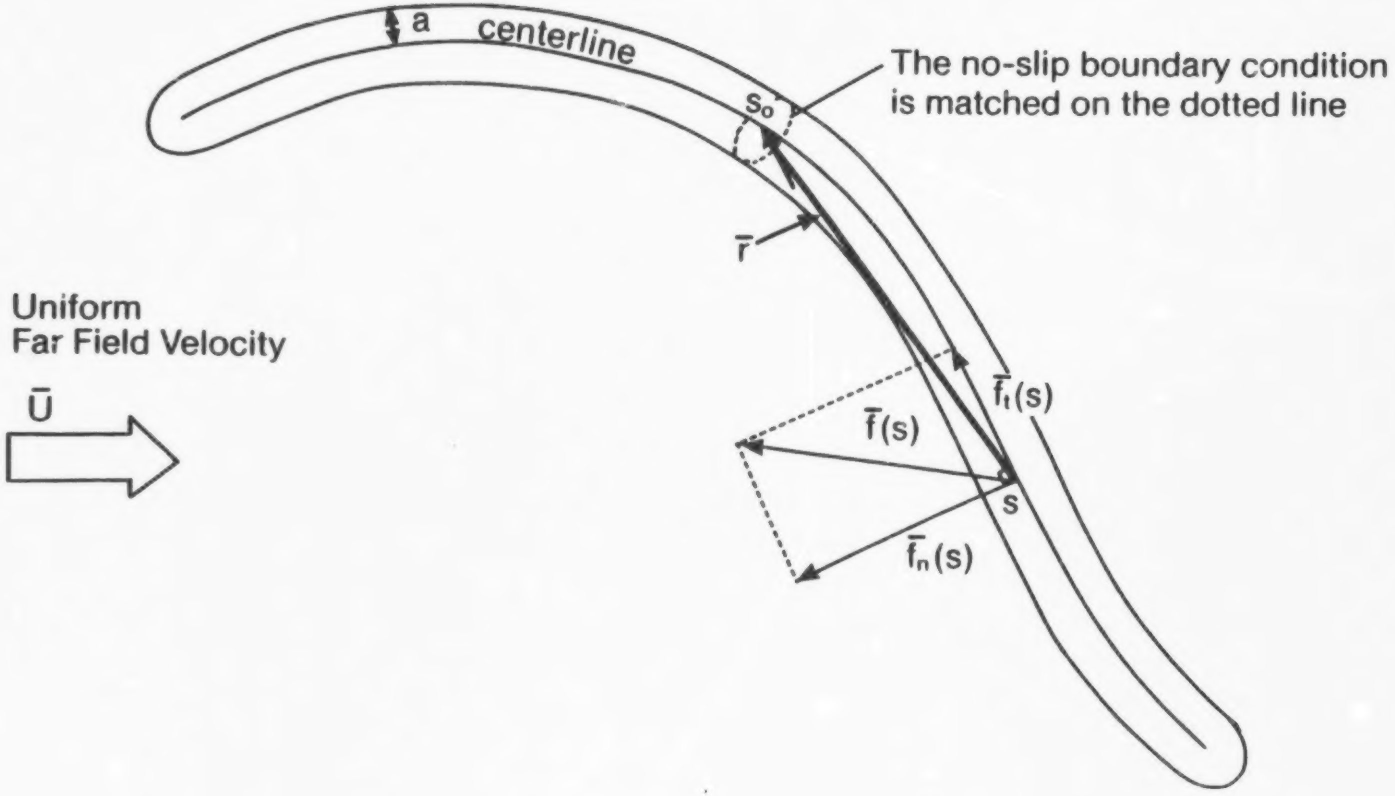
a
centerline
s_o
The no-slip boundary condition
is matched on the dotted line
$\bar{r}$
Uniform
Far Field Velocity
$\bar{U}$
$\bar{f}_t(s)$
$\bar{f}(s)$
s
$\bar{f}_n(s)$

Figure 6. Definition Diagram For Lighthill's Theorem

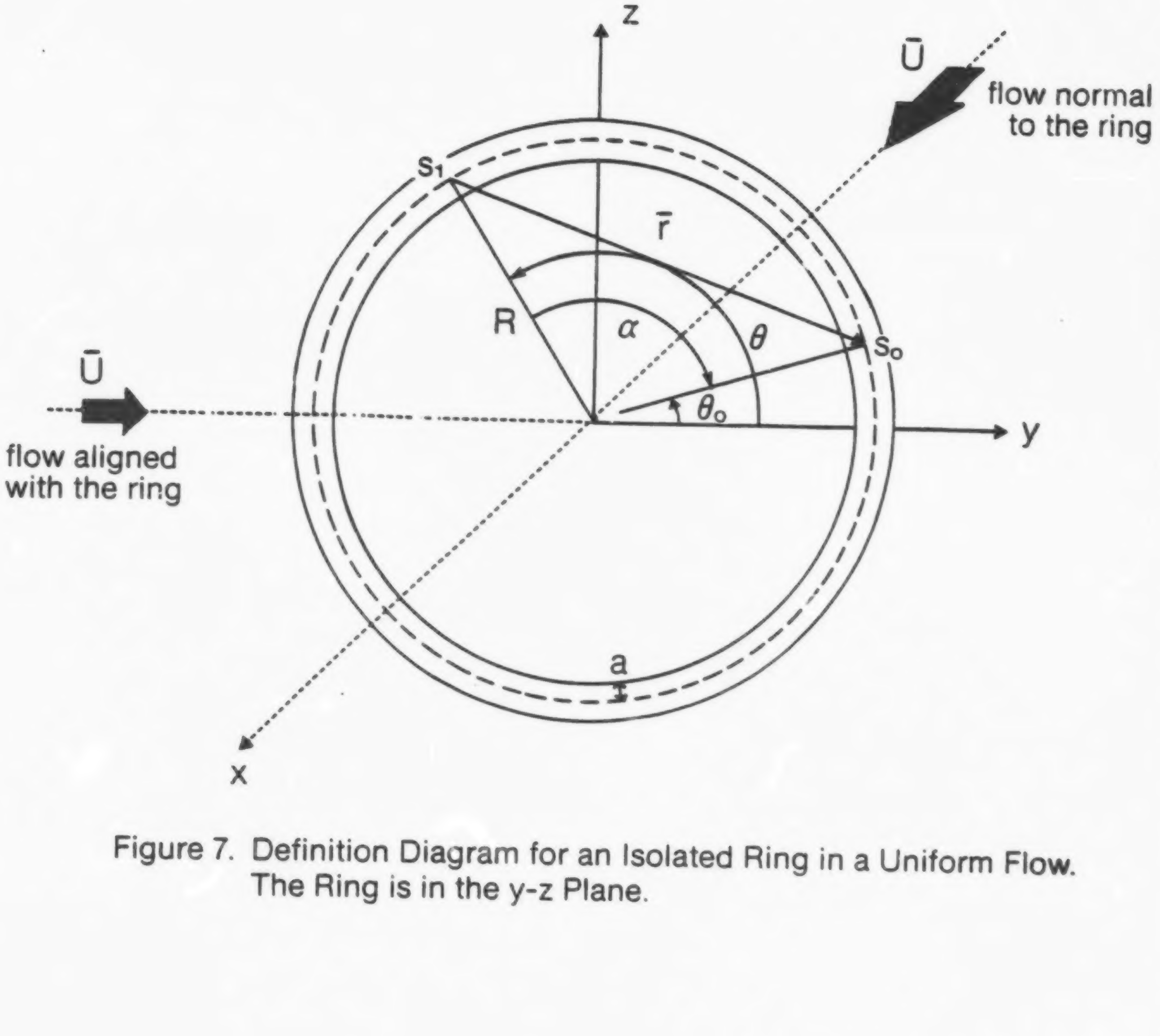
z
Ū
flow normal
to the ring
S₁
r̄
R
α
θ
S₀
Ū
θ₀
y
flow aligned
with the ring
a
x

Figure 7. Definition Diagram for an Isolated Ring in a Uniform Flow. The Ring is in the y-z Plane.

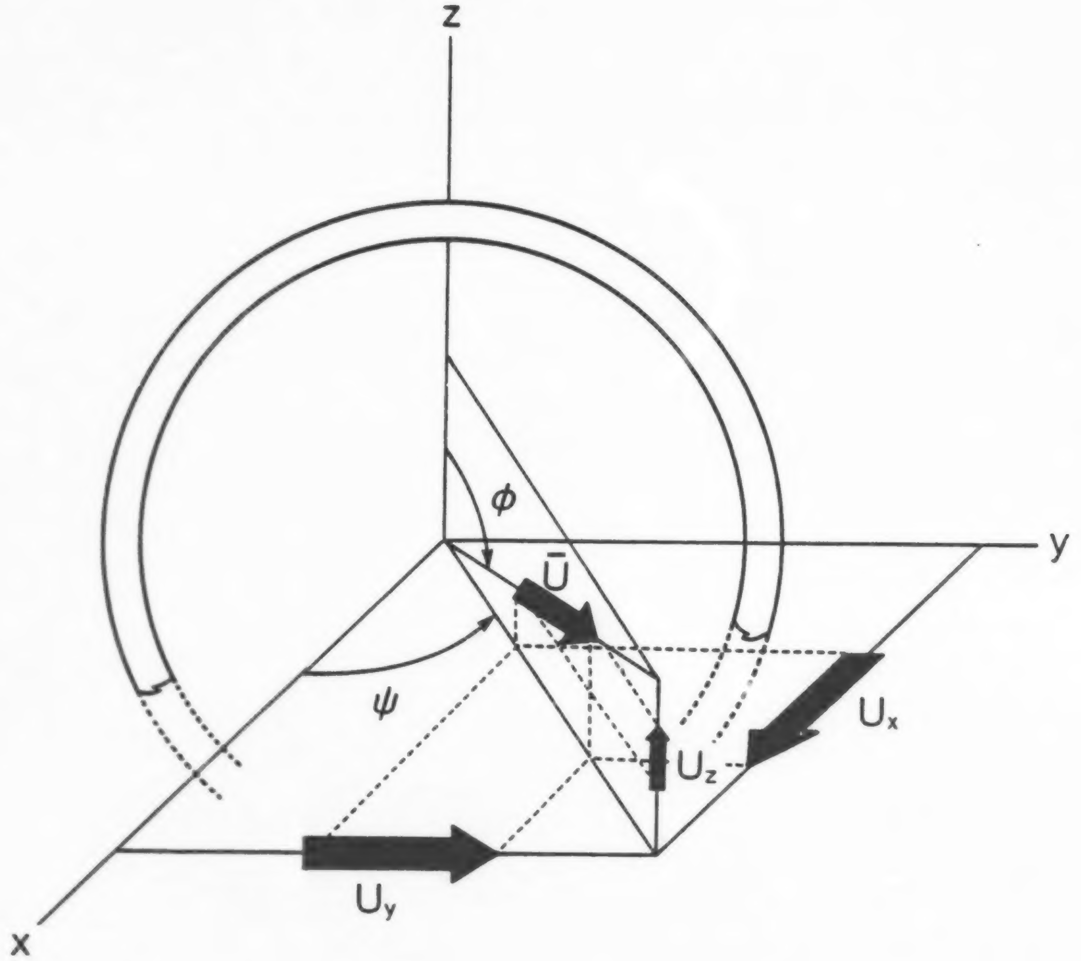
z
ϕ
y
$\bar{U}$
ψ
U_x
U_z
U_y
x

Figure 8. Definition Diagram of Flow-Related Parameters.
The Ring is in the y-z Plane.

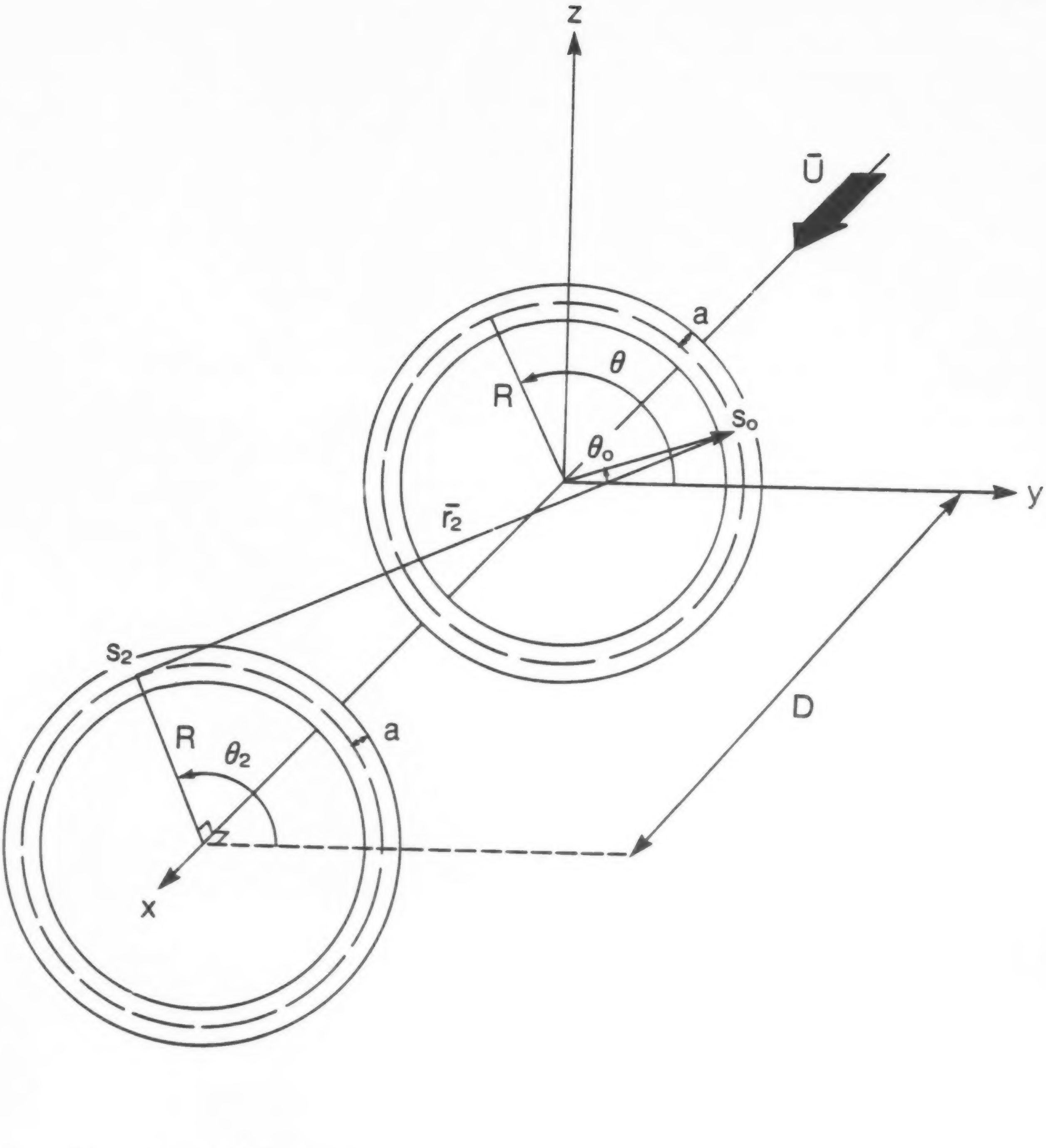
z
Ū
a
θ
R
s₀
θ₀
y
r̄₂
s₂
D
R
a
θ₂
x

Figure 9. Definition Diagram for two Coaxial Rings in a Uniform Flow.

$\frac{R}{D}$	Ω
$\rightarrow \infty$	.742
20	.742
5	.741
2	.711
1	.679
.5	.584
.3	.497
.2	.501
.1	.920
.05	2.03

FIGURE 10: Table of Values for Ω as the Ratio R/D Varies

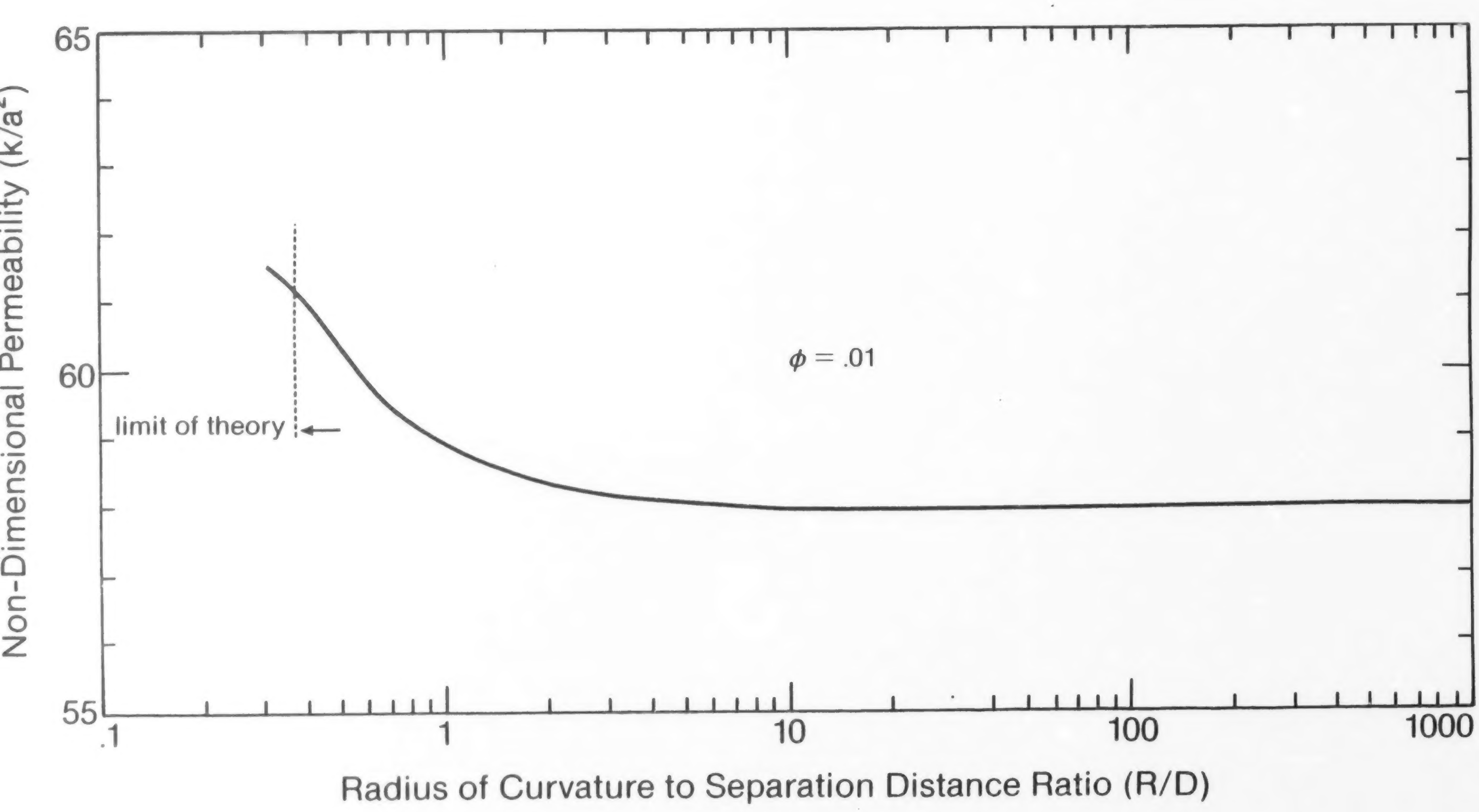

Figure 11. Non-Dimensional Permeability versus Radius of Curvature for a Solid Volume Fraction of $\phi = .01$

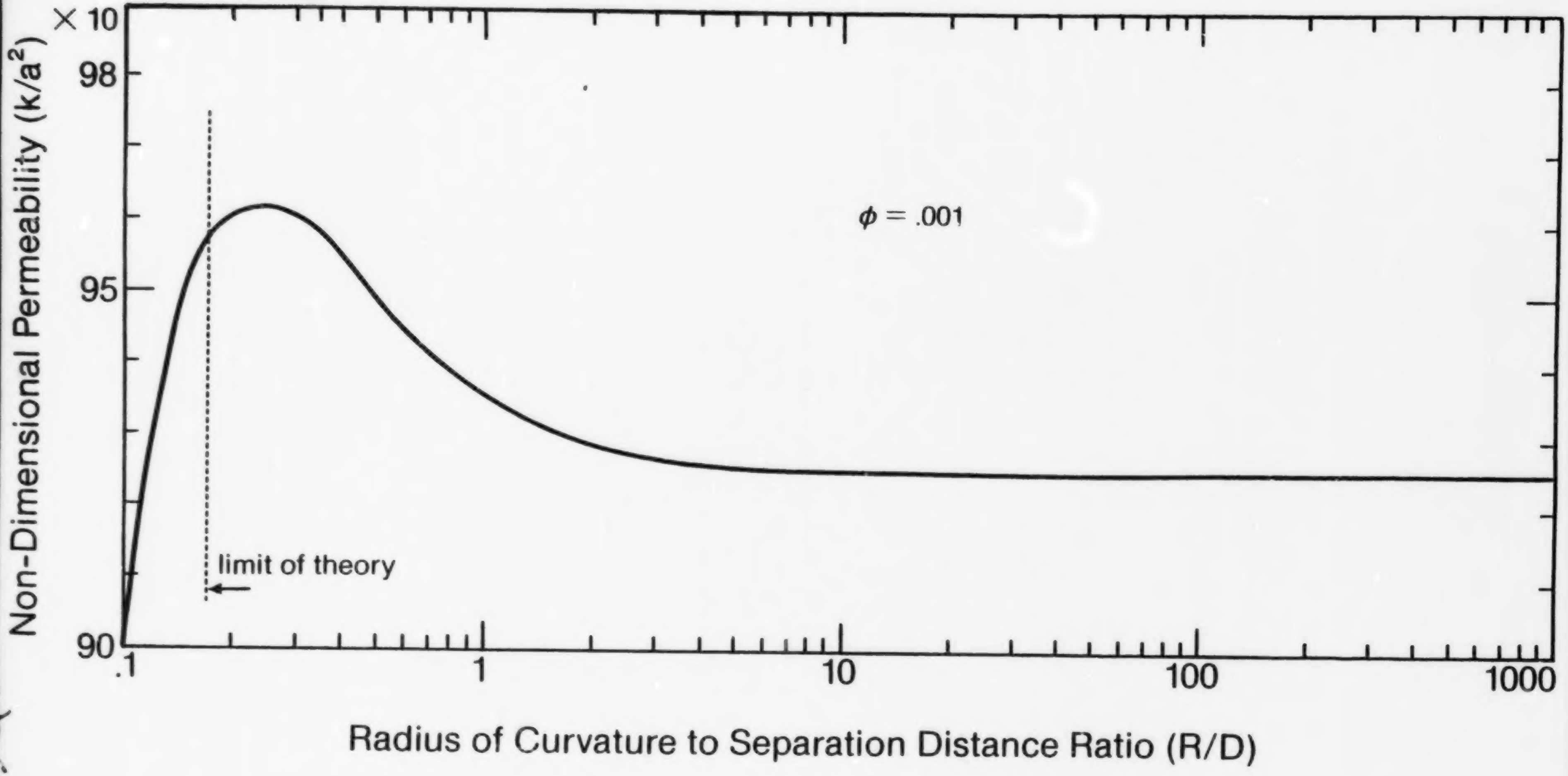

Figure 12. Non-Dimensional Permeability versus Radius of Curvature for a Solid Volume Fraction of $\phi = .001$

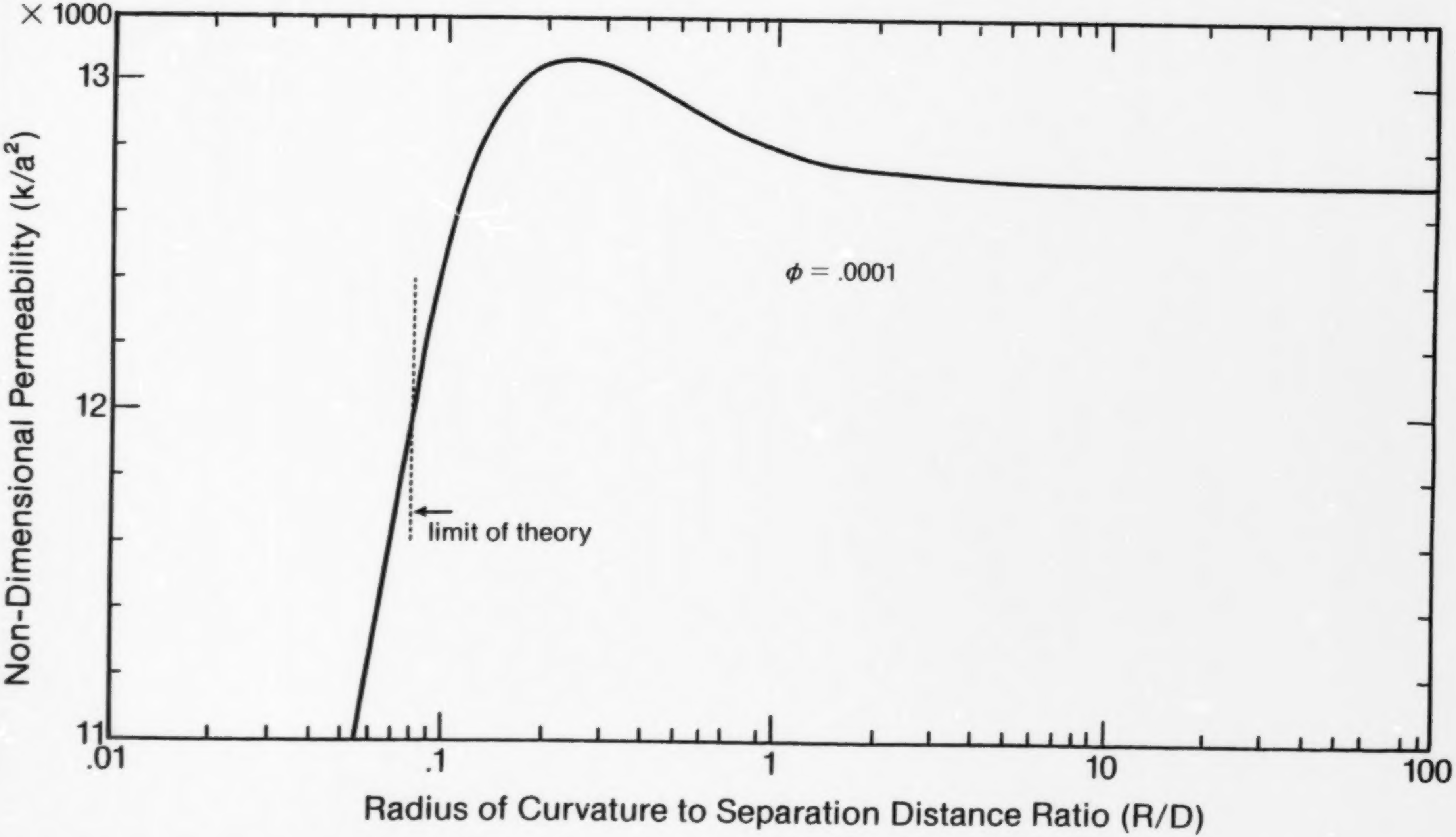

Figure 13. Non-Dimensional Permeability versus Radius of Curvature for a Solid Volume Fraction of $\phi = .0001$

Ø	$\frac{k}{a^2}$ as predicted by				
	Davies	Speilman & Goren	Jackson & James	Present Work R/D → ∞	Present Work R/D = .3
.3	.151	.26	n.v.	n.v.	n.v.
.1	1.89	2.5	2.06	2.34	n.v.
.03	12.0	16	12.9	13.8	n.v.
.01	62.5	67	55.1	57.9	61.6
.006	135	130	105	109	115
.001	n.v.	1000	897	925	962
.0001	n.v.	14600	12400	12700	13100

n.v. Theory not valid.

FIGURE 14: Table of Values of the Non-Dimensional Permeability (k/a^2) Versus the Solid Volume Fraction (Ø) for Different Theories

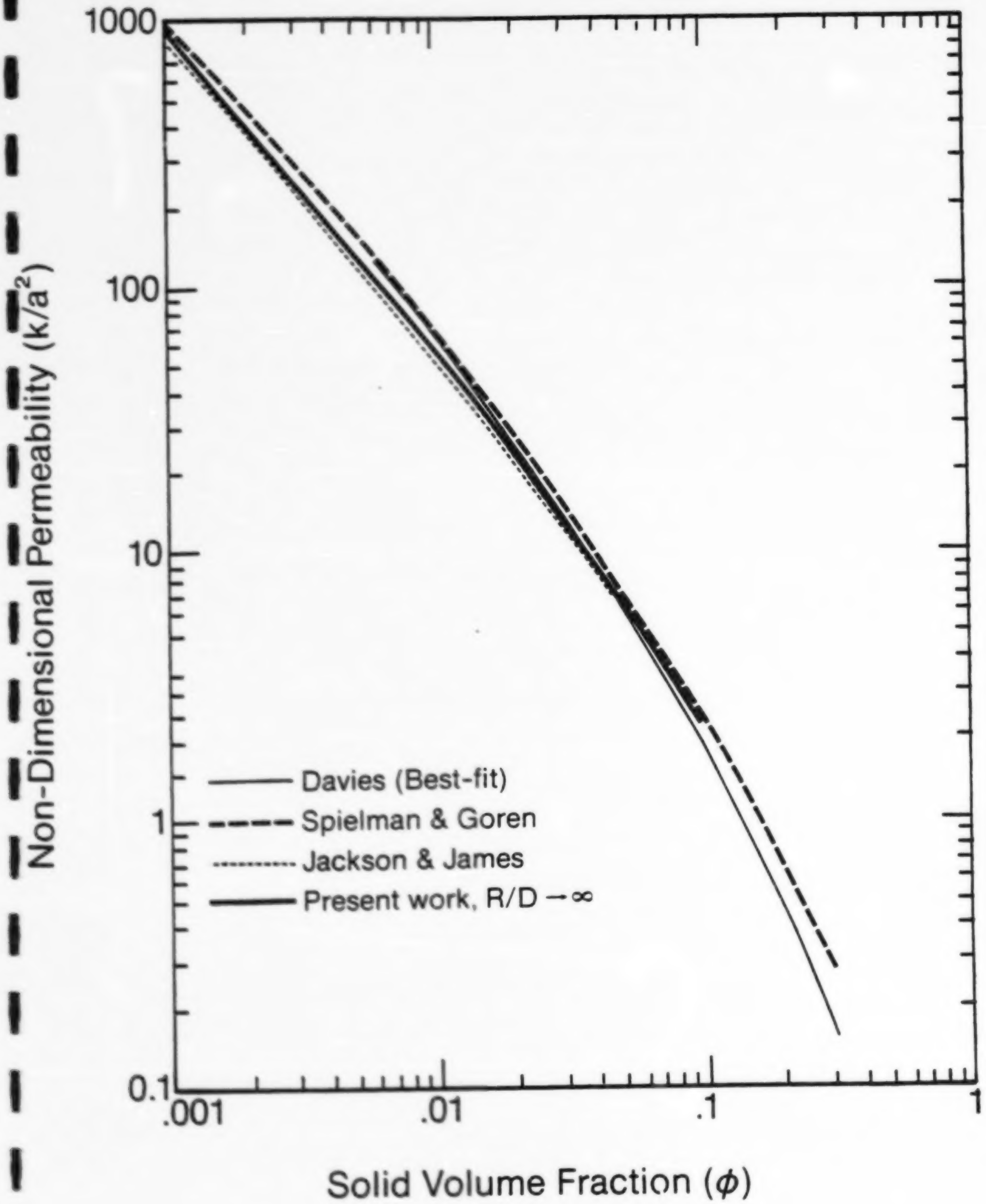

Figure 15. Non-Dimensional Permeability versus Solid Volume Fraction for Several Theories

$\frac{R}{D}$	$\frac{k}{a^2}$				
	Ø = .1	Ø = .01	Ø = .001	Ø = .00001	Ø = .00001
$\rightarrow \infty$	2.34	57.9	925	12700	162000
20	2.34	57.9	925	12700	162000
5	2.34	58.0	925	12700	162000
2	2.39	58.4	930	12700	162000
1	2.44	58.9	934	12800	163000
.5	n.v.	60.3	949	12900	164000
.3	n.v.	61.6	962	13100	165000

n.v. Theory not valid.

FIGURE 16: Table of Values of the Non-Dimensional Permeability (k/a^2) Versus the Ratio R/D and the Solid Volume Fraction (Ø)

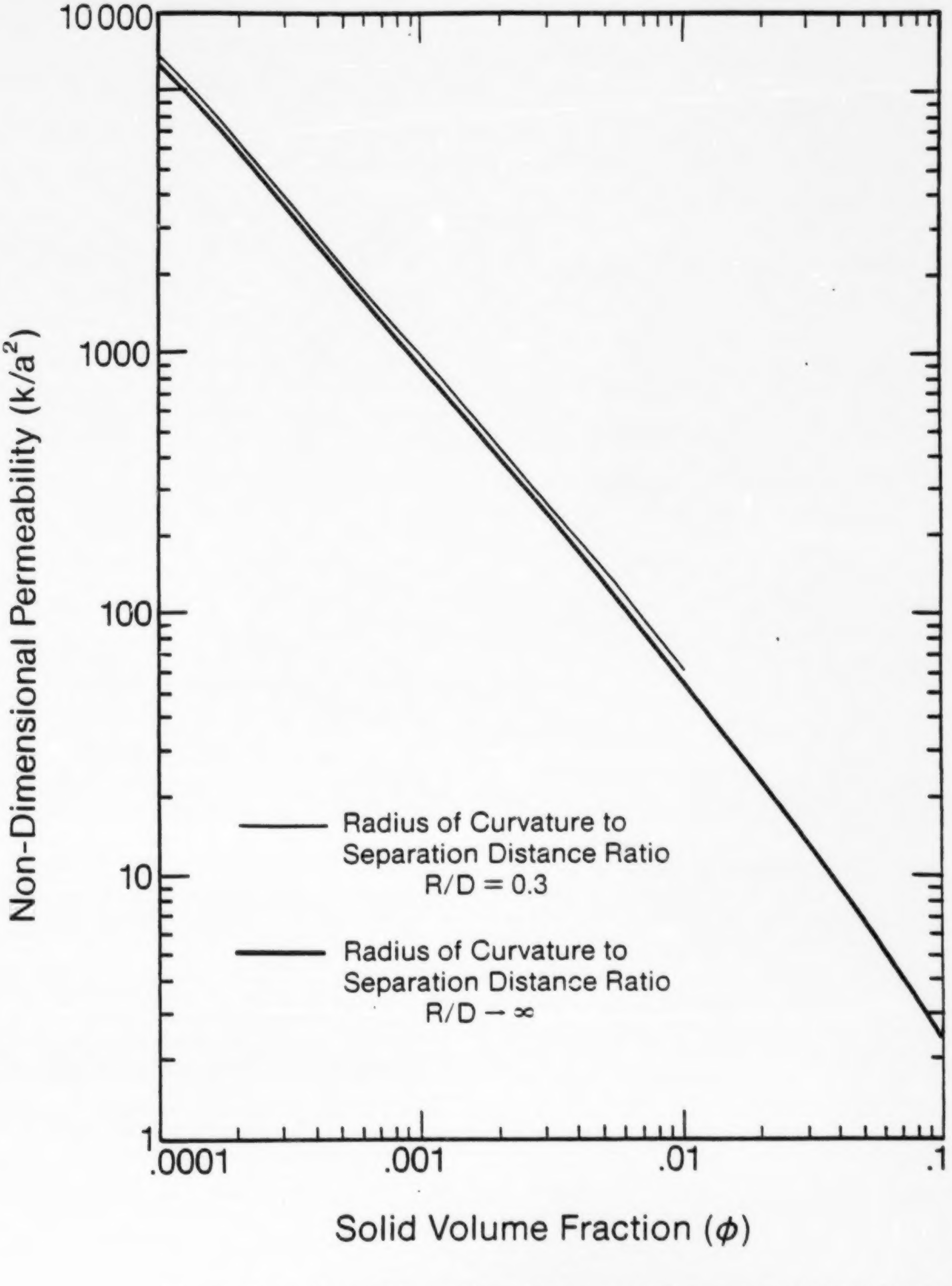

Figure 17. Non-Dimensional Permeability versus Solid Volume Fraction for two values of the Radius of Curvature.

APPENDICES

APPENDIX A

THE DRAG ON A CYLINDRICAL ROD IN UNIFORM FLOW

The problem of Stokes flow past long slender rods has been treated by Burgers (25), Batchelor (26), Cox (20) and Tillett (21). These authors, however, have only dealt with the problem of rods normal and tangential to the direction of flow. This appendix deals with the drag on a cylindrical rod at any orientation to the flow. The average force acting on a rod is also calculated by averaging the drag over flow orientation.

A rod of length L and radius a is oriented by the unit vector

$$\bar{e}_t = \begin{bmatrix} \cos\theta \\ \sin\theta\ \sin\phi \\ \sin\theta\ \cos\phi \end{bmatrix}$$

where the angles θ and ϕ are those of Figure A1. The vector $\bar{r}_0$ going from a general point on the rod to the point s_0 is

$$\bar{r}_0 = -l\ \bar{e}_t$$

where s_0 is a point given by the vector

$$\bar{s}_0 = L(\frac{1}{2} - \alpha)\ \bar{e}_t.$$

The parameter α is a real number between 0 and 1.

The far field velocity can be taken along the x-axis without loss of generality, and the normal and tangential components of velocity are given by

$$\bar{U}_n = U\sin\theta \begin{bmatrix} \sin\theta \\ -\cos\theta\ \sin\emptyset \\ -\cos\theta\ \cos\emptyset \end{bmatrix} \ ; \ \bar{U}_t = U\cos\theta \begin{bmatrix} \cos\theta \\ \sin\theta\ \sin\emptyset \\ \sin\theta\ \cos\emptyset \end{bmatrix}$$

where U is the magnitude of the far field velocity. The force components, according to equations 16 and 17, are

$$\bar{f}_n = -T\ \bar{U}_n \ ; \ \bar{f}_t = -T\bar{U}_t$$

and the sum of these gives the total force fector

$$\bar{f} = -TU \begin{bmatrix} (\gamma-1)\ \sin^2\theta + 1 \\ -(\gamma-1)\ \cos\theta\ \sin\theta\ \sin\emptyset \\ -(\gamma-1)\ \cos\theta\ \sin\theta\ \cos\emptyset \end{bmatrix}$$

This is the force of the Stokeslets distributed along the centerline of the rod as stated in the slender body theorem. This theorem gives the vector equation

$$0 = \bar{U} + \frac{\bar{f}_n(s_0)}{4\pi\mu} + \frac{1}{8\pi\mu} \int_{|l|>\delta} \left(\frac{\bar{f}}{r_0} + \frac{(\bar{f}.\bar{r}_0)\bar{r}_0}{r_0^3}\right) dl,$$

where $\delta = \frac{\sqrt{e}}{2}a$.

Here, the vector $\bar{f}_N$ is independent of its position of the rod; therefore

$$\bar{f}_n(s_0) = \bar{f}_n$$

for all values of α. The dot product $(\bar{f}.\bar{r}_0)$ is simply $(\bar{f}_t.\bar{r}_0)$ since $\bar{r}_0$

has no component normal to the rod; thus

$$(\bar{f}.\bar{r}_0) = TUl\cos\theta$$

The theorem expressed along the three axes gives:

$$0 = U - \frac{T\gamma U \sin^2\theta}{4\pi\mu} + \frac{I_1}{8\pi\mu} \qquad \text{(A1)}$$

on the x-axis,

$$0 = \frac{T\gamma U \sin\theta \cos\theta \sin\phi}{4\pi\mu} + \frac{I_2}{8\pi\mu} \qquad \text{(A2)}$$

on the y-axis, and

$$0 = \frac{T\gamma U \sin\theta \cos\theta \cos\phi}{4\pi\mu} + \frac{I_3}{8\pi\mu} \qquad \text{(A3)}$$

on the z-axis, with

$$I_i = A_i \left[\int_{-(1-\alpha)L}^{-\delta} + \int_{\delta}^{\alpha L} \right] \frac{dl}{l}, \quad i = 1,2,3.$$

The coefficients are given by

$$A_1 = -TU\ ((\gamma-2)\sin^2\theta + 2)$$
$$A_2 = TU\ (\gamma-2)\cos\theta \sin\theta \sin\phi$$
$$A_3 = TU\ (\gamma-2)\cos\theta \sin\theta \cos\phi.$$

The y and z components (equations A2 and A3) are clearly the same. If

$$I_i' = \left[\int_{-(1-\alpha)}^{-\delta} + \int_{\delta}^{\alpha L} \right] \frac{dl}{l}$$

then the y and z equations become

$$0 = 2\gamma + (\gamma-2) I_i' . \qquad (A4)$$

The integral is straightforward

$$I_i' = \ln(1-\alpha)L - 2\ln\delta + \ln\alpha L$$

or

$$I_i' = \ln(1-\alpha)\alpha + 2\ln\frac{2L}{a} - 1$$

The average value of $\ln(1-\alpha)\alpha$ as α varies from 0 to 1 is

$$\langle \ln(1-\alpha)\alpha \rangle = -2$$

which gives

$$I_i' = 2\ln\frac{2L}{a} - 3.$$

Since the theorem states that the velocity is zero at a radial distance a in the cross-section passing through s_0, the averaging over all values of α insures that, on average, the velocity is zero on the whole surface of the rod of radius a.

Equation A4 gives

$$\gamma = 2\left(\frac{\ln\frac{2L}{a} - \frac{3}{2}}{\ln\frac{2L}{a} - \frac{1}{2}}\right) .$$

Equation A1 can now be solved for T,

$$T = \frac{2\pi\mu}{\ln\frac{2L}{a} - \frac{3}{2}} .$$

The drag on the rod is simply

$$\bar{F} = -\int_{\frac{1}{2}}^{\frac{1}{2}} \bar{f}dl$$

which is

$$\bar{F} = -\bar{f}L.$$

Using the relation for $\bar{f}$, the drag on a rod in a uniform flow is

$$\bar{F} = TUL \begin{bmatrix} (\gamma-1)\ \sin^2\theta + 1 \\ -(\gamma-1)\ \cos\theta\ \sin\theta\ \sin\phi \\ -(\gamma-1)\ \cos\theta\ \sin\theta\ \cos\phi \end{bmatrix}$$

A rod aligned with the flow ($\theta = 0$) has a drag of

$$\bar{F} = \frac{2\pi\mu\bar{U}L}{\ln\frac{2L}{a} - \frac{3}{2}} . \qquad (A5)$$

This result agrees with Cox.

A rod normal to the flow ($\theta = \frac{\pi}{2}$) has a drag of

$$\bar{F} = \frac{4\pi\mu\bar{U}L}{\ln\frac{2L}{a} - \frac{1}{2}} . \qquad (A6)$$

This result also agrees with Cox.

The average drag over all orientations is given by

$$\bar{F}_{av} = \frac{1}{4\pi} \int_0^{2\pi} \int_0^{\pi} \bar{F} \sin\theta \, d\theta \, d\phi$$

which gives

$$\bar{F}_{av} = \frac{10}{3} \frac{\pi\mu \bar{U} L}{\ln\frac{2L}{a} - \frac{7}{10} + 0\left[\frac{1}{\ln\frac{2L}{a}}\right]} \qquad (A7)$$

APPENDIX B

INTEGRATION OF I_d AND I_e

The integration of I_d and I_e, defined by

$$I_d = \int_{S_2} \frac{ds_2}{r_2} \qquad (B1)$$

and

$$I_e = \int_{S_2} \frac{ds_2}{r_2^3}\,, \qquad (B2)$$

where all parameters are defined in Chapter III, is used in the derivation of the drag on two coaxial rings. The calculation of these integrals requires the change of variable

$$\xi = 2\beta + \pi$$

where ξ is defined in the text and β is a dummy variable. The element of integration becomes

$$ds_2 = 2R d\beta$$

therefore the contour integrals I_d and I_e are written

$$4R \int_0^{\frac{\pi}{2}} \frac{d\beta}{r_2} \qquad (B3)$$

and
$$4R \int_{0}^{\frac{\pi}{2}} \frac{d\beta}{r_2} \qquad \text{(B4)}$$

respectively, since r_2 is an even function of β, given by

$$r_2 = \frac{2R}{\sqrt{m'}} \Gamma \qquad \text{(B5)}$$

where
$$\Gamma = (1-m' \sin^2\beta)^{0.5}$$

and
$$m' = \frac{1}{\frac{D^2}{4R^2} + 1} .$$

By replacing equation B5 into equation B3 and B4, the integrals become

$$I_d = 2\sqrt{m'} \int_{o}^{\frac{\pi}{2}} \frac{d}{\Gamma}$$

and
$$I_e = \frac{m'\sqrt{m'}}{2R^2} \int_{o}^{\frac{\pi}{2}} \frac{d}{\Gamma^3} .$$

These can be integrated using tables of integration to become

$$I_d = 2\sqrt{m'}\ K(m')$$

and
$$I_e = \frac{1}{2R^2} \frac{m'\sqrt{m'}}{1-m'} E(m')$$

where K(m') and E(m') are complete elliptic integrals of the first and second kind respectively.

By making use of the identity

$$\frac{D^2}{4R^2} = \frac{1-m'}{m'} ,$$

I_e becomes

$$I_e = \frac{2\sqrt{m'}}{D^2} E(m').$$

The integration of equations B1 and B2 is then given by

$$I_d = 2\sqrt{m'}\ K(m') \tag{B6}$$

and

$$I_e = \frac{2\sqrt{m'}}{D^2} E(m'). \tag{B7}$$

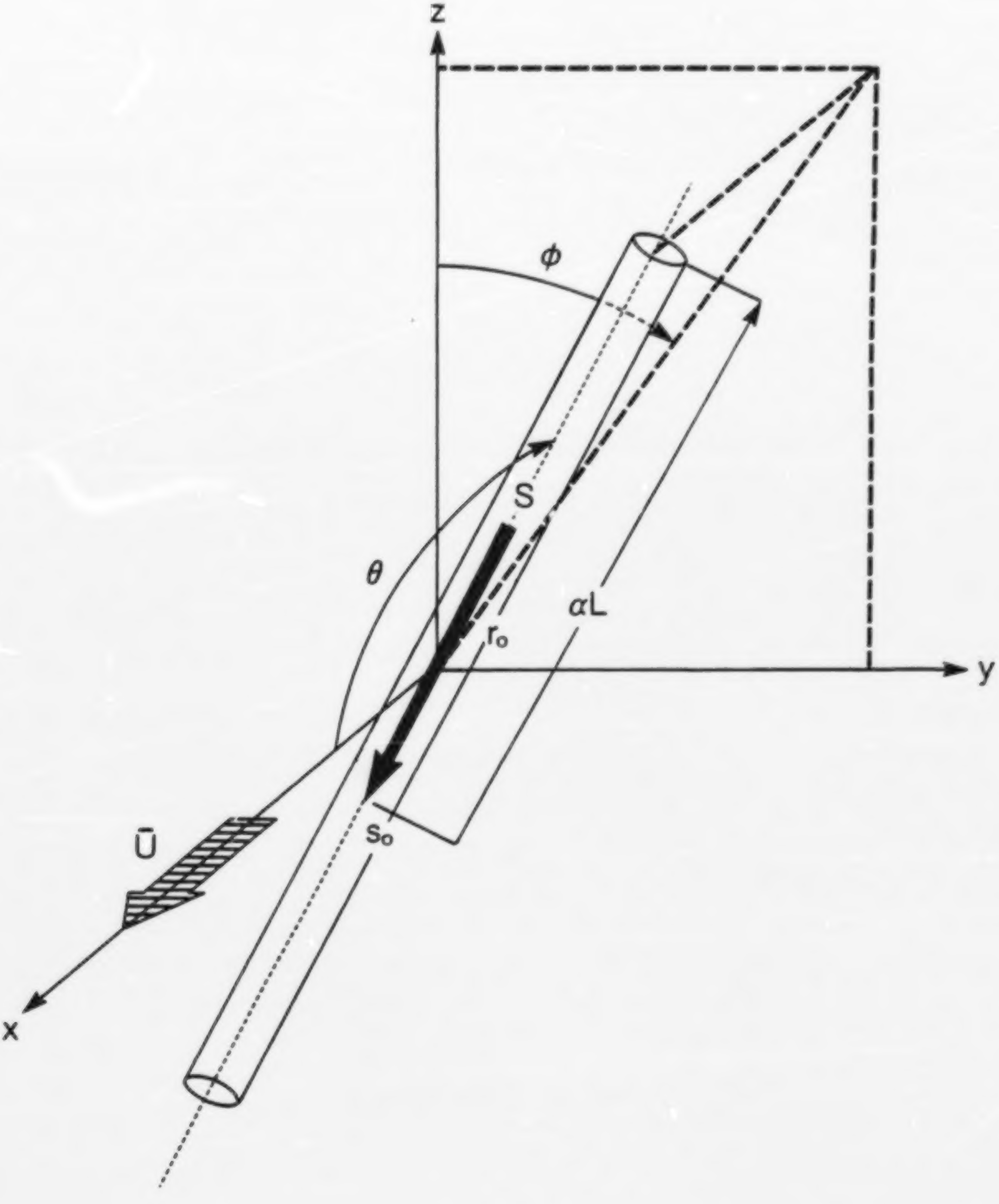
z
φ
S
θ
αL
r₀
y
Ū
s₀
x

Figure A1. Definition Diagram for a Rod in a Uniform Flow

Hydrodynamics of Polymers in Solution

PART II: PERMEABILITY MEASUREMENTS OF POLYMER CHAINS IN SOLUTION

by

D. F. James, Ph.D., P.Eng.
D. G. Kimbell, B.A.Sc.
C. R. Fraser, B.A.Sc.

Work Conducted for the Department of Energy, Mines and Resources

DSS File No. 03SQ.23440-3-9088

CANMET Scientific Authority: Dr. W. Friesen

March, 1985

S & J Engineering Inc.
403 Wellesley St. E.
Toronto, Ontario M4X 1H5

ABSTRACT

The permeability of a concentrated polymer solution was determined by confining the solution between solvent-permeable membranes in a test cell and measuring the pressure drop across the cell at known flowrates . The flowrates were low enough that the entangled chains were not packed by the flow, because the pressure drop was linear with flowrate. From the flow data, the permeability of the solution was determined from Darcy's Law. The fluids tested were aqueous solutions of polyacrylamide and polyethylene oxide, with molecular weights of order 10^6 and for concentrations between .1% and 2% by weight. For the polyacrylamide, the permeability decreased with concentration in a manner consistent with theories for flow through fibrous porous media; a comparison with prior hyaluronic acid data suggests that the hydrodynamic diameter of the polyacrylamide chain is slightly more than 10 Å. Tests with NaCl in the solvent and with a different charge density along the chain indicate that the hydrodynamic diameter is not affected much by these parameters. For polyethylene oxide, the permeability decreased with concentration much more rapidly, suggesting that its hydrodynamic diameter increases with concentration.

TABLE OF CONTENTS

Page

Abstract i

1. OBJECTIVE

1.1 General Objective 1
1.2 Prior Work 2
1.3 Specific Objectives 3

2. EXPERIMENTAL APPARATUS

2.1 Overall Description 5
2.2 Pressure Drop Measurement 5
2.3 Flowrate Measurement 6
2.4 Test Cell Assembly 7
2.5 90 mm Test Cell 7
2.6 47 mm Test Cells 8

3. SOLUTION PREPARATION

3.1 Solvent 9
3.2 Solute 10
3.3 Solution Preparation 13

4. MEMBRANE INVESTIGATION

4.1 Membranes Used 14
4.2 Clogging 15
4.3 Effect of Pore Size 16
4.4 Membrane Support 16

5. DATA

5.1 Reduction of Permeation Data 17
5.2 Permeation Data 18
5.3 Viscometry Data 19

6. DISCUSSION OF RESULTS

6.1 Linearity of Permeation Data 21
6.2 Zero-Flow Pressure Differential 21
6.3 Comparison to Prior Work 22
6.4 Effect of Ions 23

Figures

1. OBJECTIVE

1.1 General Objective

The goal of the present work is to find the permeation characteristics of polymer chains in solution, in particular to find the hydrodynamic resistance of the dissolved chains when solvent flows through them. In a concentrated solution, the chains are entangled and form a skein or mesh. When the solution is flowing, the skein moves along with the flow, but there is generally a relative velocity between the skein and the solvent. The skein thus behaves as a fibrous porous medium, somewhat like cotton batting. This concept of modelling the dissolved polymer as a fibrous porous medium is most appropriate for very long chains, and polymers used in energy applications are of this type because molecular weights are generally in the range of 10^6 to 10^7.

Knowledge of the flow resistance of polymer chains will be useful for a number of flow problems. Specifically, it can be applied to the enhanced oil recovery technique known as polymer flooding. In this technique, water mobility is significantly reduced by polymer adsorption onto rock pore surfaces and by polymer clogging of rock pores. Both mechanisms retard the flow of water and therby improve the displacement of oil. Knowledge of the permeation characteristics of a polymer skein would enable petroleum engineers to estimate the flow resistance caused by polymer chains in porous oil-bearing rock.

Knowledge of chain flow resistance can be applied to the many other situations where there is relative motion between solvent and chains. Hence there is a potential application to the entire field of polymer solution rheology and to all situations in which polymers are used as additives for hydrodynamic effect.

This study may also enable an estimate to be made of the hydrodynamic radius of the polymer chain. Part I showed how the permeability k of a randomly-wound fibrous porous medium is related to the fibre radius a and the solid volume fraction ϕ . By measuring the permeability of a solution of known concentration, i.e. of known ϕ, one can use the equations developed in Part I to determine the effective hydrodynamic radius of the chain - viz. the radius if it were a solid strand of circular cross-section.

1.2 Prior Work

The technique for the present work is based on the work of Jackson and James[1], who determined the permeation characteristics of hyaluronic acid, a biological polymer found in various tissues. Their aim was to find out if hyaluronic acid was the principle agent in causing the high resistance of flow through muscle tissue. Their experiment was simple in concept. It consisted of enclosing a hyaluronic acid solution of known concentration between two solvent-permeable membranes, then pushing solvent through this system and measuring the flowrate and pressure drop. The known resistance of the membranes was subtracted from the measured pressure drop to obtain the pressure drop due to the polymer alone. Jackson and James found that, for low flowrates, the pressure drop was proportional to the flowrate, confirming that the polymer chains acted as a porous medium. This enabled the permeability k of the hyaluronic acid solution to be calculated from Darcy's Law,

$$\frac{Q}{A} = \frac{k}{\mu}\frac{\Delta P}{L} ,$$

where Q is the volumetric flowrate, A is the flow area, μ is the (dynamic) viscosity of the solvent, and $\Delta P/L$ is the pressure gradient in the streamwise direction. The permeability k was found to vary inversely with the hyaluronic acid concentration raised to the power 1.2. Their concentrations ranged from 0.5 to 15 mg/cm^3, so that the solutions were well removed from the gel state and were basically concentrated polymer solutions.

M.L.White[2] carried out a similar experiment with polyacrylamide, except that the concentration range was from 35 to 245 mg/cm^3. With such high concentrations, the solutions were actually gels. Moreover, the gels were cross-linked, so that the structure was different from the entangled chain structure of concentrated solutions. On the basis of his results, White calculated the hydrodynamic diameter of a polyacrylamide chain to be 7.0 Å.

1.3 Specific Objectives

While the resistance characteristics of many chain polymers are of interest, the present work is directed to two water-soluble polymers commonly used in wastewater treatment and in enhanced oil recovery. The two polymers are polyethylene oxide (PEO) and two types of polyacrylamide, unhydrolysed (PAAm) and partially hydrolysed (HPAAm). Both polymers are commercially available, and at high molecular weights they are effective as flocculants (or coagulants) and thickeners.

Of primary interest for each polymer is the dependence of the permeability k on solution concentration c. This necessitates finding k over a range of concentrations of each polymer. The lower end of the range is dictated by the concentration necessary for entanglement, i.e. the beginning of the concentrated regime. The upper end is the concentration which creates a gel or an unmanageably viscous solution. Since the polymers of interest have molecular weights of order 10^6 and above, the useful concentration range is about 1000 ppm to 20,000 ppm (parts per million by weight).

Two more variables arise when dealing with HPAAm. Partially hydrolysed polyacrylamide is essentially a copolymer of acrylamide and acrylic acid. It can be characterized by an additional parameter X, the degree of hydrolysis, which is the fraction of monomer links in the polymer chain that are acrylic acid; X, in principle, can vary from 0% for pure polyacrylamide (PAAm) to 100% for pure polyacrylic acid (PAA).

Hydrolysis is known to have a significant effect on the intrinsic viscosity [n] of HPAAm, and thus it may also affect the permeability k of the solution. The viscometric studies by Klein and Conrad[3] of polyacrylamide in 0.5M NaCl brine showed that, for $\overline{M}_w = 5.5 \times 10^6$, [n] doubled when X varied from 0 to 35%. The presence of salt in solution is also known to affect the intrinsic viscosity of HPAAm. Although this has not been documented by any published calculations, viscometric tests done in this work (described in detail in section 5.3) revealed that the intrinsic viscosity [n] of a 30% hydrolysed polyacrylamide in 0.5M NaCl brine was roughly 20% of its intrinsic viscosity in pure water. This is understood to be due to HPAAm's anionic character.

One aim of this work, therefore, is to know if hydrolysis and salt have the same effects on the permeation characteristics of HPAAm solutions. This can be found by determining the permeability k of HPAAm solutions in brine and by doing this for polyacrylamides of various degrees of hydrolysis.

The relative velocity between a polymer skein and the solvent in which it is dissolved is quite low. Thus it is expected that the appropriate range of flowrates for this work are small. Moreover, the flowrates must be low enough to prevent collapsing of the skein, i.e. the polymer structure must be unaltered by the flow to obtain a linear relation between the pressure drop and flowrate. With linear data, Darcy's Law applies and the permeability of the polymer skein can be found from the data.

2. EXPERIMENTAL APPARATUS

2.1 Overall Description

As indicated by Figure 1, the apparatus for the permeation experiments consists of an upper reservoir, a test cell, a collecting reservoir, connecting tubing, a pan balance, a stopwatch, and a pressure-measurement device. The test cell contains polymer solution confined by two solvent-permeable membranes. Pure solvent is driven by gravity from the upper reservoir into the test cell, through the two membranes and the solution between them, out of the test cell and into the collecting reservoir. Up to three test cells were simultaneously in operation, each with its own apparatus.

The two variables measured in this experiment were the total pressure drop across the cell and the flowrate. At a fixed flowrate, the total pressure drop is the sum of the pressure drops due to the membranes ΔP_m, and the pressure drop due to the polymer solution ΔP_p. For this reason, all tests in this work consisted of two parts: measurements of pressure drop with no polymer solution between the membranes, and measurements at the same flowrates with a polymer solution in the test cell.

2.2 Pressure Drop Measurement

Locations of the pressure taps for the overall pressure drop are indicated in Figure 1. The taps are not actually part of the test cell, rather they are part of the tubing which connects the two reservoirs to the test cell. Because the flowrates in the system are minuscule, friction losses in the tubing are negligible and thus the positions of the taps are arbitrary. Hence the pressure drop reading accurately reflects the pressure drop across the test cell.

Two pressure measurement devices were used in this work: a pressure transducer, and two piezometer tubes. The former was more accurate, more precise, and easier to read. It did, however, require careful calibration initially, and regular zeroing to maintain accurate readings. The piezometer tubes, while less accurate, were cheaper and simpler. They also made it easier to rid the pressure lines of air bubbles. Varying the pressure drop for either device was a simple matter of raising or lowering the upper reservoir. The reservoirs were fixed during a run and thus the driving head decreased during the run. However, since the flowrates were so low, $O(10^{-4})$ cm^3/s, the change in head was negligible and the pressure drop was constant.

2.3 Flowrate Measurement

The flowrate was measured by timing the interval required for a certain mass of solvent to pass through the system. The solvent mass was determined by weighing the collecting reservoir at the beginning and end of the interval. The volumetric flowrate Q was calculated from this mass flowrate and the solvent density.

Three analytical balances were used in this work, one for each test cell. Two read to four decimal places in grams, and the third to two places. To obtain similar accuracies in flowrate,time intervals for the latter balance were correspondingly longer.

Initially, the collecting reservoir had no physical connection with the rest of the system. Solvent dripped through a hypodermic needle into a beaker, and the beaker was weighed at the beginning and end of each time interval.

This approach proved to be unsatisfactory for two reasons. First, the needle created a significant but unnecessary resistance to solvent flow; secondly, it became clear after exploratory testing that solvent evaporation from the reservoir was not negligible. To eliminate these problems, the discharge tube was submerged and the liquid in the collecting reservoir was coated with a thin film of oil.

The experimental system was also found to be very sensitive to small mechanical disturbances. Accidental shaking of any component of the apparatus introduced significant flow transients, as did air currents caused by opening or closing the door of the analytical balance. To minimize such disturbances, the collecting reservoir sat on the pan of the balance during the tests and its mass was monitored at known time intervals.

2.4 Test Cell Assembly

Jackson and James[1] found that reproducible results depended on the complete removal of air bubbles from the test cell. Following their procedure, membranes used in this work were degassed prior to test cell assembly, and the permeation fluid was deaerated. Because the test cell was assembled in a bath of solvent identical to the permeation fluid, the bath solvent too was deaerated.

The membranes were always handled with forceps, to avoid damaging them and to prevent contamination by oil from human skin. The test cell was assembled in the bath and attached to the connecting tubing, which beforehand was filled with solvent and clamped off upstream and downstream. The test cell was then lifted out of the bath and fixed to a retort stand, and the pinchcocks were removed to make the system operational.

2.5 90mm Test Cell

One of the three test cells used in this work was the original cell designed and used by Jackson and James. It is depicted in Figure 2 and is henceforth referred to as the 90 mm cell, since this is the diameter of the membranes it holds. It was always connected to the pressure transducer for the measurement of ΔP, and the two-decimal precision balance was used for measurements of Q.

The cell was designed with three chambers in parallel instead of one large chamber. A perforated titanium plate downstream of each membrane prevented membrane "sagging", or bulging, in the flow direction. As shown in Figure 2, each chamber had a radial hole through which polymer solution was inserted by syringe. O-rings and external clamping pressure were used to seal the cell. All cell components, with the exception of the O-rings and titanium plates, were made of plexiglass.

2.6 47 mm Test Cells

Two additional test cells were built to speed up data acquisition. They were designed to house 47 mm membranes which were found to be more readily available than the 90 mm membranes. The two 47 mm cells are smaller, lighter and simpler in design than the 90 mm cell. As shown in Figure 3, each 47 mm cell has one chamber instead of three, and stainless-steel fine-mesh screens were used for support instead of the perforated titanium plates. Similar to the 90 mm cell, the chamber has a radial hole for syringe injection of the polymer. The entire assembly, save for the screens and two O-rings, is made of plexiglass, so that air bubbles can be spotted. External clamping is unnecessary with this smaller cell. Instead of using bolts, the end pieces and central housing are threaded together, as shown in Figure 3. By greasing the threads with vacuum grease and tightly screwing the components together, the cell is sealed with much less difficulty and much more quickly than the 90 mm cell.

3. SOLUTION PREPARATION

3.1 Solvent

The solvent for the polymer solutions, and the fluid for the permeation tests, was primarily deionized water. Deionized water was not really necessary for the nonionic PEO and PAAm, but it served as a quality solvent. For anionic HPAAm, it was indeed necessary because chain configurations of this polymer are generally very sensitive to ion concentration. Hence the common permeation fluid was deionized water. In the case of HPAAm, the fluid was sometimes brine; because of this polymer's sensitivity to ions, the ionic strength of the solvent was varied in a controlled way.

Prior to testing, Jackson and James filtered their perfusion fluid through the test cell to reduce clogging by particulate matter. In the present work, because of time constraints, all permeation fluid was filtered once through a Millipore membrane (MF-type, .22 μm pore size) and deaerated before addition to the upper reservoir. This produced satisfactory results, but it is recommended that future permeation tests revert to Jackson and James' approach of filtering all fluids - the solvent, the bath fluid and the permeation fluid - through the test cell.

Practical experience revealed the necessity of certain additives for the polymer solutions. The first one, formaldehyde, was necessary to prevent bacteria in the water. Bacteria feed of the oxygen in the PEO chains, thereby breaking the chains. Bacteria can also clog the membranes and are known to produce chain polymers of their own. Since these factors are potentially harmful, small amounts of formaldehyde (approximately 0.03% vol.) were added to all the fluids associated with the permeation tests of PEO.

Formaldehyde cannot be used, however, in the cases of PAAm and HPAAm solutions, because it causes a solution instability. Hence this additive was avoided, but another additive was used for a different purpose. Polyacrylamide solutions of any degree of hydrolysis are known to exhibit "ageing", a long-term decrease in viscosity. Kulicke et. al.[4] found that this behaviour is avoided by adding 2% vol. of 2-Propanol to the solution. Hence in permeation tests of PAAm and HPAAm, all fluids contained 2% vol. of 2-Propanol.

3.2 Solute

Standard polymerization techniques produce a polymer with a distribution of molecular weights. Commercial polymers also tend to contain impurities such as metal oxides and monomer. Because the impurities and the low molecular weight tail of the distribution pose a potential clogging problem for the membranes,there is a need to purify, or fractionate, a polymer sample before it is used in permeation tests.

Fractionation is done by precipitating out the highest-molecular weight fractions of polymer from the solution. Of the various ways this can by done, the only one found practical for the present work was the solvent/nonsolvent technique. This technique simply involves slowly adding a nonsolvent to a solution of the polymer. The nonsolvent forces some of the polymer to precipitate out of solution, beginning (theoretically) with the highest-molecular weight fractions. The precipitate can be removed and used, or else refractionated to eliminate even more low-molecular weight polymer.

This technique was applied to Polyox Coagulant, a PEO produced by Union Carbide. The solvent/nonsolvent system was benzene/heptane. However, viscometric tests of a fractionated sample of Coagulant indicated a mean molecular weight lower than that of the unfractionated sample. This suggests that more high-molecular weight fractions than low-molecular weight fractions were eliminated from the polymer, i.e. the technique was not successful. Consequently, instead of trying to purify commercial PEO,samples of well-characterized PEO were purchased from Toyo Soda Manufacturing Co. of Tokyo, Japan. These had extremely narrow molecular weight distributions, but the maximum available molecular weight was only 1.0×10^6. Since the lower-molecular weight samples would undoubtedly block the pores of the smallest pore membranes available (.025 um pore size), permeation tests were conducted only with the 1.0×10^6 molecular weight sample.

As for polyacrylamide,fractionation of Separan AP273 (a commercial HPAAm produced by Dow Chemical of Sarnia) was tried using water/acetone as the solvent/nonsolvent system. However, time constraints prevented adequate viscometric tests of the fractionated polymer, and again, well-characterized samples were employed. These samples, supplied by the CANMET Coal Research Centre of Devon had known mean molecular weights and degrees of hydrolysis. The four samples are:

CANMET Flocculant 1, $\overline{M}_w - 15 \times 10^6$, $X = 5\%$
CANMET Flocculant 2, $\overline{M}_w = 1 - 5 \times 10^6$, $X = 14\%$
CANMET Flocculant 3, $\overline{M}_w = 1 - 5 \times 10^6$, $X = 26\%$
CANMET Flocculant 4, $\overline{M}_w = 1 - 5 \times 10^6$, $X = 38\%$

Before these samples were obtained, an attempt was made to characterize some commercial samples of PEO and HPAAm on hand. The mean molecular weight $\overline{M}_w$ if each sample was determined by finding its intrinsic viscosity $[n]$, and then using the appropriate Mark-Houwink relation to calculate $\overline{M}_w$. All Mark-Houwink relations are of the form,

$$[n] = k \, \overline{M}_w^{\,b}$$

where k and b are known constants for a polymer - solvent - temperature combination.

This viscometric technique was used to find $\overline{M}_w$ of three different PEO samples and one HPAAm sample, since the constants k and b are known for these samples. Several dilute solutions of each polymer were prepared and tested in a Cannon-Fenske size 50 capillary viscometer. The reduced viscosity n_{sp}/c for each solution was calculated from

$$\frac{n_{sp}}{c} = \frac{n_{solution} - n_{solvent}}{n_{solvent}\ c}$$

where $n_{solvent}$ is the solvent viscosity, $n_{solution}$ the solution viscosity and c the solution concentration. A plot of n_{sp}/c vs. c was made and the intrinsic viscosity [n] was read as the extrapolated value of n_{sp}/c at c=0. Using the appropriate Mark-Houwink constants, $\overline{M}_w$ of the polymer was calculated. These results are presented in chapter 6.

In the case of HPAAm, knowledge of the degree of hydrolysis X is a prerequisite in calculating $\overline{M}_w$. That is, the Mark-Houwink constants k and b, which were determined by Klein and Conrad[3], are functions of X and so X must be known if $\overline{M}_w$ is to be found from [n] data. An effort was initiated to measure X using quantitative analysis by infrared (IR) spectroscopy. Since HPAAm is a copolymer of acrylamide and acrylic acid, the IR spectrum of HPAAm shifts with increasing X from that of PAAm (X = 0%) to that of PAA (X = 100%). It was hoped (and still is) that some property of the spectrum (e.g. height of a particular peak) would prove to be proportional to X and thus become a suitable basis for measuring X of an uncharacterized HPAAm. The spectra of several polyacrylamides of known X were searched in this effort.

Regrettably, due to time constraints and the afore-mentioned difficulties with fractionation, permeation tests of commercial polymers were halted and the four CANMET Flocculant samples were tested instead.

3.3 Solution Preparation

Preparation of the polymer solutions for the test cells followed standard procedures except that a small amount of alcohol was used as a dispersant. The use of 1-Propanol prevented the polymer powder from agglomerating and forming insoluble globules. When 2-Propanol was intended as the solvent additive, it was used instead. This technique minimized the dissolution time, but generally up to two days was needed for complete dissolution. Solutions were stored in airtight containers and kept away from light to avoid polymer chain degradation.

4. MEMBRANE INVESTIGATION

4.1 Membranes Used

Two types of membranes were tried for this permeation study: Millipore MF - type filters and Nuclepore polycarbonate filters. Only the former type have proven to be useful.

The polycarbonate membranes are created by irradiating a polycarbonate film, then chemically etching the particle tracks. The structure is therefore that of a solid disc with many cylindrical holes through it. The structure of the MF - type membranes is far less clear. Photomicrographs of an MF - type membrane surface give it the appearance of a sponge. The manufacturer, however, refers to the membrane as a screen filter with surface particle retention properties.

The MF - type membranes are opaque and approximately 100 μm thick. They are quite brittle in air, less so in water. The polycarbonate membranes, on the other hand, are transluscent and only 1 μm thick. They are so light and flexible that during test cell assembly in the bath, the smallest current would sweep them out of the cell before they were locked in place. Barring this occurrance, permeation tests with the polycarbonate membranes usually yielded inordinately high flowrates. This can only be explained by inadequate sealing of the membranes, probably due to membrane movement before the test cell was properly tightened.

Given the practical difficulties with the polycarbonate membranes, it was decided to cease experimenting with them and to use MF - type membranes in all permeation tests.

4.2 Clogging

Membrane clogging was the most severe problem encountered in this work. Clogging was indicated by an increasing flow resistance over the course of a permeation test. Before and after tests of membrane resistance also indicated clogging; in fact, the resistance after permeation tests was anywhere from 25% to 250% higher than the resistance before.

To investigate what was causing the clogging, two used pairs of membranes were left soaking in solvent for a few days, then re-inserted in the test cell and tested again. The results were conflicting. The first pair of membranes had not been tested following their test with polymer, but it was known that their resistance, along with that of 500 ppm of a polyacrylamide in water, was 16 650 (the units of resistance are those of head differential divided by flow rate: cm $H_2O/cm^3/s$). After soaking in water for seven days, the membrane flow resistance was 16 200. This suggested that the membranes were not being clogged by low-M_w fractions of the polymer, because any polymer in the pores would have diffused out during the soaking period and reduced the membrane resistance considerably. The second pair of membrances, however, after soaking for two days, went from a resistance of 9100 (following polymer permeation test) to a resistance of 7600 (almost its resistance before the polymer permeation test of 7300), suggesting that some of the clogging was caused by the polymer.

Another experiment was devised to help identify what was clogging the membranes. Two new membranes were tested. The system was left running for about two hours at a very high flowrate which sent about 10.5 cm^3 of permeation fluid through the system (more than twice the amount that would normally pass through in a permeation test). The membrane resistance increased from 12 900 to 42 000. Clearly, particulate matter in the fluid was primarily responsible for the clogging.

While clogging was a serious problem, it was surmounted by subtracting the membrane resistance from the total resistance to yield the polymer resistance (as mentioned earlier in section 2.1). Since the membrane resistance was a fraction of the total resistance - it varied from 15% to 45% - the resulting polymer resistance could be accurately determined. The membrane resistance which was subtracted was that measured after the permeation test with a polymer.

4.3 Effect of Pore Size

MF - type membranes are available in a variety of pore sizes and the smallest available - .10, .05, and .025 μm pores - were investigated at length. A small size was desired, of course, to contain the polymer chains, and the lengthy investigation tried to determine which causes the fewest problems. The maximum resistance was obtained, of course, with the finest pore membrane, but these membranes had relatively smaller clogging problems. All in all, there seemed to be no reason to select .025 μm membranes over .05 μm membranes and so both were used in the present work.

4.4 Membrane Support

The titanium plates and fine-mesh screens mentioned in sections 2.5 and 2.6 were introduced to prevent the flow from deforming the membranes, a phenomenon observed by Jackson and James. In the present work, this "sagging" was rarely observed. Rather, swelling was seen, particularly in the 47 mm cells when the polymer concentrations in the cell were high. That is, the upstream membranes bulged outward to increase the volume between the membranes. This bulging was evident when a cell was disassembled. Since accurate permeation data depends on a known and fixed thickness between the membranes all permeation tests with the 47 mm cells have been carried out with the screens placed so that the membranes cannot swell.

5. DATA

5.1 Reduction of Permeation Data

Finding the permeability k of a polymer solution involved finding the flow resistance R_p of the chains and then converting this quantity to permeability. To determine R_p, the first step was to draw a straight line through the P vs. Q data taken with polymer in the cell; the slope of this line is R_{p+m}, the resistance of polymer plus membranes. Then the resistance of the membranes alone, R_m, was found from the slope of the line through the data with membranes only. The polymer resistance, then, is:

$$R_p = R_{p+m} - R_m$$

Darcy's Law in a modified form was used to convert this resistance to permeability. The original form of the Law, as given in section 1.2, is:

$$Q = \frac{k}{\mu} A \frac{\Delta P}{L}$$

Since Δp is related to the measured head Δh by:

$$\Delta p = pg \, \Delta h$$

and since the flow resistance R is $\Delta h/Q$, then Darcy's Law can also be written as

$$k = \frac{uL}{\rho g A} \frac{1}{R}$$

or, equivalently,

$$k = \frac{\nu L}{gA} \frac{1}{R}$$

where ν is the kinematic viscosity. This equation was used for all determinations of k.

As a sample calculation, consider the permeation data for the

2000 ppm CANMET Flocculant 3 solution in brine. These data are plotted in Figure 4 and the slope of a linear regression curve through these data is 360 000. Also shown in the Figure are the ΔP vs. Q data for the membranes alone; the slope of a linear regression curve through these points is 115 000. The flow resistance of the solution is, therefore:

$$\begin{aligned} R_p &= R_{p+m} - R_m \\ &= 360\ 000 - 115\ 000 \\ &= 245\ 000 \text{ cm } H_2O/\text{cm}^3/\text{s} \end{aligned}$$

The dotted line in Figure 4 has a slope of this value.

To calculate k the following parameters were used in the modified Darcy Law: the kinematic viscosity of water at 21.5°C is 0.985×10^{-2} cm^2/s, A for the 47 mm cell is 11.34 cm^2, and L is 0.500 cm. The permeability k of the solution is therefore:

$$\begin{aligned} k &= \frac{(0.985\text{x}10^{-2})(0.500)}{(11.34)(981)(245000)} \\ &= 1.76 \times 10^{-13} \text{ cm}^2 \end{aligned}$$

This is the value which appears in Figure 19 for 2000 ppm concentration.

5.2 Permeation Data

Permeation data for five concentrations of the well-characterized PEO sample were obtained. The concentrations were 1000, 2000, 5000, 10 000, and 20 000 ppm, and the data are shown in Figures 5 to 9. The k values resulting from these data are shown plotted against concentration in Figure 10. To provide a comparison with other permeability results, the data for hyaluronic acid by Jackson and James have been included in this figure.

Permeation data for four concentrations (1000, 2000, 5000, and 10 000 ppm) of CANMET Flocculant 3 ($M_w = 1 - 5 \times 10^6$, X = 26%) in water are presented in Figures 11 to 14. Figure 12 shows two sets of data for the 2000 ppm concentration. One set was obtained by injecting 2000 ppm into the cell and taking flow measurements. The second was obtained by injecting 1000 ppm into the cell when it already contained 1000 ppm after permeation tests at that concentration. The two sets of data are not identical, and the 20% discrepancy is thought to be due to errors in accurately determining membrance resistance. The corresponding k values, and those for the other three concentrations are presented in Figure 15.

In order to assess the influence of ion concentration on flow resistance, the same polymer was tested in 0.5M NaCl solution. This time the concentrations were limited to 1000, 2000, and 5000 ppm and the flow data are given in Figures 16 to 18. The resulting k values are plotted in Figure 19, along with the k values when the ion concentration was zero, i.e. the k values from Figure 15 have been added. The latter are slightly higher, indicating that salt causes a slight decrease in the hydrodynamic diameter.

Another polyacrylamide was tested with a different degree of hydrolysis. Figures 20 to 22 dislplay data for CANMET Flocculant 2 ($M_w = 1 - 5 \times 10^6$, X = 14%) in water at concentrations of 1000, 2000, and 5000 ppm. The k values are presented in Figure 23, and shown with them are the data for Flocculant 3 which, it will be recalled, had twice the degree of hydrolysis (26%). The two sets of data are not substantially different suggesting that hydrolysis of polyacrylamide has only a minor effect.

5.3 Viscometry Data

Initially, it was desired to conduct permeations tests of commercial polymers. Four such polymers were viscometrically characterized prior to our attempts at fractionation; one of them was so characterized after fractionation.

Viscosity data for three commercial PEO samples (Polyox Coagulant, Polyox WSR-301, and Polyox WSR-205) are shown in Figures 24 to 26; they have been plotted in the standard form of reduced viscosity n_{sp}/c vs. concentration c. The intrinsic viscosity of each sample was determined by extrapolation to $c = 0$. The Mark-Houwink constants used to estimate the mean molecular weight of each sample were $k = 1.03 \times 10^{-4}$ and $b = 0.78$, as determined by Shin[5] for PEO. The molecular weights of the three samples were estimated to be: Coagulant, $\overline{M}_w = 3.9 \times 10^6$; WSR-301, $\overline{M}_w = 1.4 \times 10^6$; WSR-205, $\overline{M}_w = 5.2 \times 10^5$.

Following several attempts to fractionate PEO, a sample of fractionated Polyox Coagulant was viscometrically characterized. The viscosity data are shown in Figure 27. The intrinsic viscosity of the sample is shown to be 12.7 dl/g, definitely below the value of 14.3 dl/g obtained for the unfractionated sample (Figure 24). Hence our fractionation technique was considered unsuccessful and this led to the purchase of the PEO standard sample.

Viscosity data for Separan AP273 in two solvents, water and 0.5M NaCl brine, are shown in Figures 28 and 29. From the $[n]$ value of 18.3 dl/g, in Figure 29, $\overline{M}_w$ was found to be 3.6×10^6 using Mark-Houwink constants determined by Klein and Conrad[3] (X was taken to be 30%, the figure quoted by the supplier, Dow Chemical). The data in Figure 28 are nonlinear, for reasons that are not yet clear. However the effect of salt on the viscosity of HPAAm solutions is obvious: the viscosity of Separan AP273 in water is an order of magnitude higher than its viscosity in brine.

6. DISCUSSION OF RESULTS

6.1 Linearity of Permeation Data

The key concept of this work is that entangled polymer chains can act like a rigid porous structure. The chains are flexible and not rigid, of course, but if the flow of solvent through them is slow enough, then hydrodynamic forces on the chain are much less than counteractive diffusive forces and the skein is undeformed by the flow. In this case, the chains are equivalent to a solid structure and so flow through them is governed by Darcy's Law; that is, the pressure drop should be proportional to flowrate. This is indeed the case, for all the permeation graphs show that ΔP is a linear function of Q. Had the flow caused the chains to pack, the permeability would have decreased and the data would not have fallen on a straight line. The linear data confirms, then, that at low flowrates the chains behave as a rigid porous structure.

6.2 Zero-Flow Pressure Differential

Many of the permeation graphs show a small pressure differential at zero flowrate. This differential is apparent by extrapolation of the data, but it was also detected by measurements at zero flowrate; that is, when the flow was shut off, the liquid levels in the manometer tubes approached each other, but a finite difference remained after a long time. This effect is thought to be due to osmotic pressure, perhaps related to molecular forces at the polymer-membrane interfaces. The effect was unexpected because it did not occur in the prior permeation tests with hyaluronic acid. It was not investigated in detail because it appeared that it did not influence the flow data. That is, the pressure drop was still linear with flow rate and thus the 'osmotic pressure' was simply a super-imposed effect. Future work in this area should be directed to finding the source of this effect.

6.3 Comparison to Prior Work

As mentioned earlier, the only prior data of polymer permeability are those for hyaluronic acid.[1] In order to put the present results in context, these prior data have been plotted in Figures 10 and 15. Several comments about these graphs are in order.

(i) In Figure 10, the two sets of data are not close, but they are no different than an order of magnitude and thus the present data certainly fall within the expected range of values. The difference lies, of course, in different hydrodynamic diameters for the two polymer chains. Since the diameter of the hyaluronic acid chains is thought to be about 10 Å [1], the higher permeability of the PEO chains indicates that their diameter is less. This is to be expected because the molecular diameter of a hyaluronic acid chain is about 10 Å, while that for PEO is about 2 Å.

(ii) Part I showed that the prior hyaluronic data are consistent with theories of low Reynolds number flow through fibrous porous media. That is, the predictions of k vs. c are similar quantitatively and qualitatively to the k vs. c data for hyaluronic acid. The present PEO data, however, lie along a line which has a much higher negative slope and so the theories cannot be fitted to the PEO data. This result suggests that the hydrodynamic diameter of PEO chains increases as the concentration increases. Such an effect is unexpected but it is possible that the packing of water molecules around a PEO chain depends on the proximity of adjacent chains. Such an effect would also explain, for example, why PEO is such a good thickener - viz, why solution viscosity increases so rapidly with concentration.

(iii) The PAAm data, on the other hand, in Figure 15 are just below the hyaluronic acid data, suggesting that the hydrodynamic diameter of PAAm is slightly more than 10 Å and that this diameter is not affected by chain density, unlike the PEO chain. These major differences between PEO and PAAm data may help in (eventually) explaining why the rheology of dilute PEO solutions is fundamently different from that of PAAm solutions.

6.4 Effects of Ions

(i) Salt Effects. Figure 19 illustrates the effect of dissolved NaCl on partially hydrolyzed polyacrylamide. For such a polyelectrolyte, the presence of salt usually has a major influence on hydrodynamic effects; Figures 28 and 29, for example, show that salt at a concentration of 0.5M reduces the specific viscosity by a factor of ten. Figure 19 indicates, however, that the hydrodynamic diameter is only slightly decreased by salt because the salt data are somewhat higher. Hence it would appear that the Na^+ ions, shielding negative charges along the chain, disturb the packing of water molecules around the PAAm chain, but not much. This finding suggests that the enormous influence of salt on dilute solutions - such as those used in intrinsic visocity determination - is almost solely because the salt causes the macromolecular coils to shrink.

(ii) Effect of Degree of Hydrolysis. Figure 23 presents a comparison of permeation data for two polyacrylamides with different degrees of hydrolysis. The data for X = 14% are substantially the same as those for X = 26%, suggesting that effective diameter is not affected by the proportion of charged groups along the chain. This finding is consistent with the finding in (i) with regard to salt; that is, if the hydrodynamic diameter is unaffected by the charge-shielding Na^+ ions, it is not surprising that it is also unaffected by the number of charges along the chain.

REFERENCES

1. Jackson, G.W. and James, D.F. "The Hydrodynamic Resistance of Hyaluronic Acid and Its Contribution to Tissue Permeability", in Biorheology, Vol. 19, 317 (1982).

2. White, M.L. "The Permeability of an Acrylamide Polymer Gel", in Journal of Physical Chemistry, Vol. 64, 1563 (1960).

3. Klein, J. and Conrad, K.-D. "Molecular Weight Determination of Poly(acrylamide) and Poly(acrylamide-co-sodium-acrylate)", in Die Makromolekulare Chemie, Vol.179, 1635 (1978).

4. Kulicke, W.-M. et.al. "Preparation, Characterization, Solution Properties and Rheological Behaviour of Polyacrylamide", in Progressive Polymer Science, Vol. 8, 373 (1982).

5. Shin, H. "Reduction of Drag in Turbulence by Dilute Polymer Solutions", Sc.D. Thesis, Massachusetts Institute of Technology (1965).

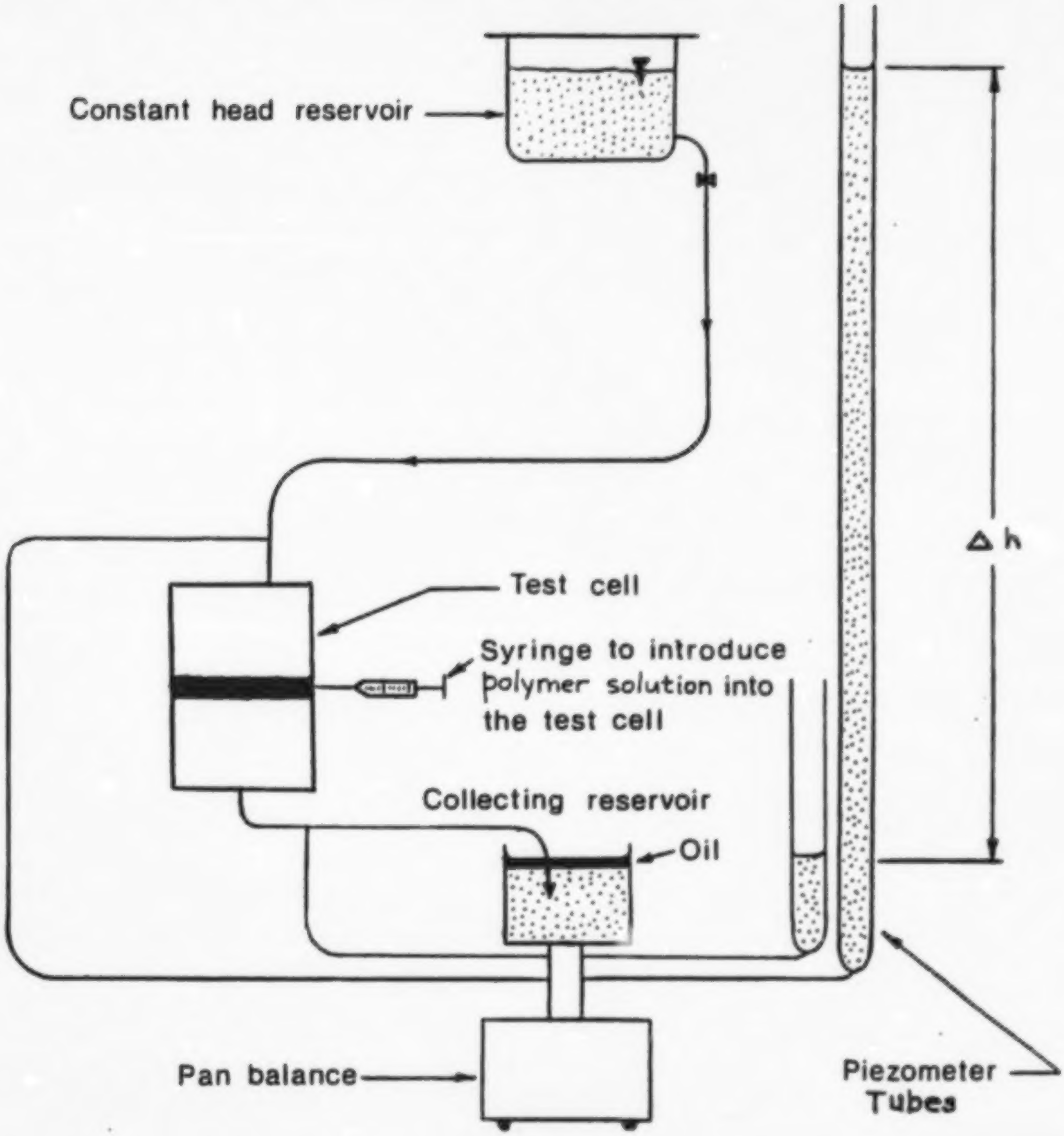
Constant head reservoir
Δh
Test cell
Syringe to introduce polymer solution into the test cell
Collecting reservoir
Oil
Pan balance
Piezometer Tubes

Figure 1

Exploded View of 90 mm Test Cell

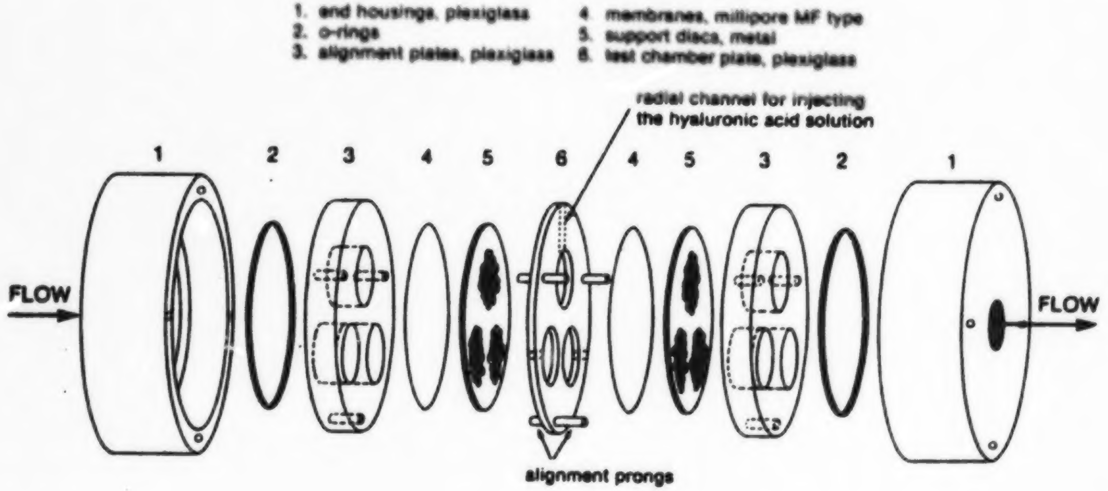
1. end housings, plexiglass
2. o-rings
3. alignment plates, plexiglass
4. membranes, millipore MF type
5. support discs, metal
6. test chamber plate, plexiglass
radial channel for injecting the hyaluronic acid solution
1
2
3
4
5
6
4
5
3
2
1
FLOW
FLOW
alignment prongs

(Figure taken from Ref. 1)

Figure 2

Exploded View of 47 mm Test Cell

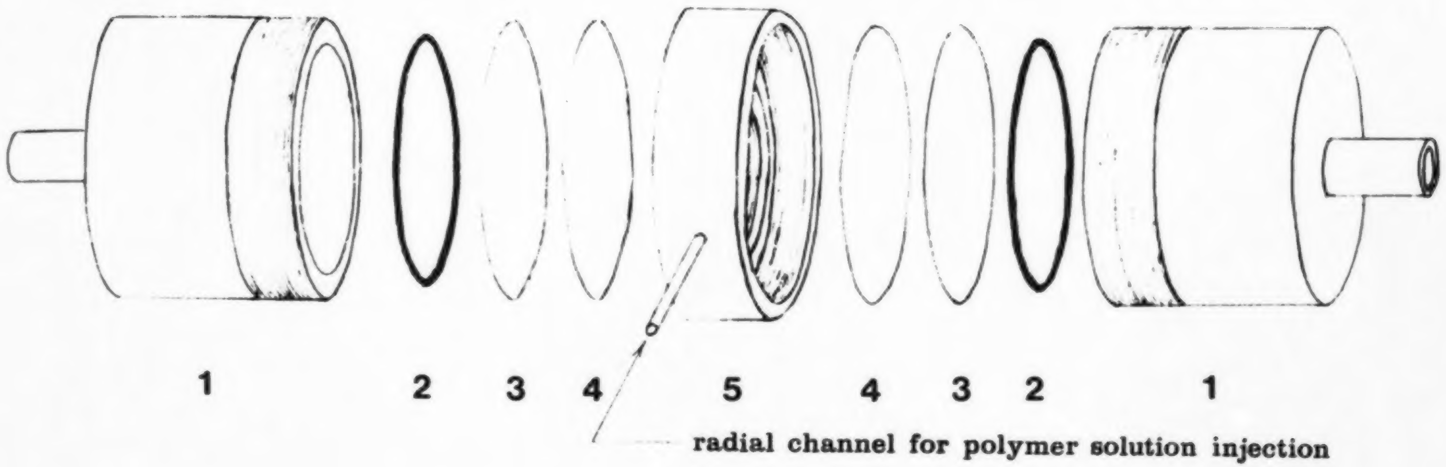
1
2
3
4
5
4
3
2
1
radial channel for polymer solution injection

1 - end piece
2 - O-ring
3 - fine-mesh screen
4 - membrane
5 - test chamber plate

Figure 3

PERMEATION TESTS OF POLYMER SKEINS

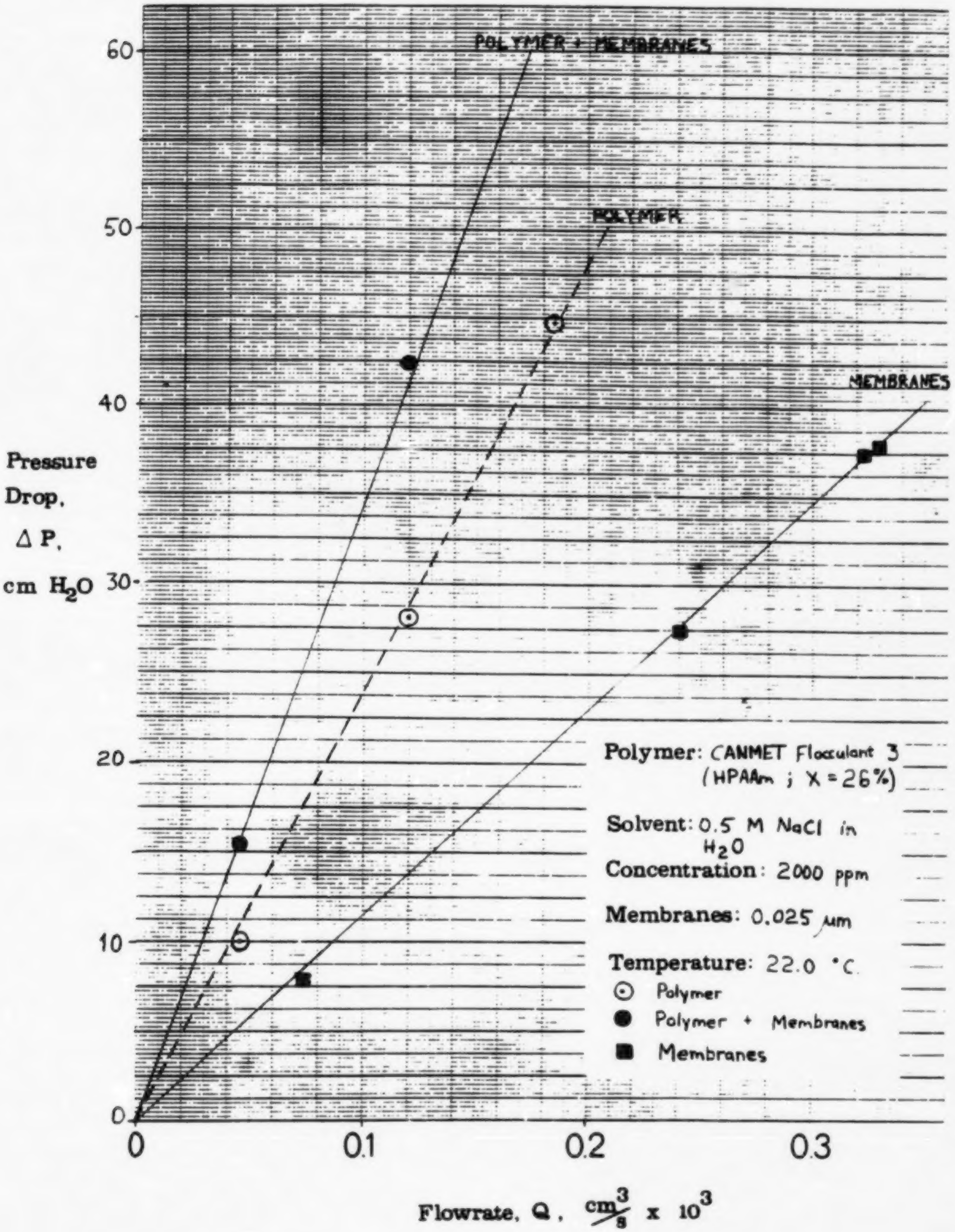

Figure 4

PERMEATION TESTS OF POLYMER SKEINS

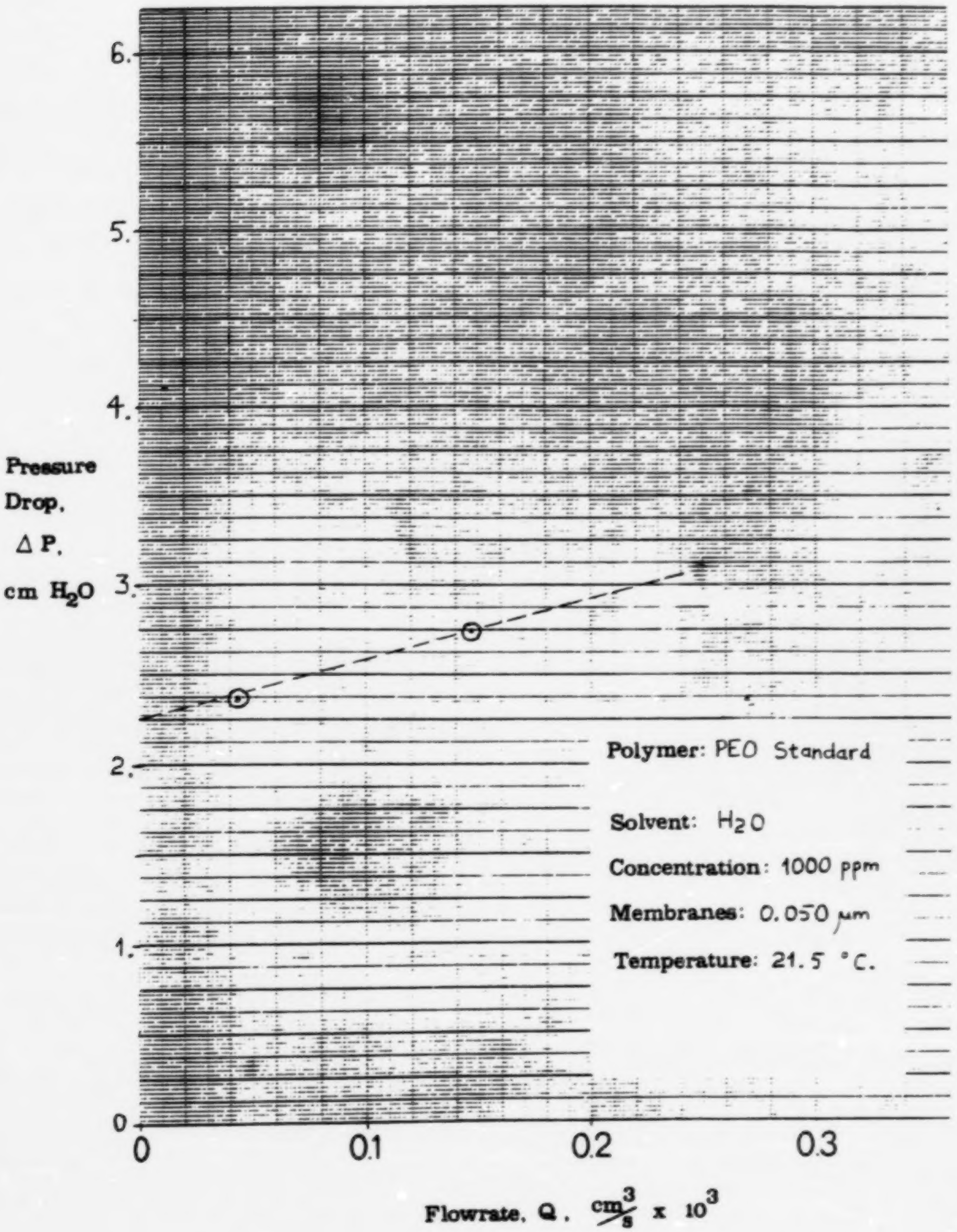

Figure 5

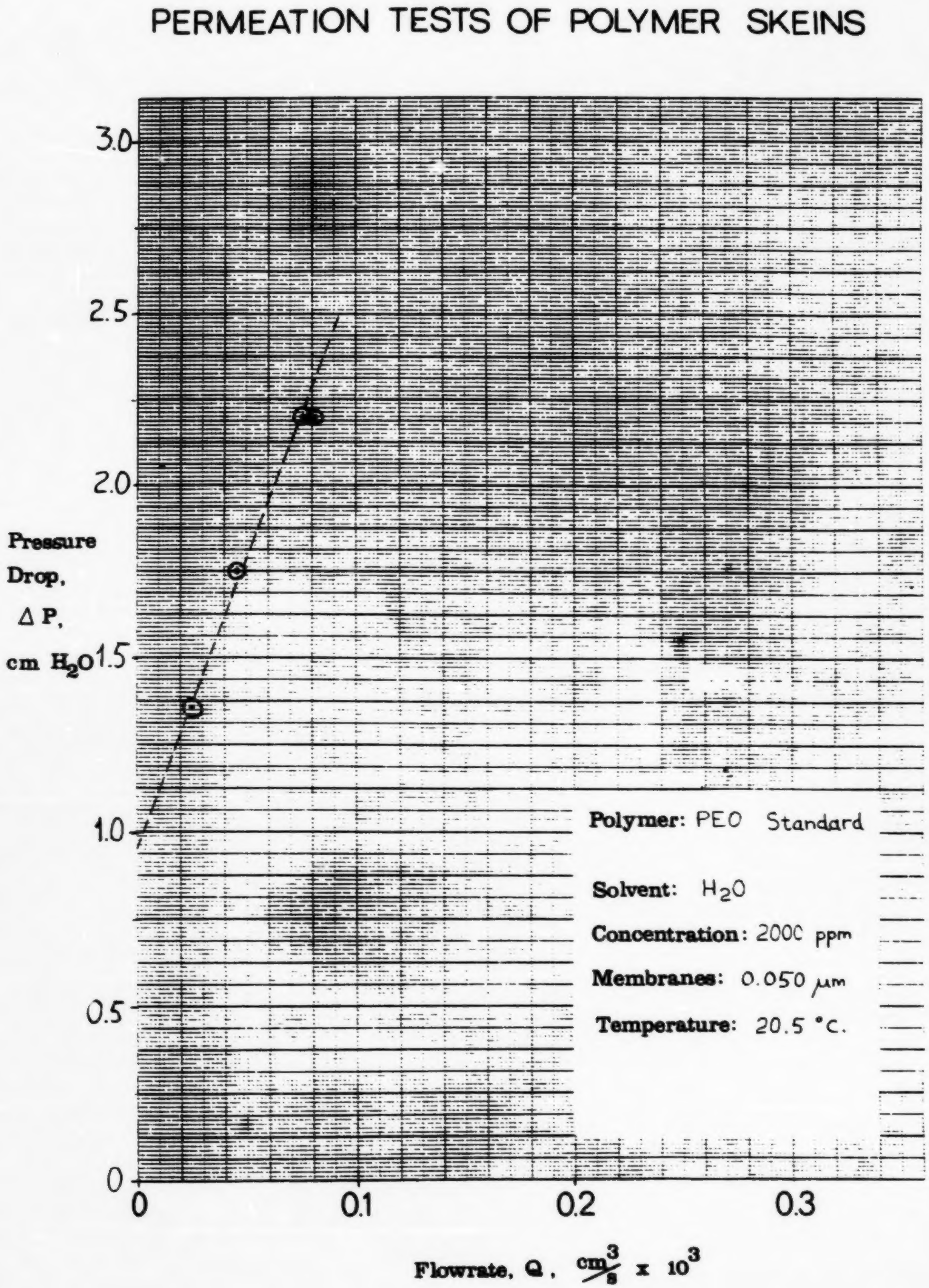
PERMEATION TESTS OF POLYMER SKEINS
3.0
2.5
2.0
1.5
1.0
0.5
0
Pressure Drop, ΔP, cm H_2O
0
0.1
0.2
0.3
Flowrate, Q, $\frac{cm^3}{s} \times 10^3$
Polymer: PEO Standard
Solvent: H_2O
Concentration: 2000 ppm
Membranes: 0.050 µm
Temperature: 20.5 °C.

Figure 6

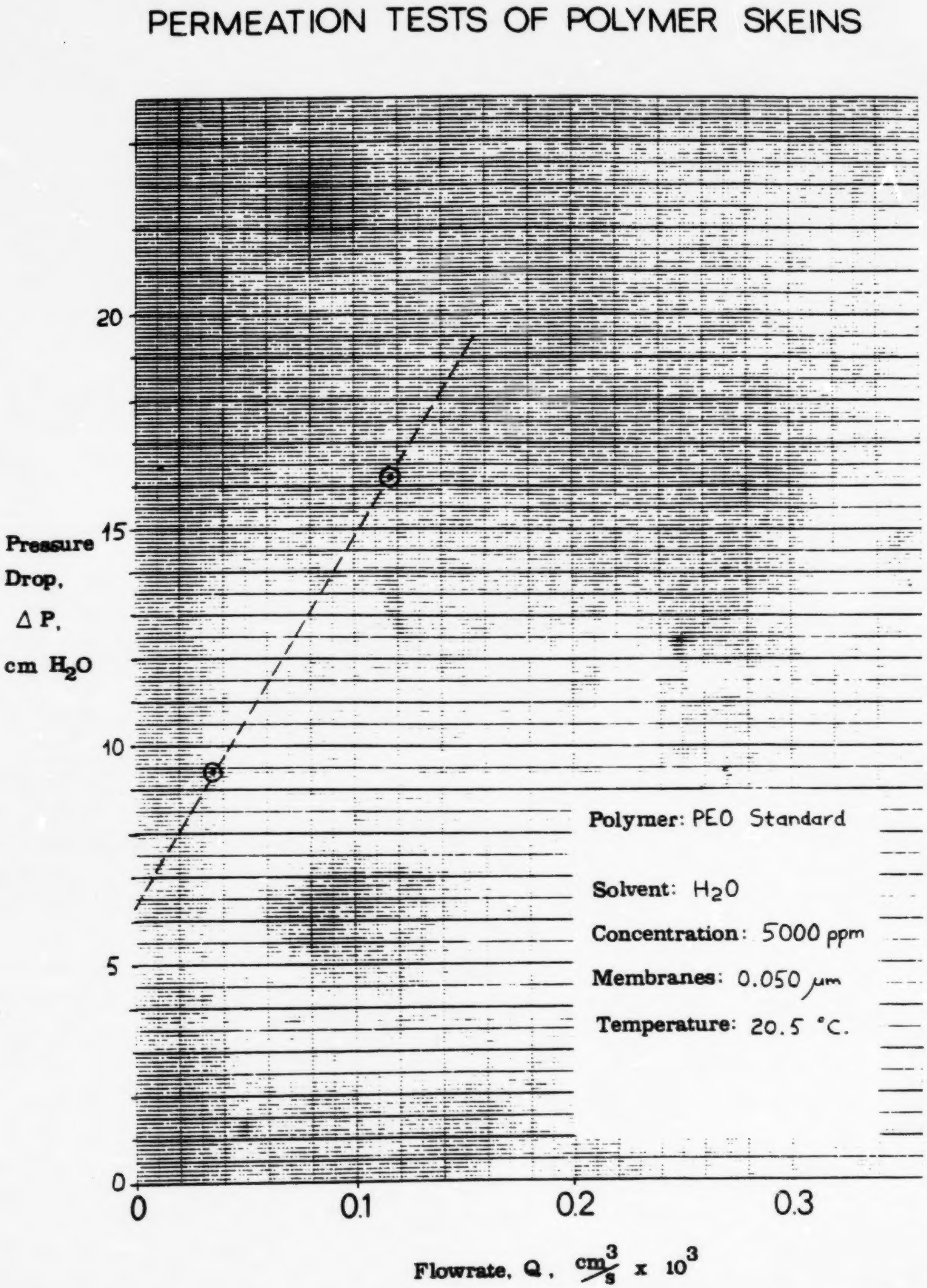

PERMEATION TESTS OF POLYMER SKEINS

Figure 7

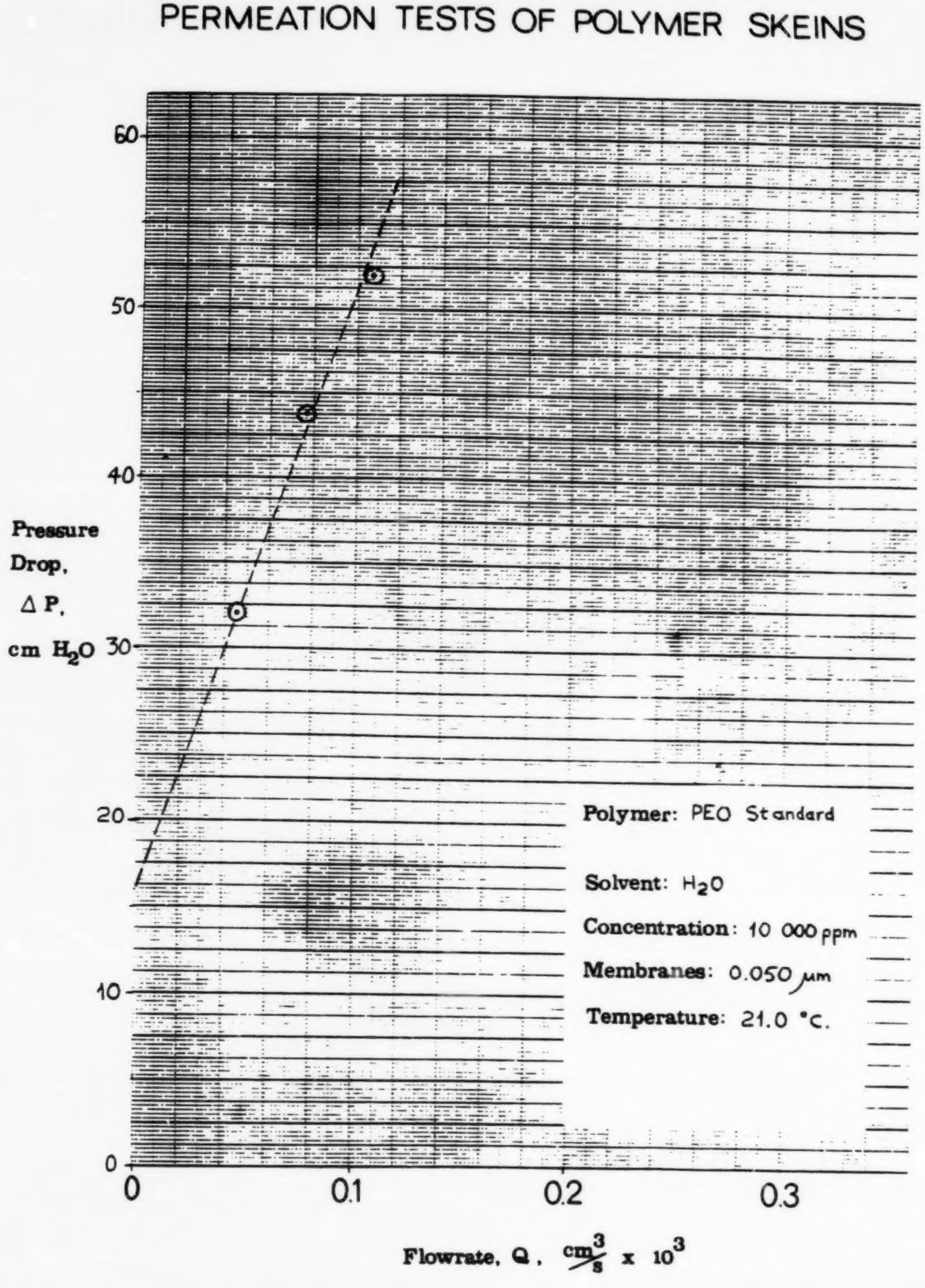
PERMEATION TESTS OF POLYMER SKEINS
60
50
40
30
20
10
0
Pressure Drop, ΔP, cm H_2O
0
0.1
0.2
0.3
Flowrate, Q, $\frac{cm^3}{s} \times 10^3$
Polymer: PEO Standard
Solvent: H_2O
Concentration: 10 000 ppm
Membranes: 0.050 μm
Temperature: 21.0 °c.

Figure 8

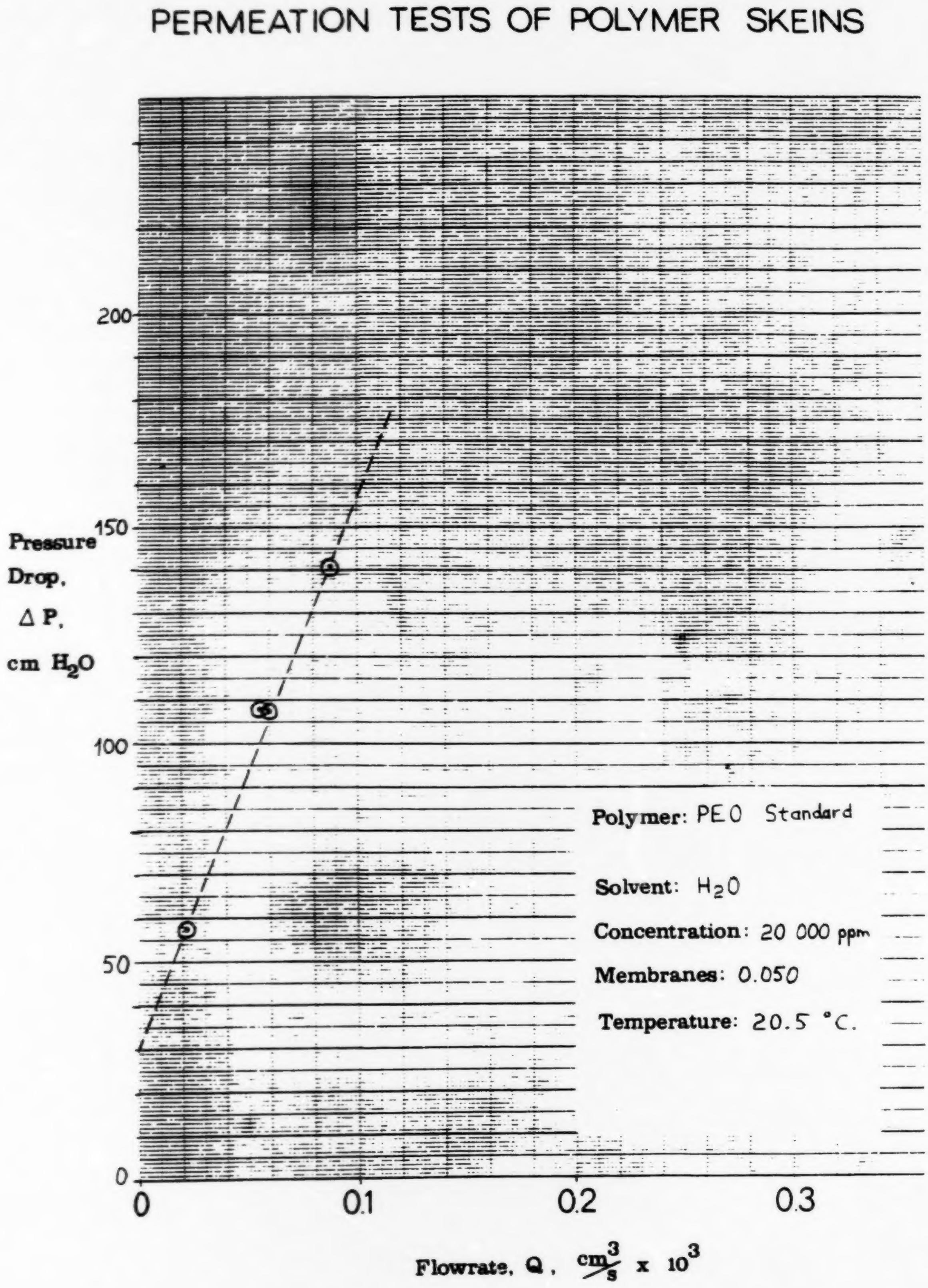
PERMEATION TESTS OF POLYMER SKEINS
Pressure Drop, ΔP, cm H2O
200
150
100
50
0
0
0.1
0.2
0.3
Flowrate, Q, cm3/s x 10^3
Polymer: PEO Standard
Solvent: H2O
Concentration: 20 000 ppm
Membranes: 0.050
Temperature: 20.5 °C.

Figure 9

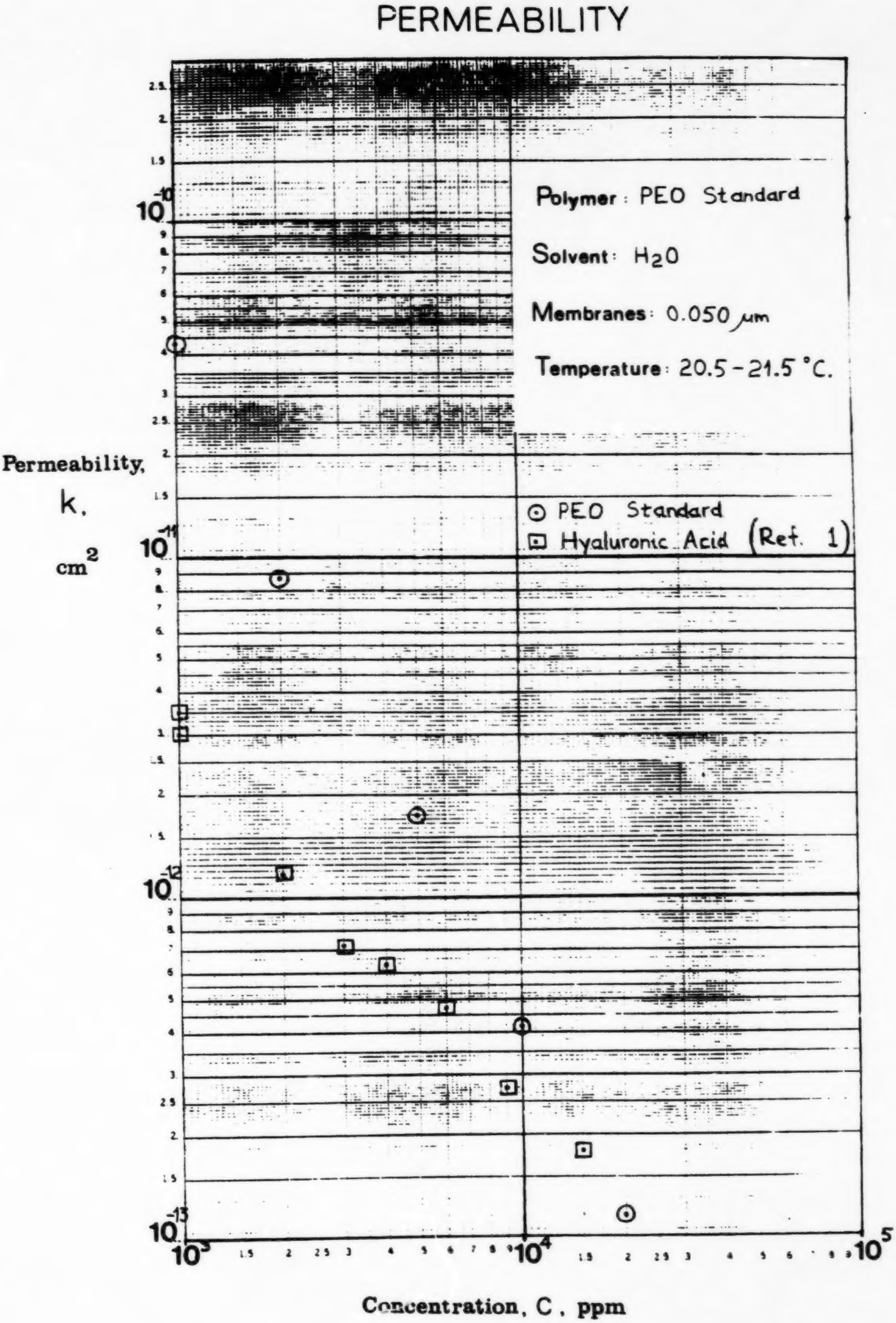
PERMEABILITY
Polymer: PEO Standard
Solvent: H_2O
Membranes: 0.050 μm
Temperature: 20.5 - 21.5 °C.
⊙ PEO Standard
⊡ Hyaluronic Acid (Ref. 1)
Permeability, k, cm^2
10^{-10}
10^{-11}
10^{-12}
10^{-13}
10^3
10^4
10^5
Concentration, C, ppm

Figure 10

PERMEATION TESTS OF POLYMER SKEINS

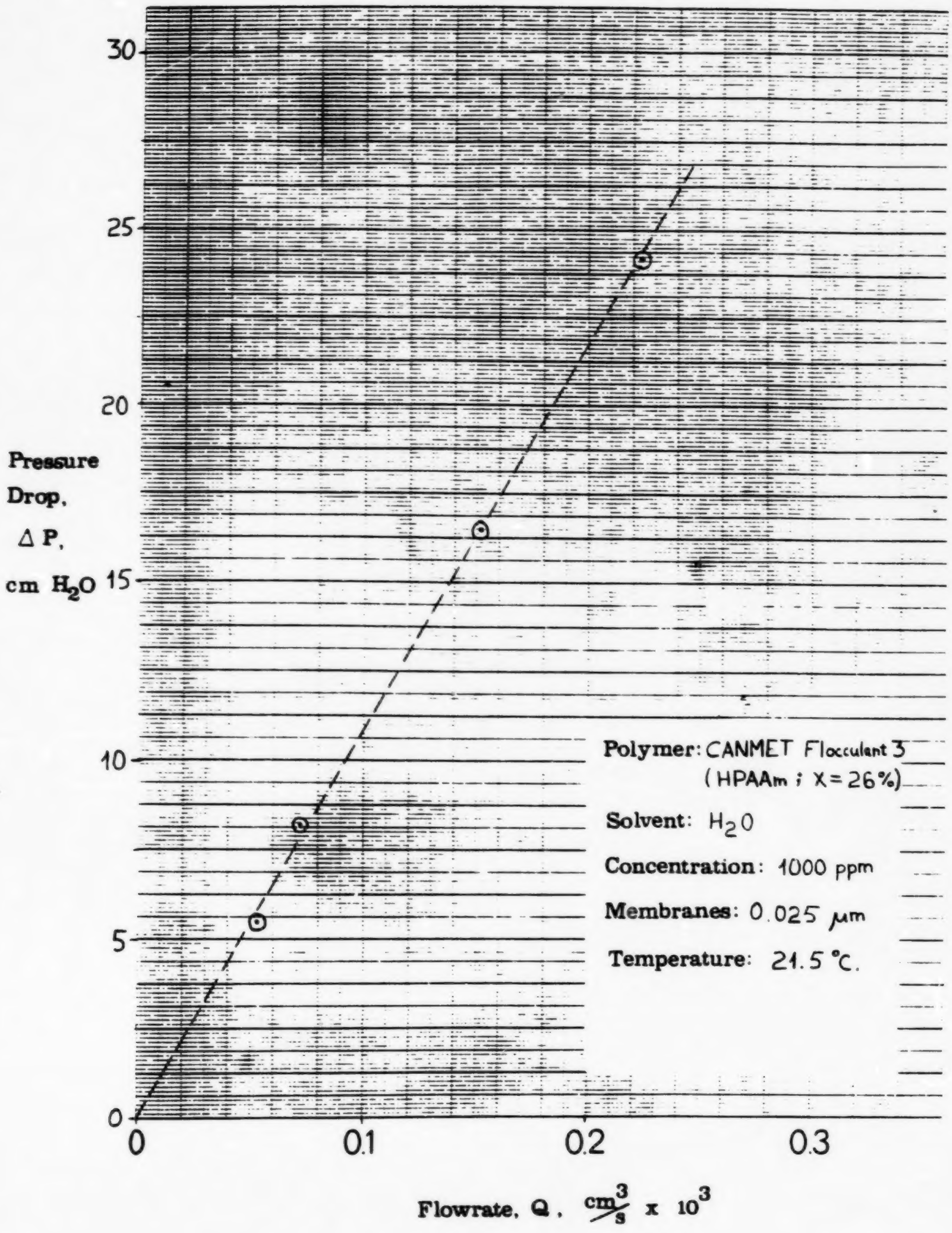

Figure 11

PERMEATION TESTS OF POLYMER SKEINS

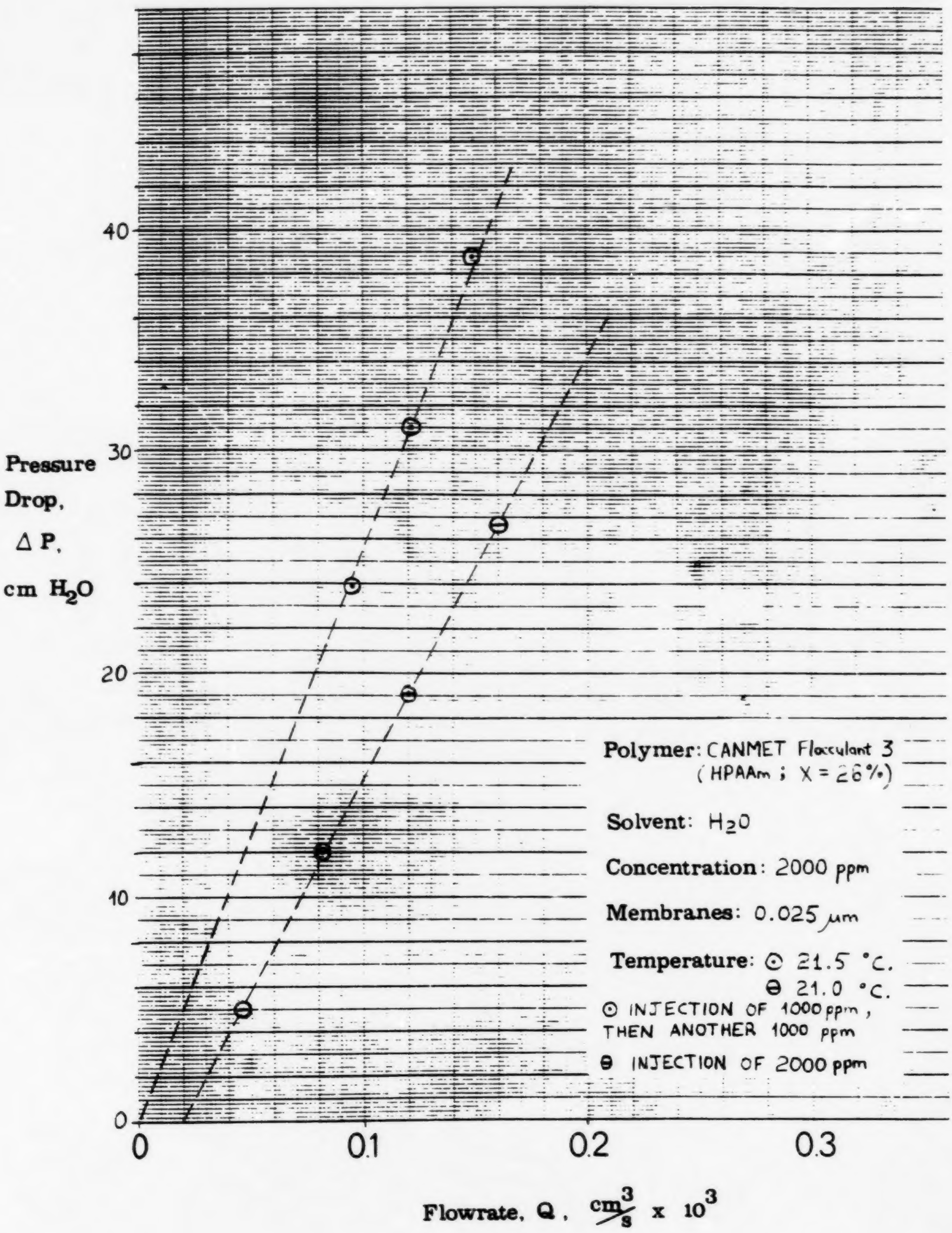

Figure 12

PERMEATION TESTS OF POLYMER SKEINS

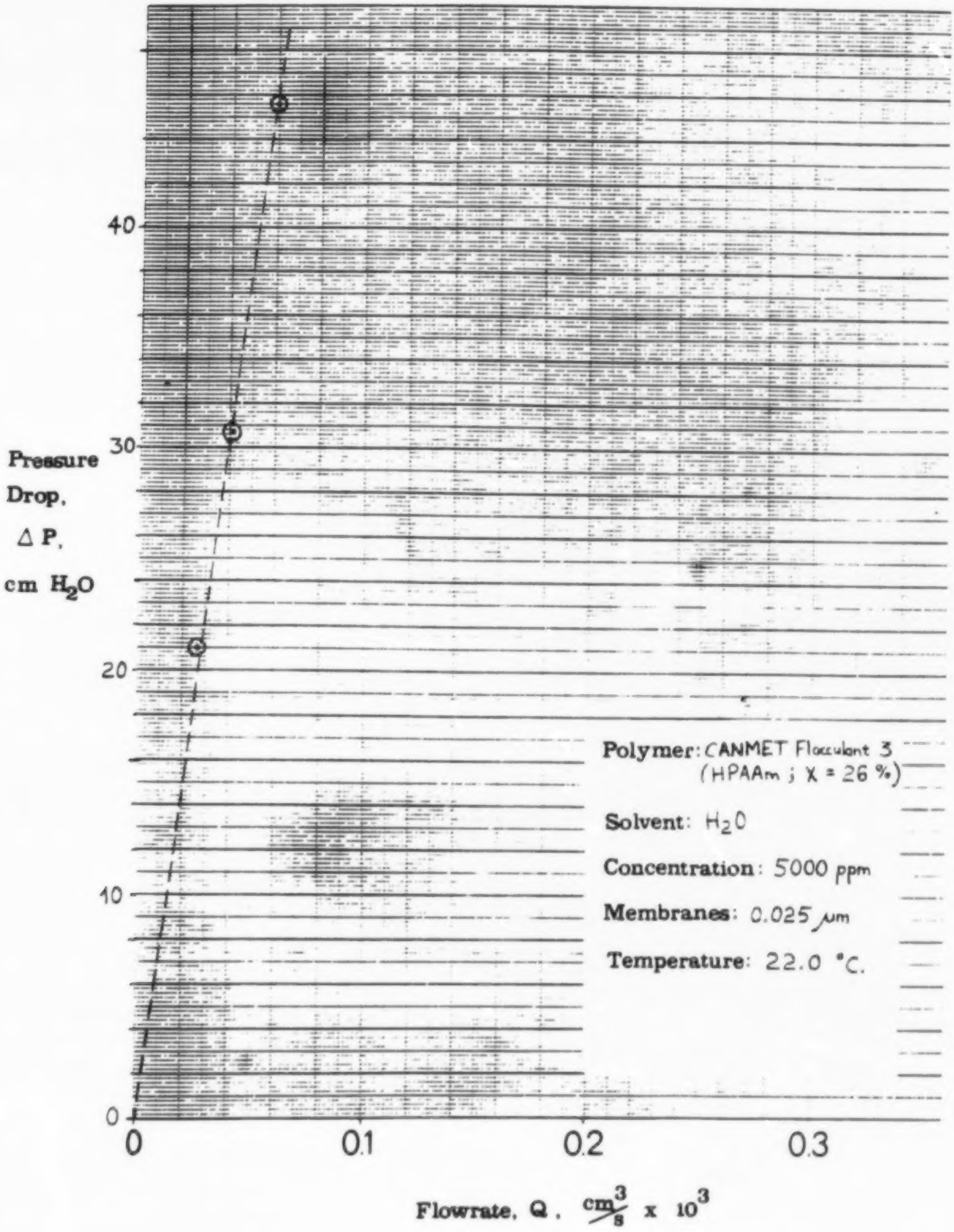

Figure 13

PERMEATION TESTS OF POLYMER SKEINS

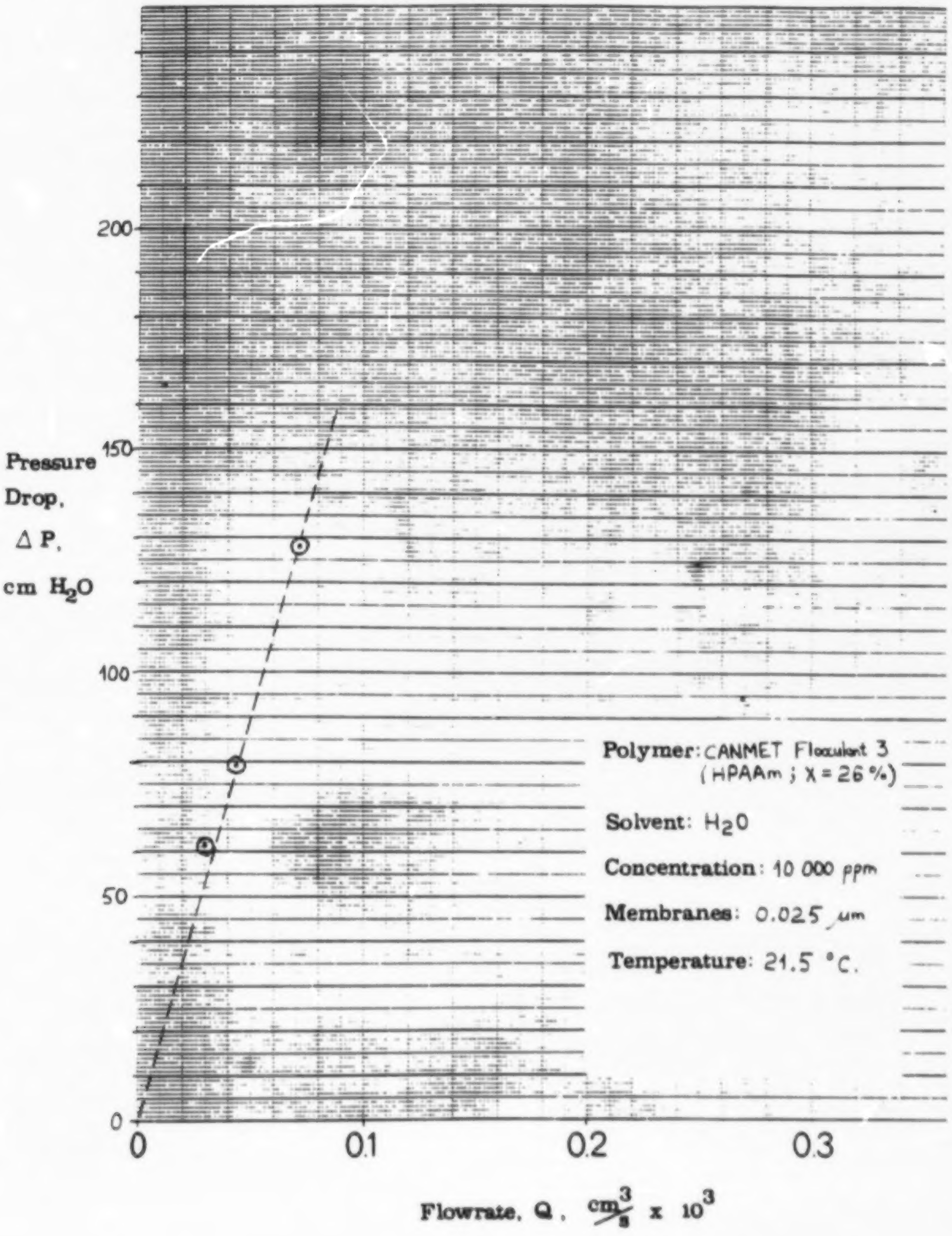

Figure 14

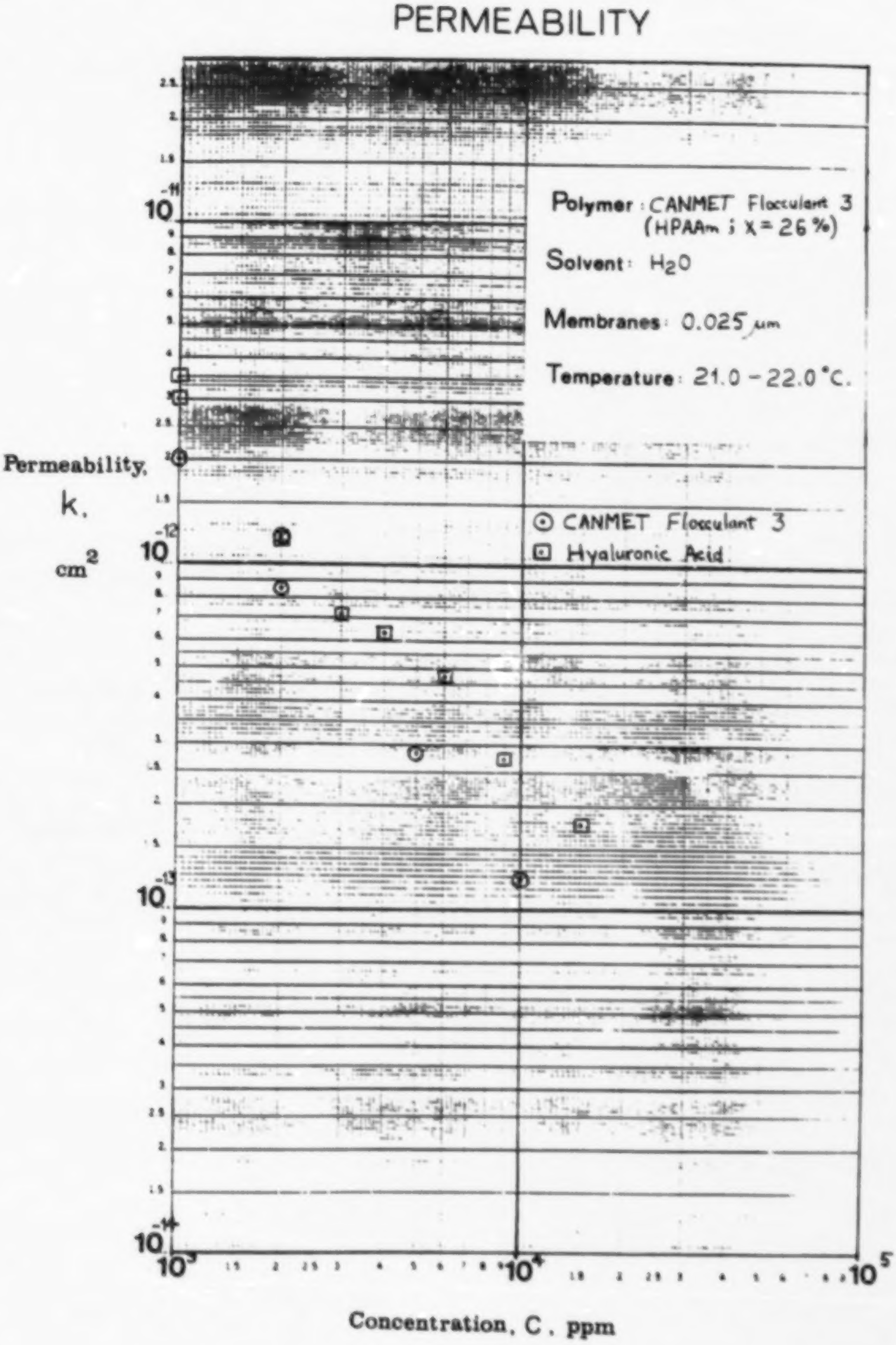
PERMEABILITY
Polymer: CANMET Flocculant 3 (HPAAm ; x = 26 %)
Solvent: H2O
Membranes: 0.025 μm
Temperature: 21.0 - 22.0 °C.
⊙ CANMET Flocculant 3
⊡ Hyaluronic Acid
Permeability, k, cm2
10-11
10-12
10-13
10-14
10³
10⁴
10⁵
Concentration, C, ppm

Figure 15

PERMEATION TESTS OF POLYMER SKEINS

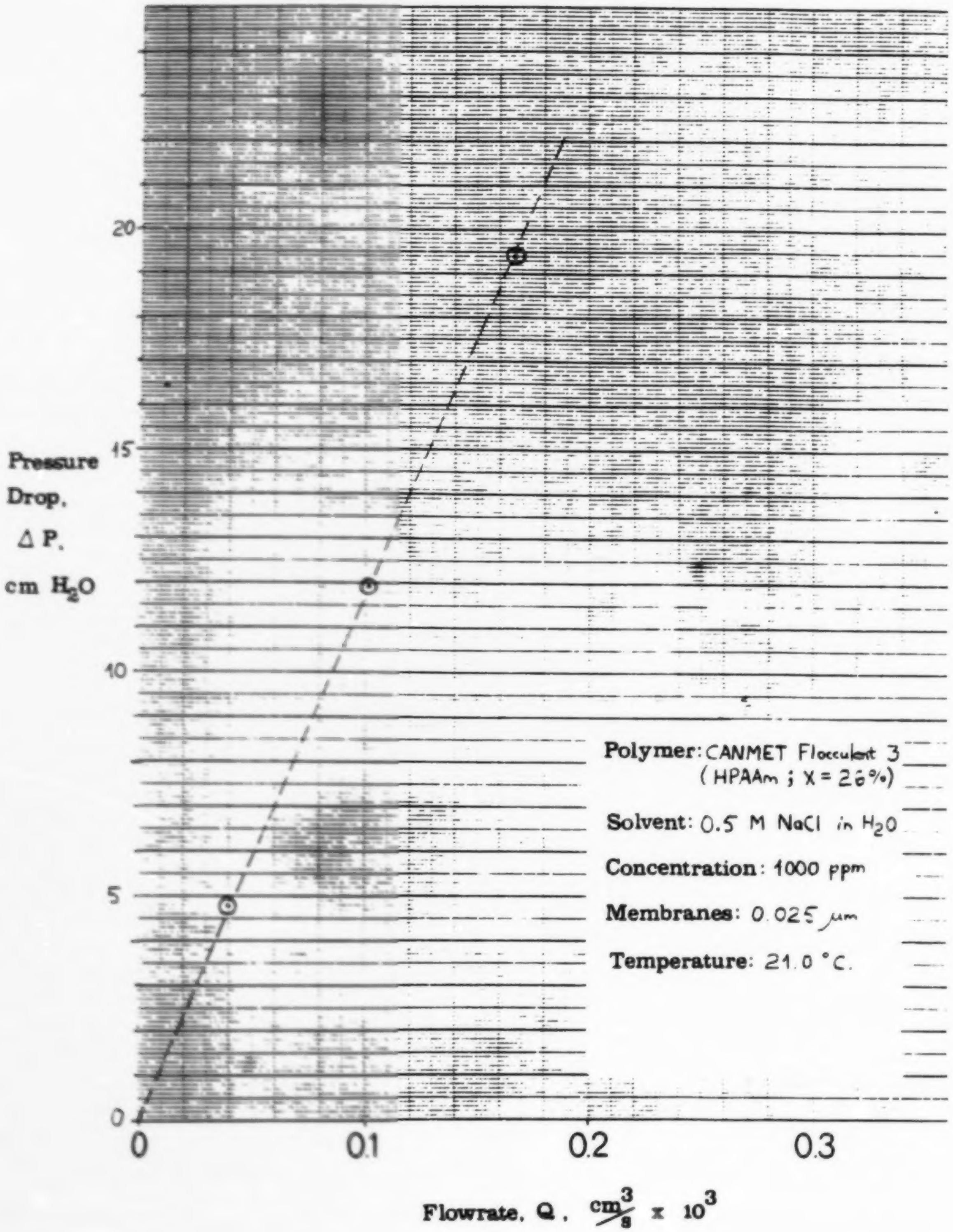

Figure 16

PERMEATION TESTS OF POLYMER SKEINS

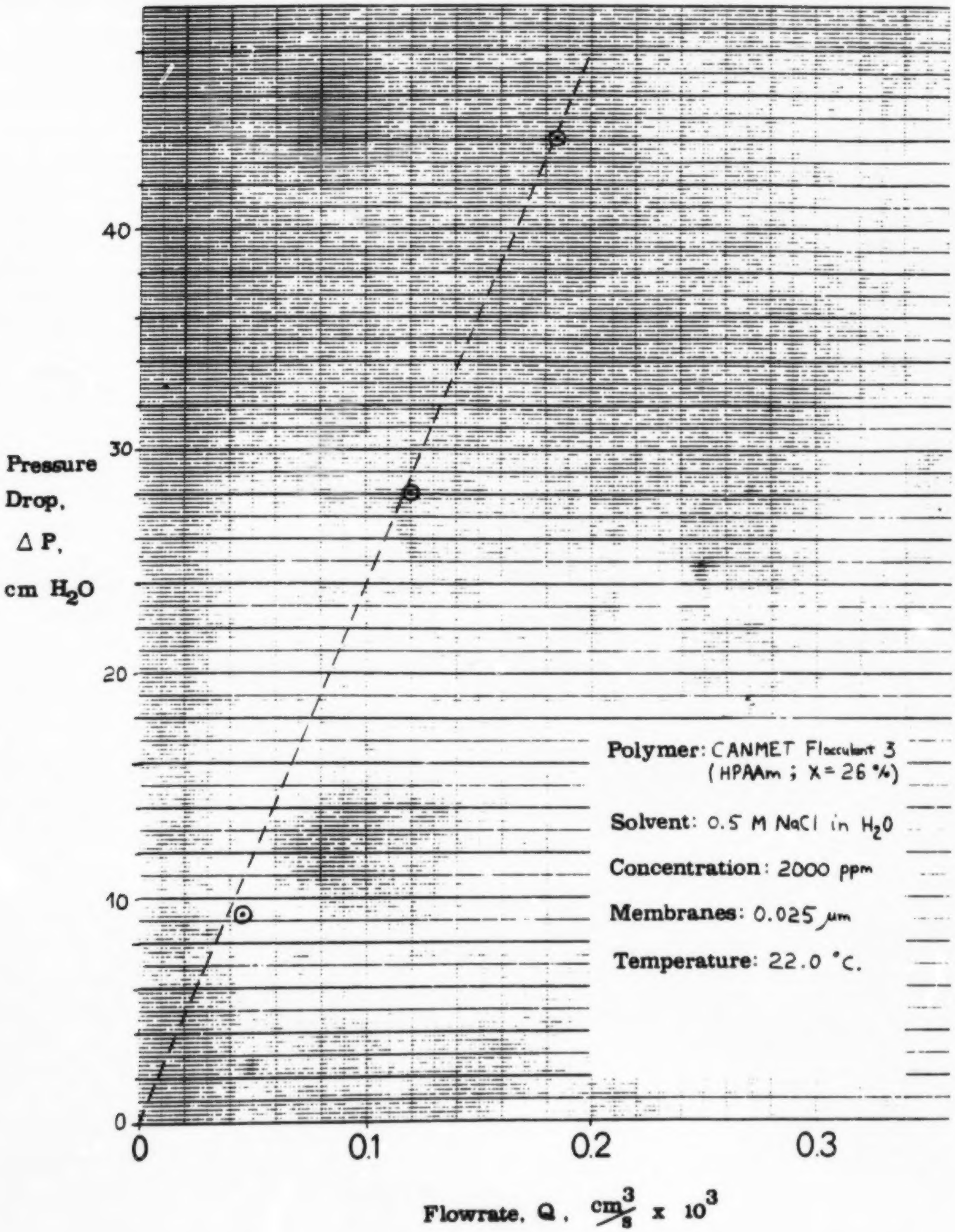

Figure 17

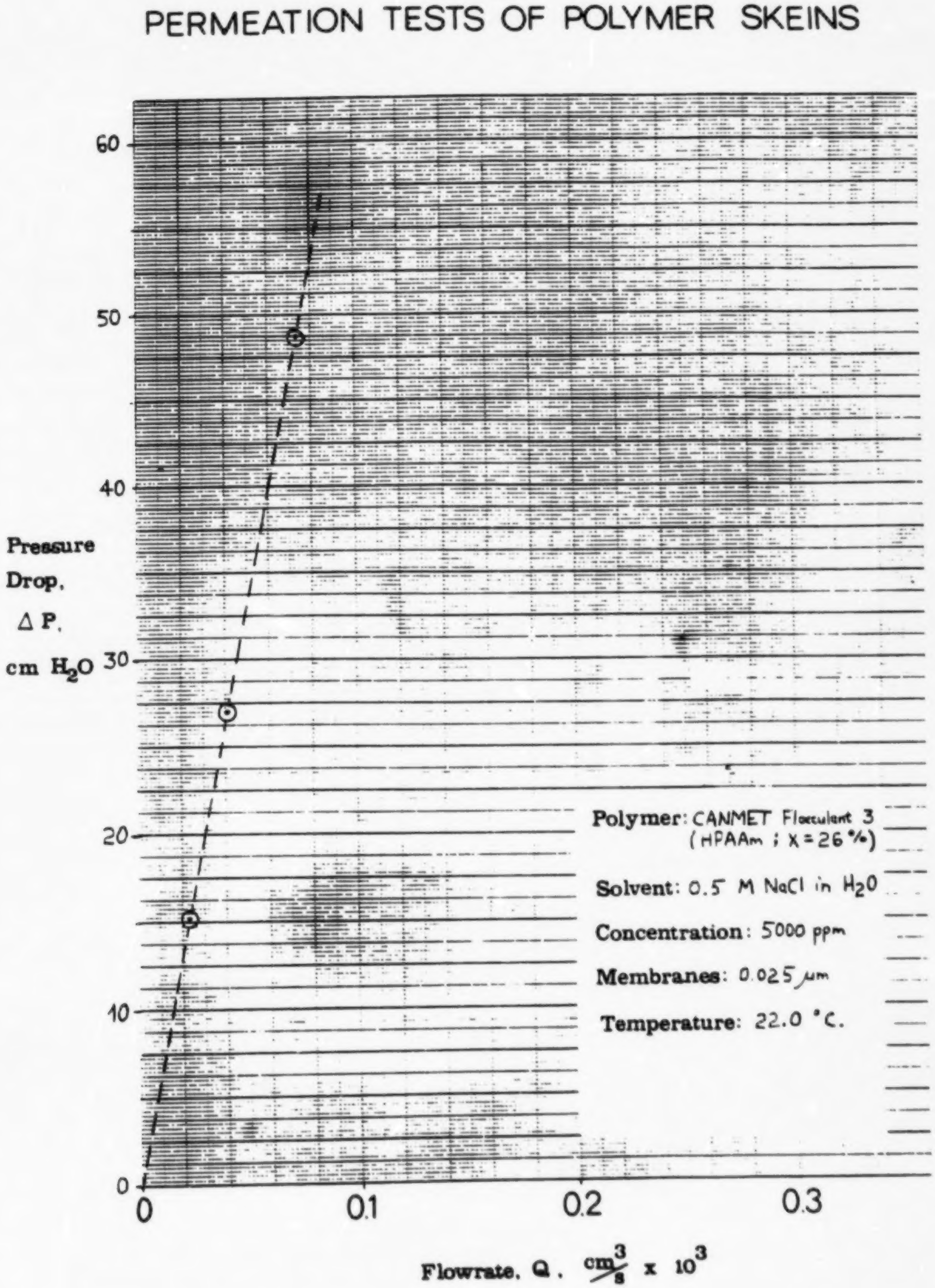
PERMEATION TESTS OF POLYMER SKEINS

Figure 18

PERMEABILITY

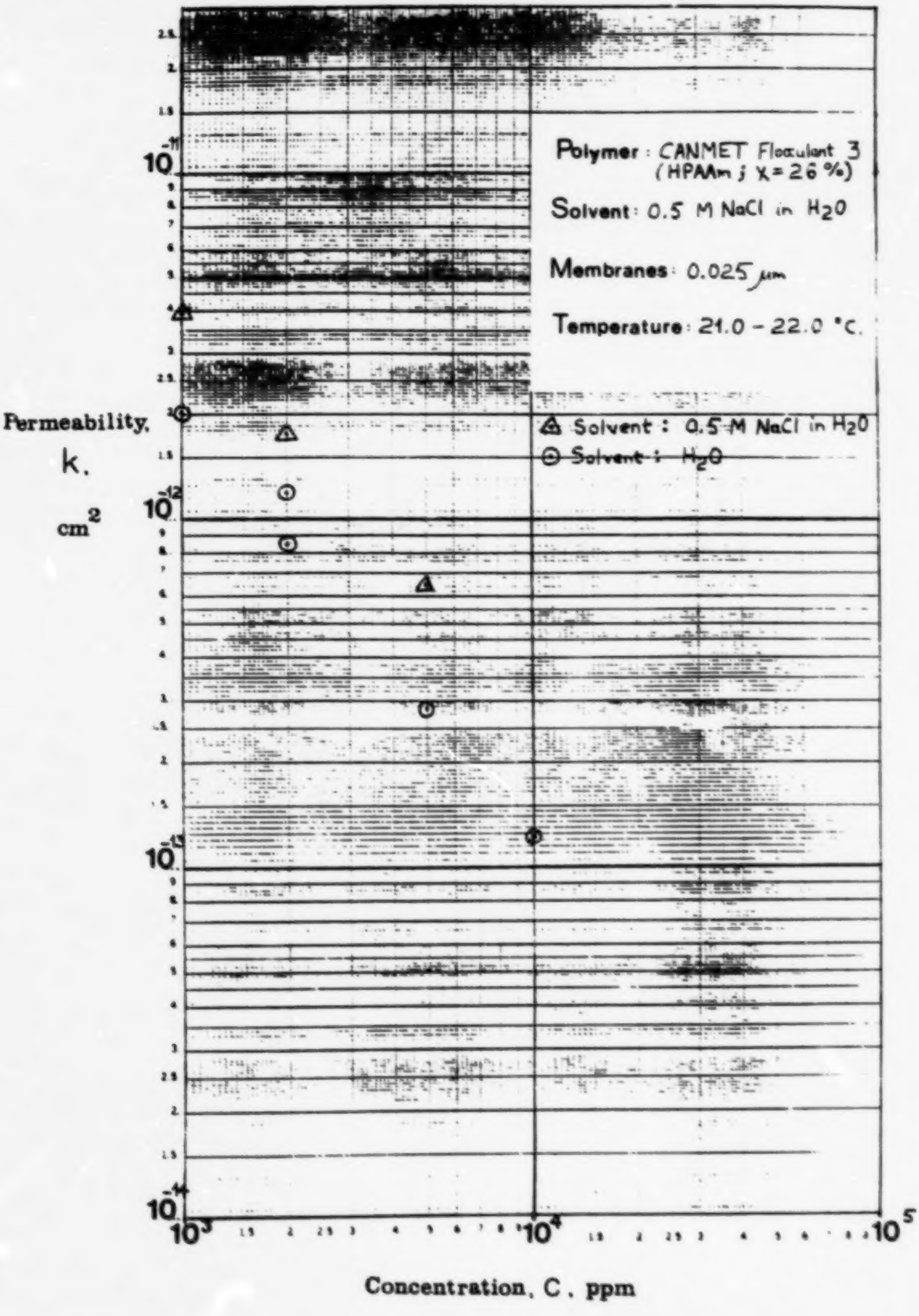

Figure 19

PERMEATION TESTS OF POLYMER SKEINS

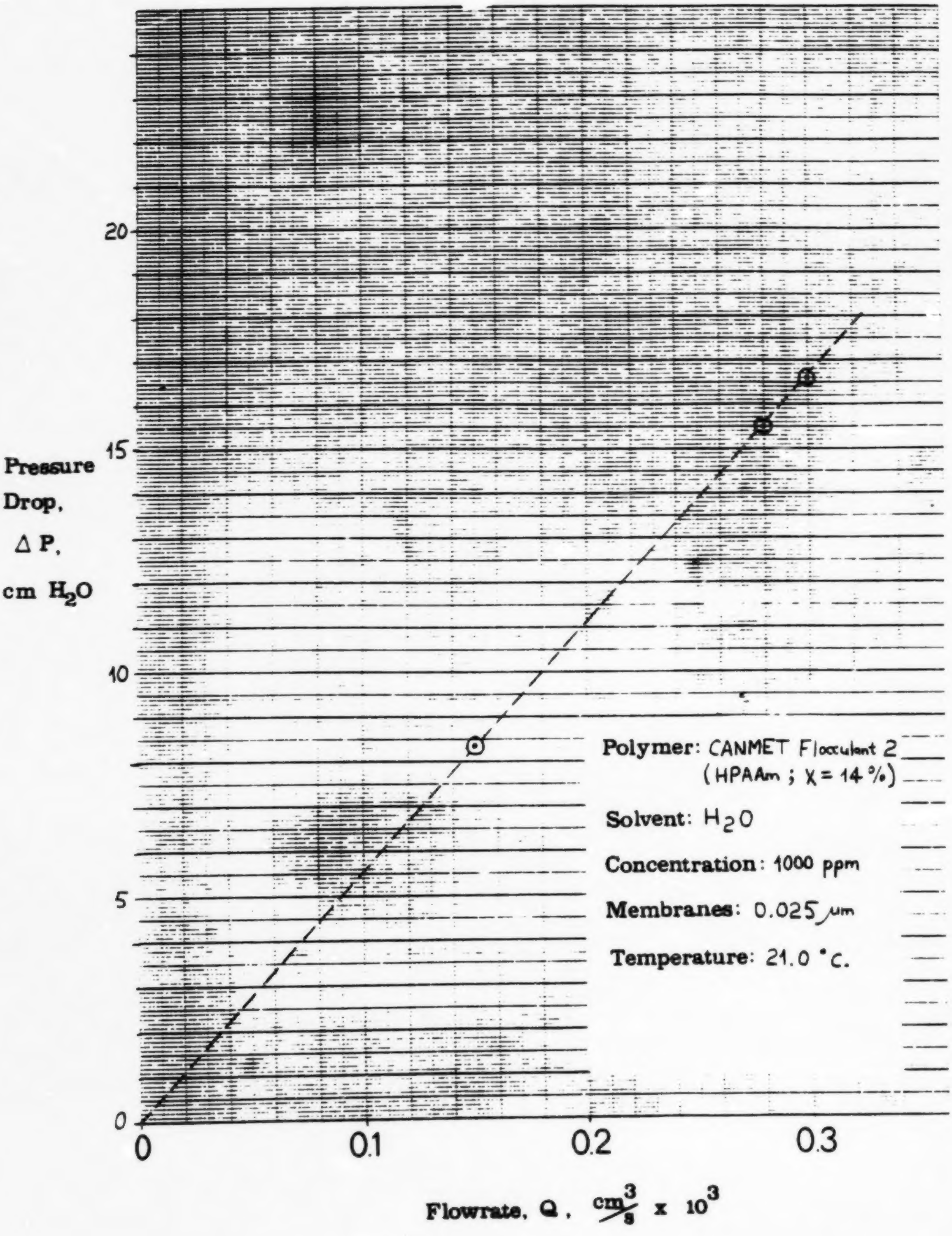

Figure 20

PERMEATION TESTS OF POLYMER SKEINS

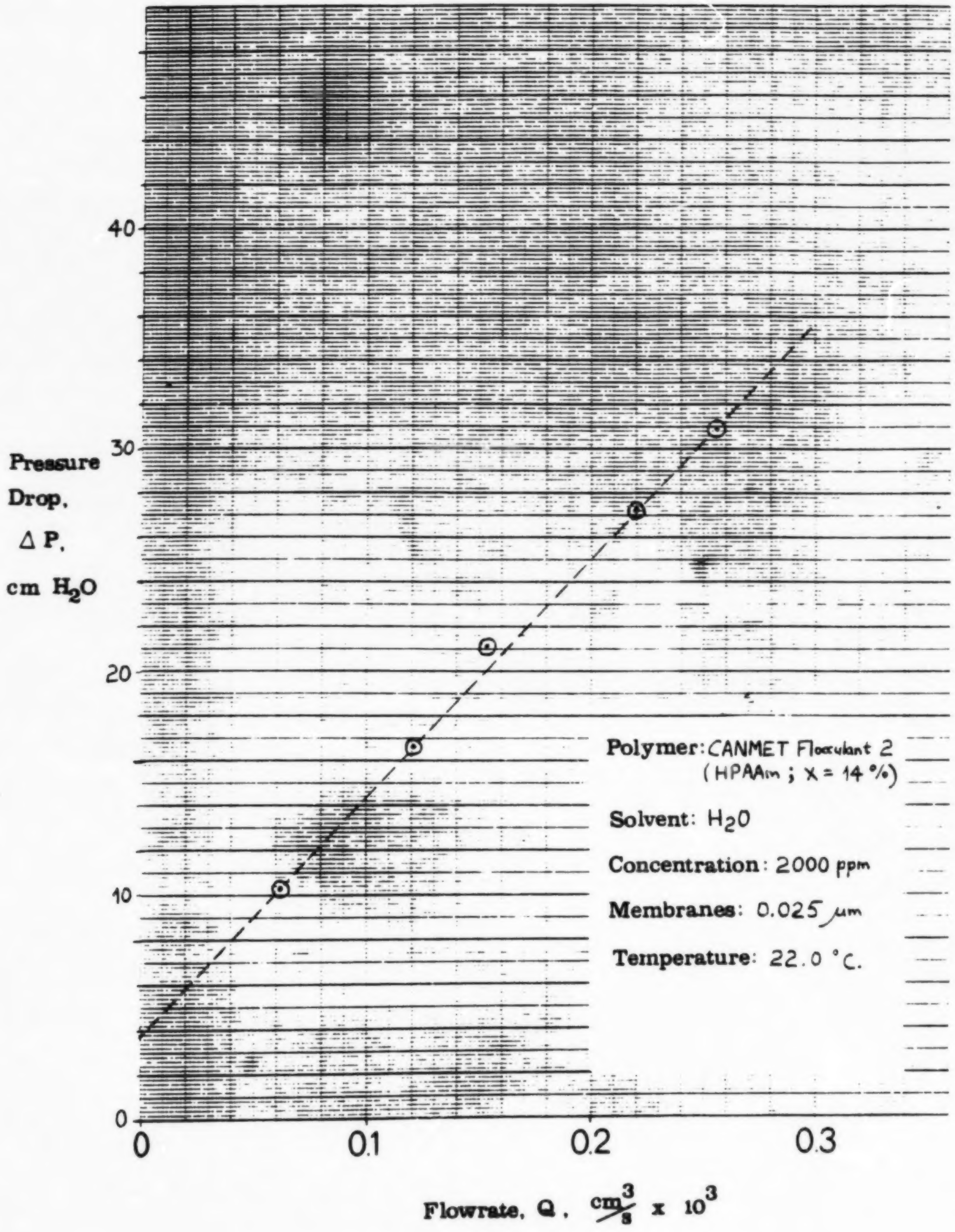

Figure 21

PERMEATION TESTS OF POLYMER SKEINS

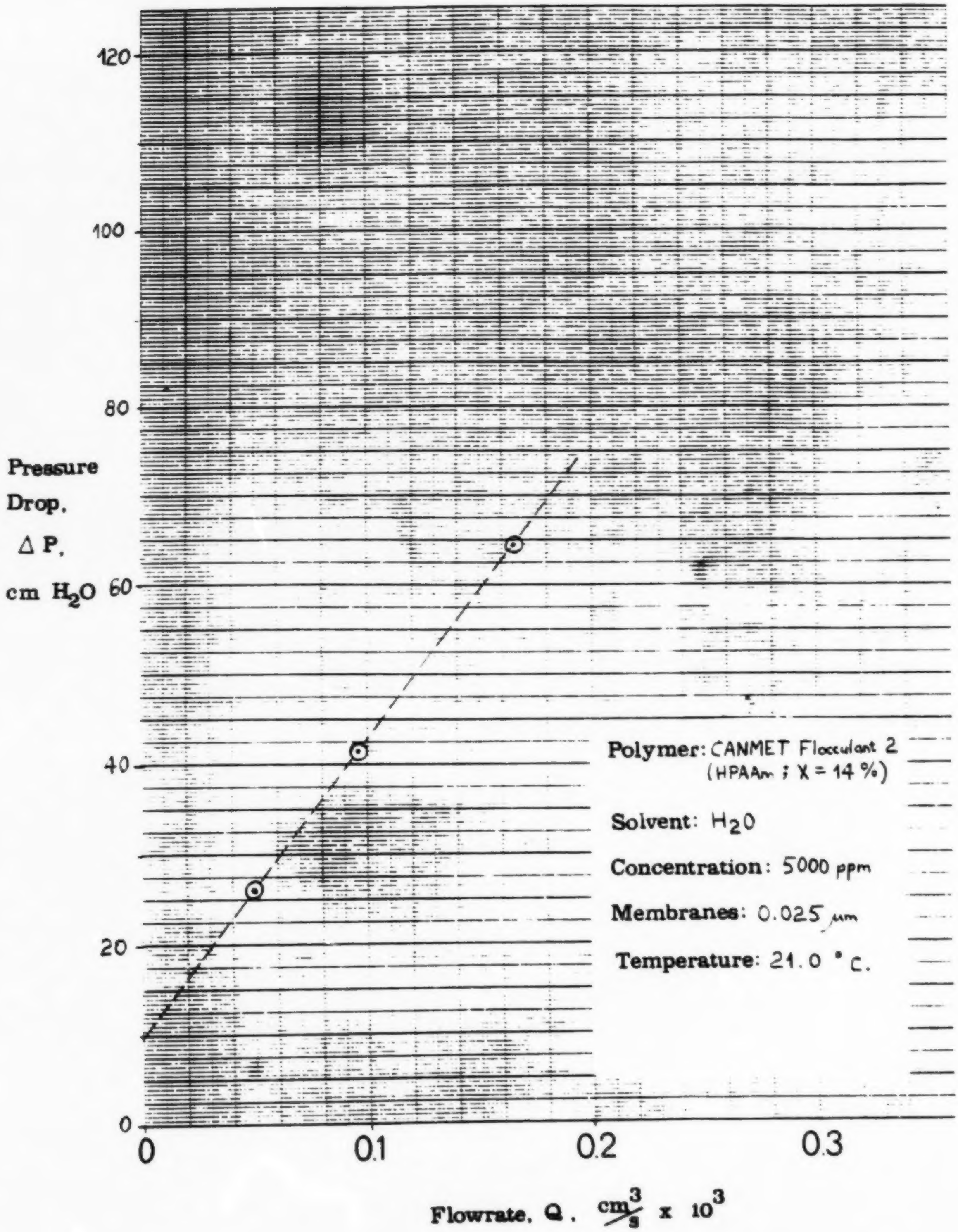

Figure 22

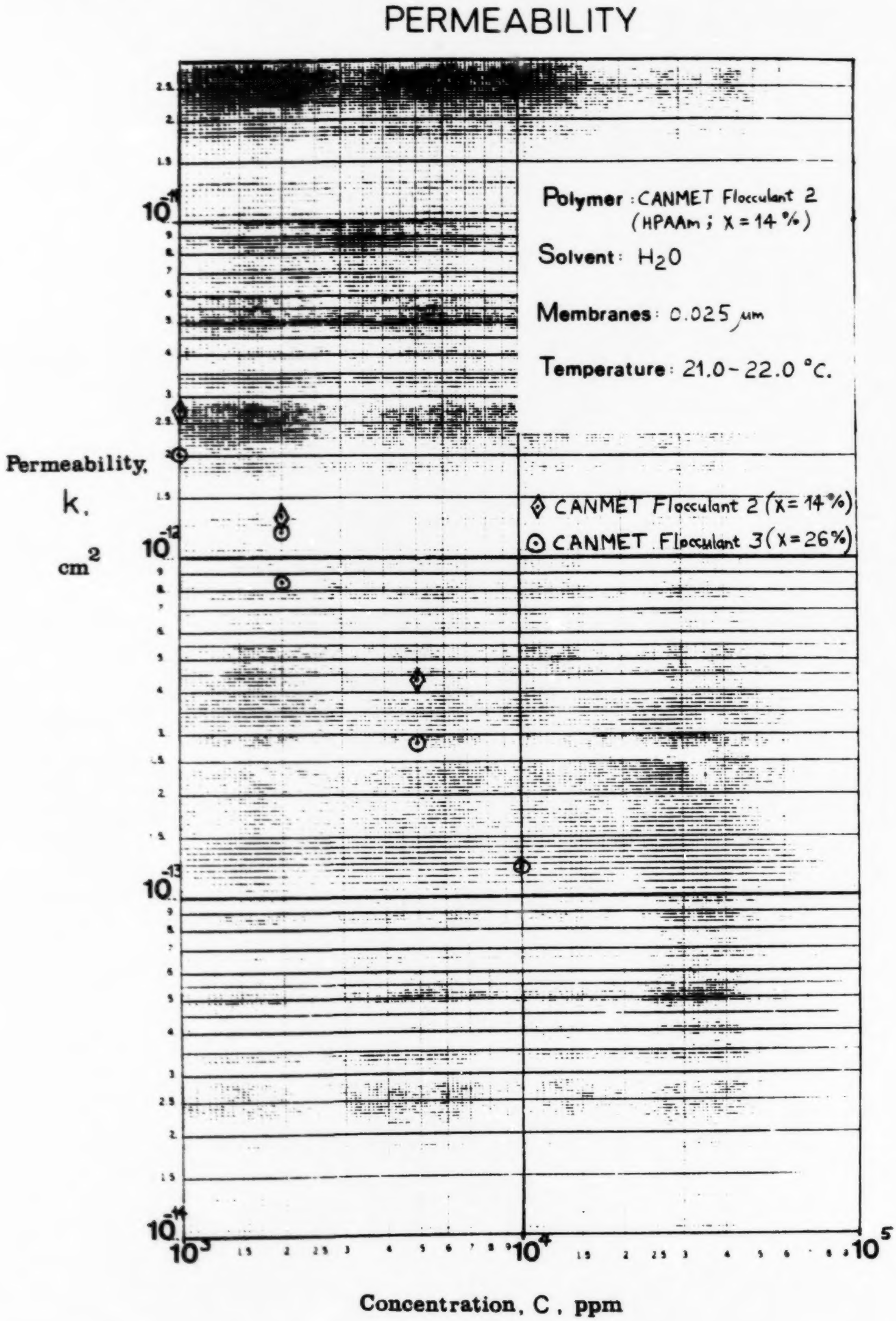

PERMEABILITY

Figure 23

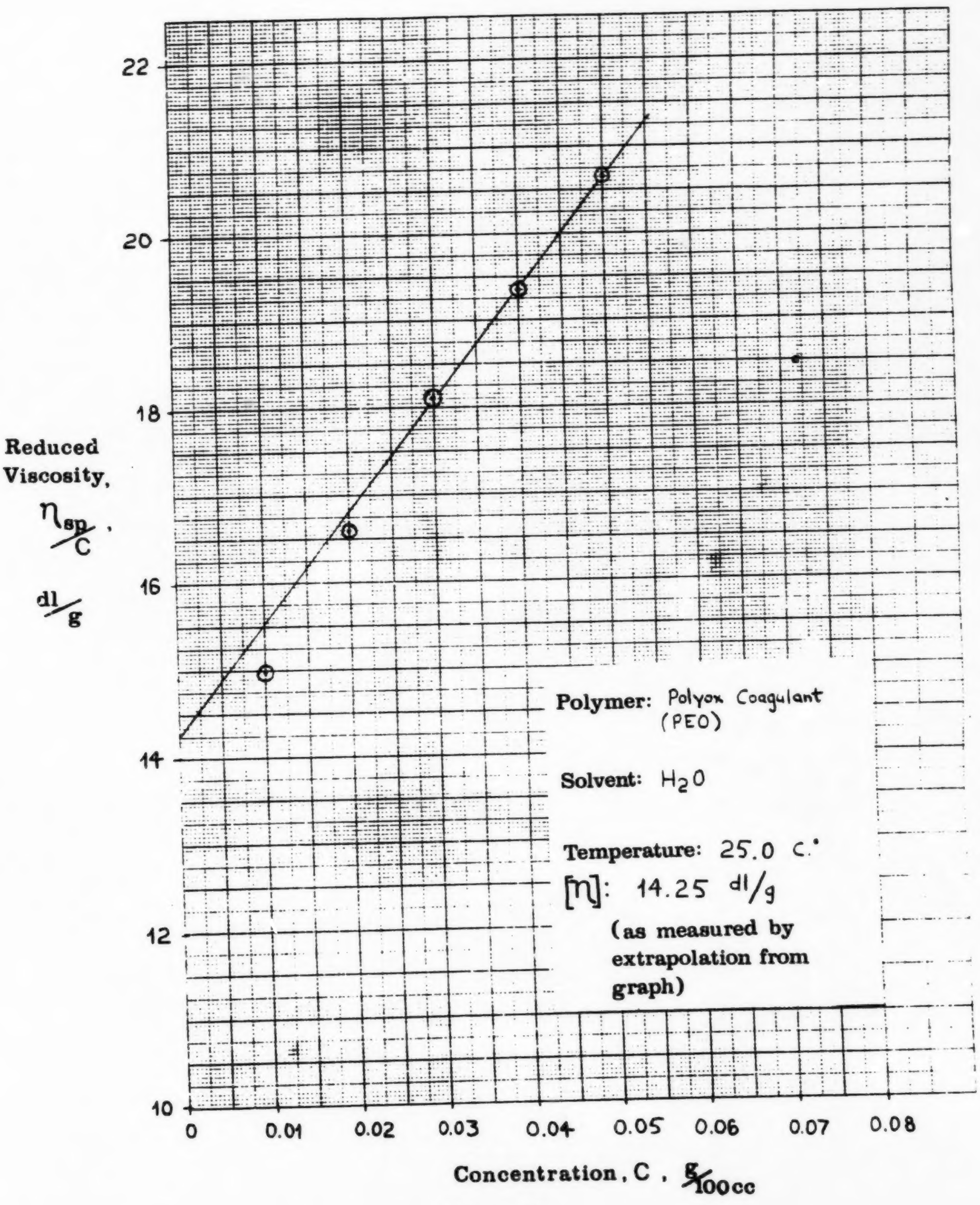

INTRINSIC VISCOSITY

Figure 24

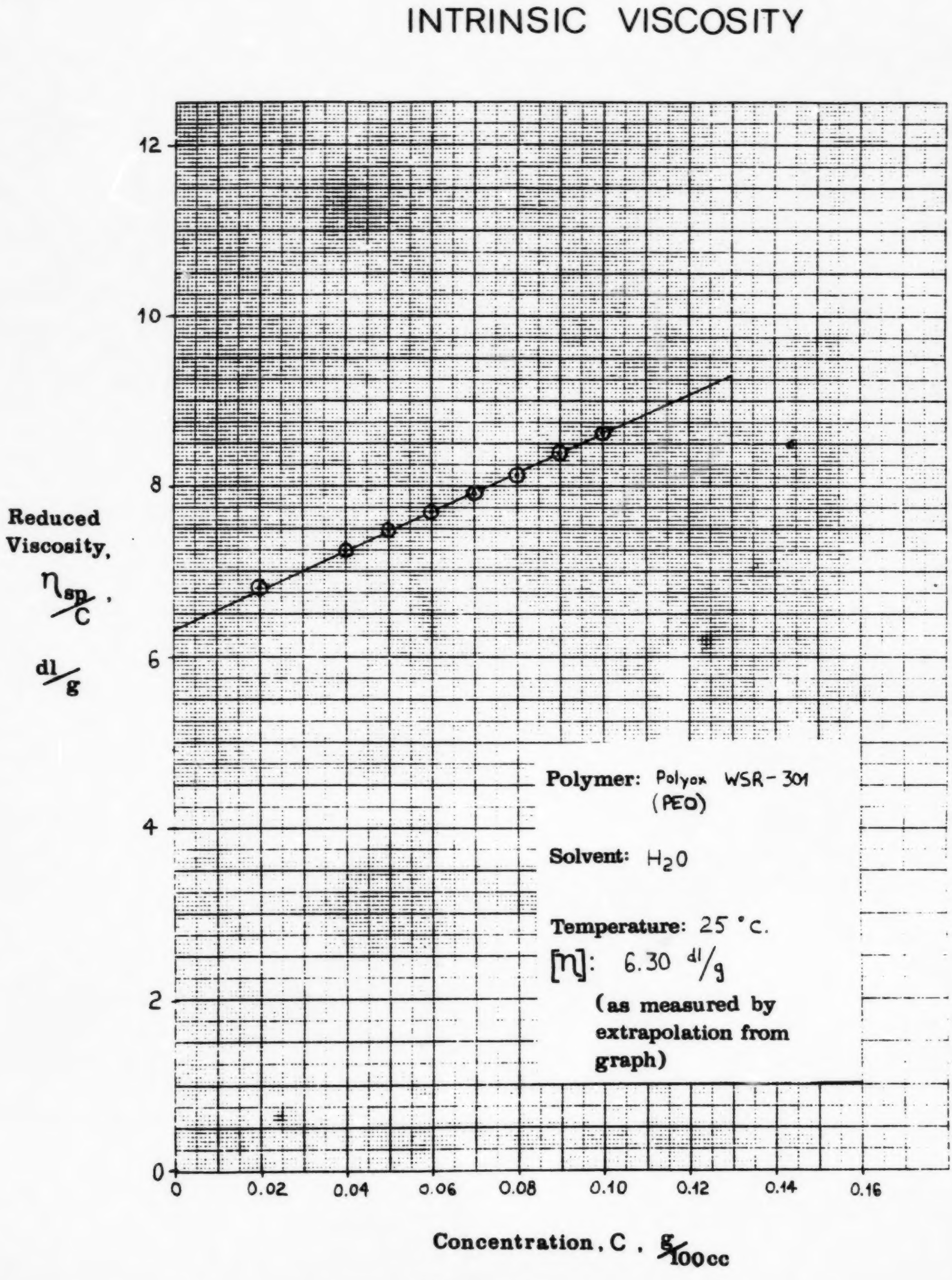
INTRINSIC VISCOSITY
Reduced Viscosity, η_{sp}/C, dl/g
0
2
4
6
8
10
12
0
0.02
0.04
0.06
0.08
0.10
0.12
0.14
0.16
Concentration, C, g/100cc
Polymer: Polyox WSR-301 (PEO)
Solvent: H_2O
Temperature: 25 °c.
[η]: 6.30 dl/g
(as measured by extrapolation from graph)

Figure 25

INTRINSIC VISCOSITY

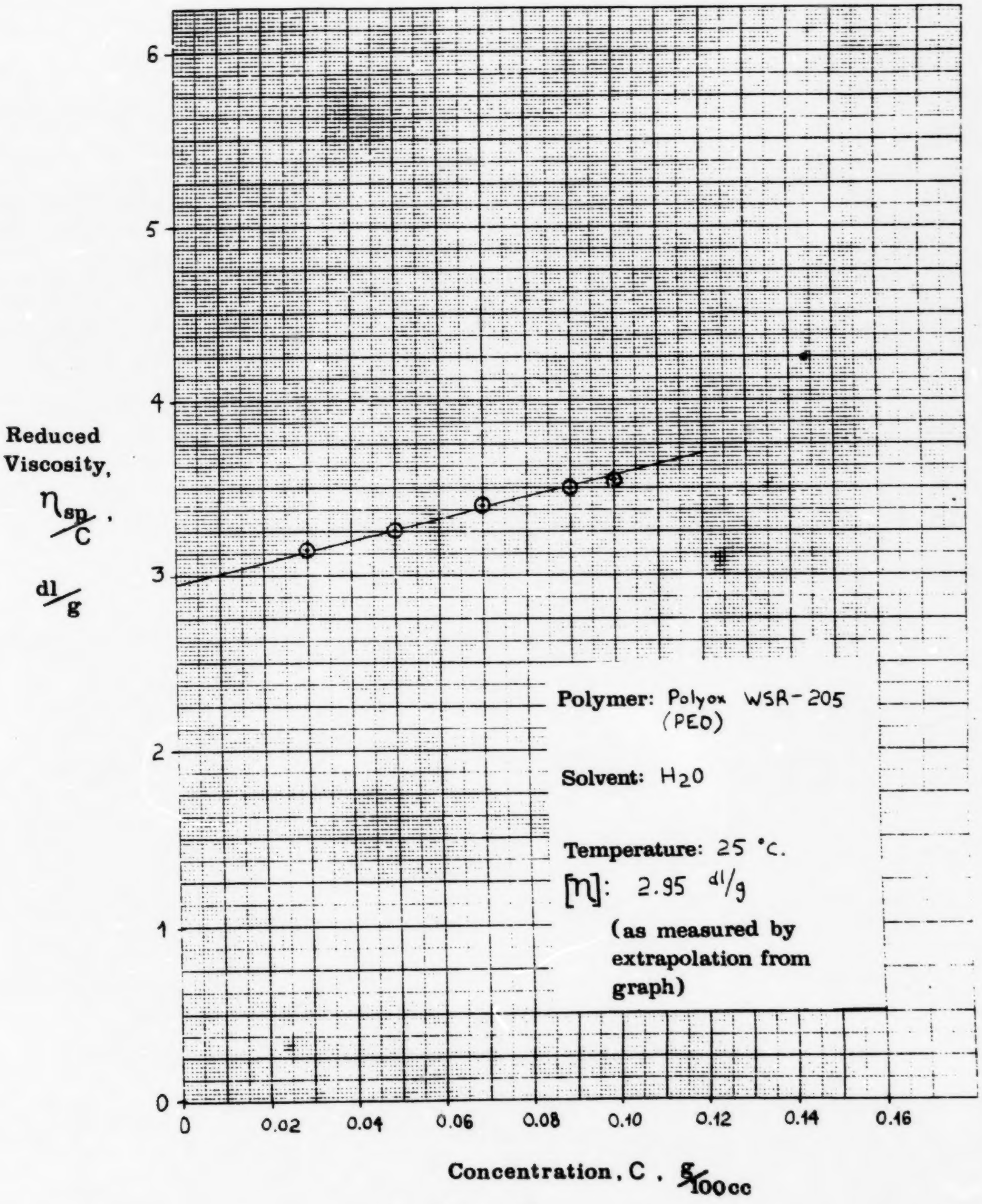

Figure 26

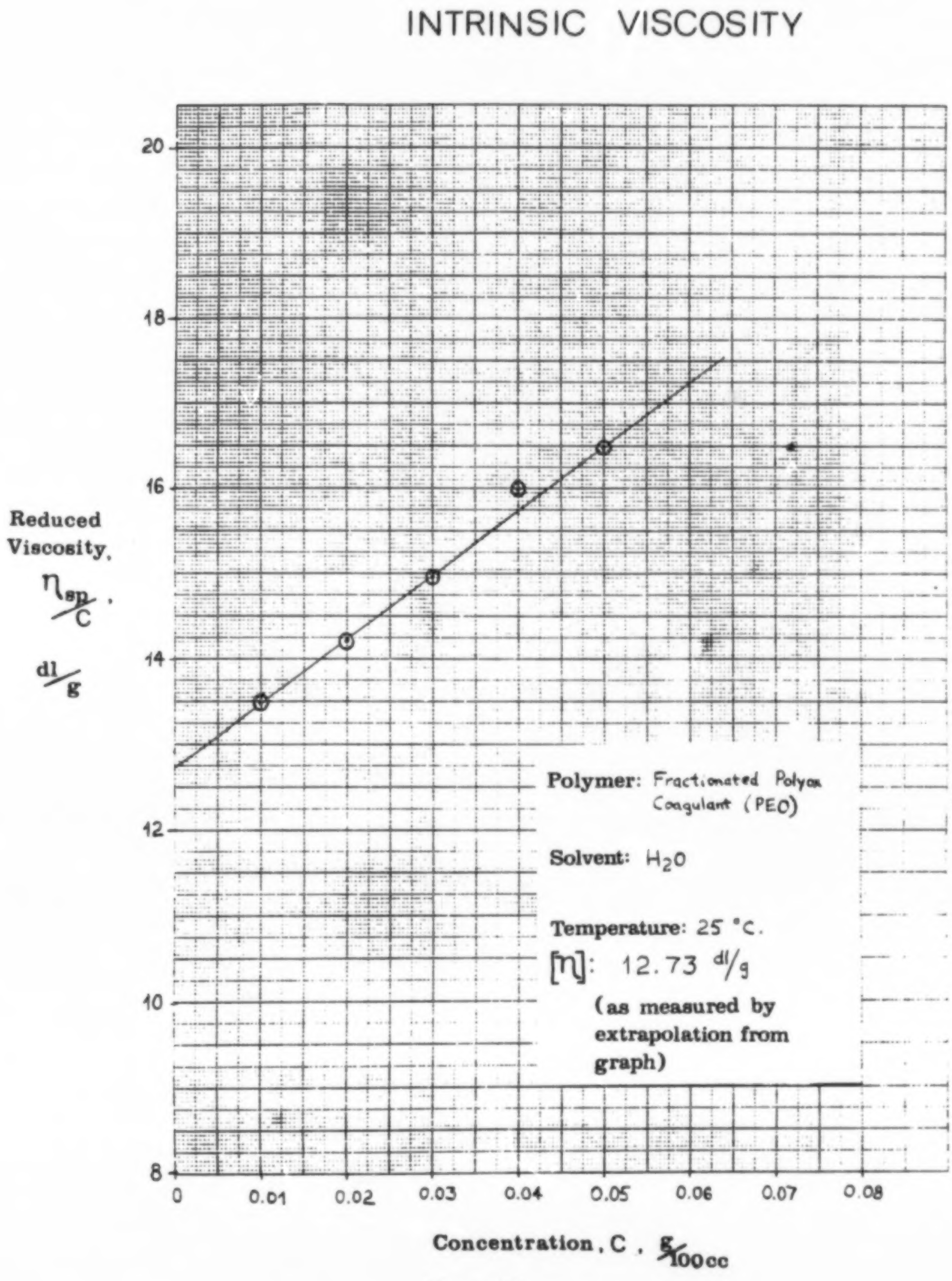
INTRINSIC VISCOSITY
20
18
16
14
12
10
8
0
0.01
0.02
0.03
0.04
0.05
0.06
0.07
0.08
Reduced Viscosity, η_{sp}/C, dl/g
Concentration, C, g/100cc
Polymer: Fractionated Polyox Coagulant (PEO)
Solvent: H_2O
Temperature: 25 °C.
[η]: 12.73 dl/g
(as measured by extrapolation from graph)

Figure 27

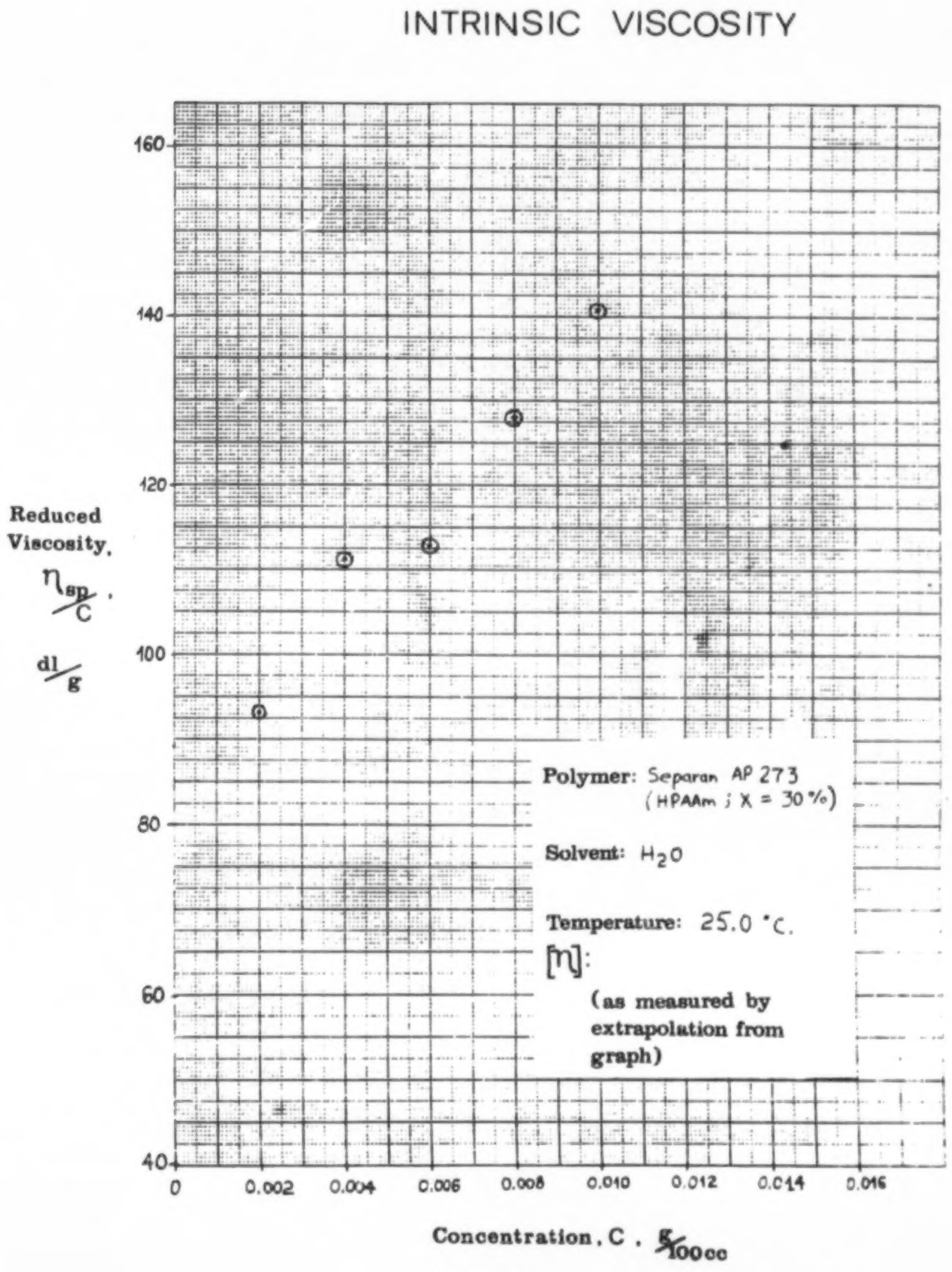
INTRINSIC VISCOSITY
Reduced Viscosity, η_{sp}/C, dl/g
160
140
120
100
80
60
40
0
0.002
0.004
0.006
0.008
0.010
0.012
0.014
0.016
Concentration, C, g/100cc
Polymer: Separan AP 273 (HPAAm ; X = 30 %)
Solvent: H_2O
Temperature: 25.0 °C.
[η]:
(as measured by extrapolation from graph)

Figure 28

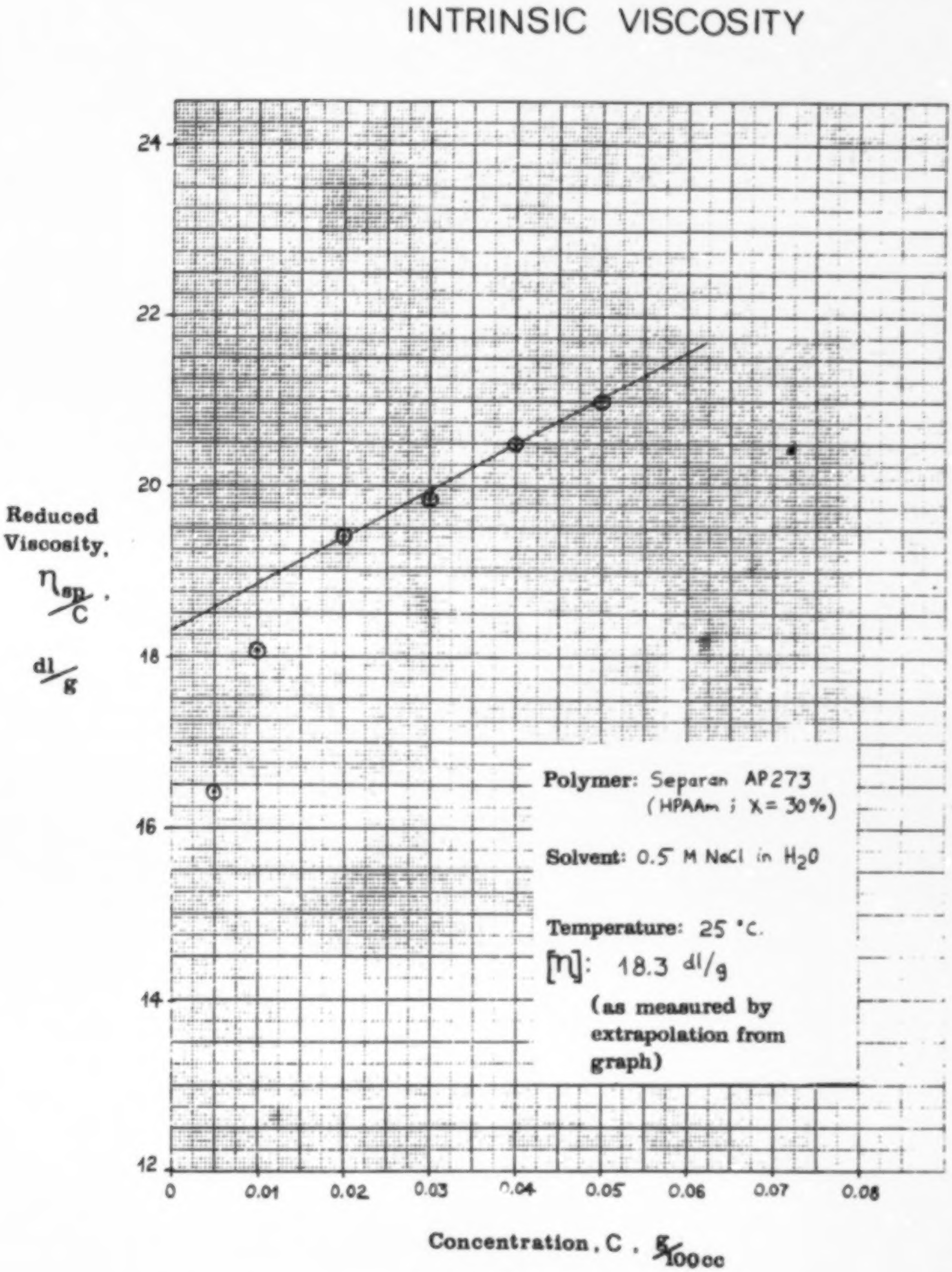
INTRINSIC VISCOSITY
24
22
20
18
16
14
12
Reduced Viscosity, η_{sp}/C, dl/g
0
0.01
0.02
0.03
0.04
0.05
0.06
0.07
0.08
Concentration, C, g/100cc
Polymer: Separan AP273 (HPAAm ; X = 30%)
Solvent: 0.5 M NaCl in H_2O
Temperature: 25 °C.
[η]: 18.3 dl/g
(as measured by extrapolation from graph)

Figure 29